Hybrid Bragg stacks - polymer-clay nanocomposites defined by ultraconfinement

Dissertation

zur Erlangung des akademischen Grades

Doktorin der Naturwissenschaften (Dr. rer. nat.)

in der Bayreuther Graduiertenschule für Mathematik und Naturwissenschaften

(BayNAT) der Universität Bayreuth

vorgelegt von

Theresa Sophie Dörres

geborene Schilling, in Coburg

Bayreuth, 2020

Die vorliegende Arbeit wurde in der Zeit von Dezember 2016 bis Dezember 2020 in Bayreuth am Lehrstuhl für Anorganische Chemie I unter Betreuung von Herrn Prof. Dr. Josef Breu angefertigt.

Vollständiger Abdruck der von der Bayreuther Graduiertenschule für Mathematik und Naturwissenschaften (BayNAT) der Universität Bayreuth genehmigten Dissertation zur Erlangung des akademischen Grades einer Doktorin der Naturwissenschaften (Dr. rer. nat.).

Dissertation eingereicht am: 18. Dezember 2020
Zulassung durch das Leitungsgremium: 14. Januar 2021
Wissenschaftliches Kolloquium: 17. Mai 2021

Amtierender Direktor: Prof. Dr. Markus Lippitz

Prüfungsausschuss:

Prof. Dr. Josef Breu	(Gutachter)
Prof. Dr. Markus Retsch	(Gutachter)
Prof. Dr. Birgit Weber	(Vorsitz)
Prof. Dr. Seema Agarwal	

Meiner Familie in Dankbarkeit gewidmet

„Satchidananda Swarupoham“

„Meine wahre Natur ist Sein, Wissen und Glückseligkeit“

„Das habe ich noch nie vorher versucht.

Also bin ich völlig sicher, dass ich es schaffe.“

Pippi Langstrumpf

Tables of contents

List of abbreviations

1D	One-dimensional
2D	Two-dimensional
3D	Three-dimensional
BLS	Brillouin light spectroscopy
CV	Coefficient of variation
DS	Double stacks
FWHM	Full width at half maximum
MMT	Montmorillonite
Hec	Synthetic sodium fluorohectorite
OP	Oxygen permeability
OS	Octahedral sheet
PEG	Polyethylene glycol
PVA	Poly(vinyl alcohol)
PVP	Polyvinylpyrrolidone
RH	Relative humidity
SAXS	Small angle X-ray scattering
SEM	Scanning electron microscopy
TEM	Transmission electron microscopy
Tg	Glass-transition temperature
TS	Tetrahedral sheet
UPy	Ureidopyrimidinone
PXRD	(Powder) x-ray diffraction

1 Summary

Natural composites like wood, bones or nacre always served as inspiration for the design of advanced and functional materials. All natural composites have one thing in common; the constituents are hierarchically arranged over multiple length scales. In case of nacre, the hierarchical arrangement of the strong and weak but tough constituents in a so-called “brick-and-mortar” structure is considered as a precondition for the combination of the technically mutually exclusive properties of strength and toughness.

However, the realization of such highly ordered arrangements is not so easy to achieve for synthetic polymer-clay nanocomposites. Apart from the varying quality of clay and inadequate processing methods, phase segregation is a widespread problem. Phase segregation not only creates a problem with reproducibility but also renders a systematic variation of parameters and their influence on the material’s properties challenging.

This work is based on the unique ability to produce highly homogeneously ordered one-dimensional (1D) crystalline nanocomposite films by spray coating, which serve as model systems for investigating the thermoelastic, permeability and mechanical properties. In literature, such 1D crystals are referred to as hybrid Bragg stacks. Within this work, two polymer/clay systems are presented, that enable the realization of a 1D crystalline arrangement of clay nanoplatelets for two different polymer contents: polyvinylpyrrolidone (PVP) and polyethylene glycol (PEG).

One factor, enabling the synthesis is the used synthetic sodium fluorohectorite (Hec) and its unique and rare phenomenon of repulsive osmotic swelling. The resulting nanoplatelets of uniform thickness form nematic liquid crystalline phases that yield a perfectly homogeneous nematic hybrid phase when mixed with a polymer. By spray coating transparent, self-standing and monocrystalline films were obtained.

Carefully adjusting the Hec to PVP content, the basal spacing can be tuned in the range from 1.9 to 3.8 nm. The unique long-range 1D ordered hybrid films in combination with advanced characterization methods allow to determine the direction-dependent thermoelastic properties. The anisotropy between the in-plane and cross-plane thermal conductivities was found to be exceptionally high for an electrically insulation hybrid material. Moreover, the structural anisotropy of the hybrid films is also displayed in the anisotropy of the direction-dependent Young’s moduli. Although the films experience strong polymer confinement, density, specific heat, in-plane thermal conductivity, and all mechanical moduli display an effective medium behavior.

The cross-plane thermal conductivities however, do not obey a simple mixing rule, as the thermal transport in the cross-plane direction is highly governed by the clay/polymer interface.

The hybrid Bragg stacks with a PVP content of 40 and 31 vol% only differ in the filler loading and are comparable with respect to filler type, aspect ratio, quality of texture and one-dimensional (1D) crystallinity. The basal spacing of 2.3 and 3.0 nm corresponds to a monolayer and bilayer of PVP, respectively. Consequently, PVP features strong confinement, as the interlayer height falls beneath the polymer’s radius of gyration. Therefore, the hybrid Bragg stacks represent a perfect model system for studying the impact of the polymer confinement on permeability. Cussler’s theory predicts that the permeability only non-linearly depends on aspect ratio and volume fraction of clay. However, within this investigation an additional nonlinear effect of confinement on permeability is established.

Finally, the combination of mono and double layers of Hec and PEG is applied to fabricate hybrid Bragg stacks that differ in the thickness of Hec layers, polymer layer thickness and nanoplatelet diameter. The filler contents can be adjusted in the range from 73 to 91 wt%, of which the latter represent the record filler content in a clay nacre-mimetics. These highly filled hybrid Bragg stacks allow to study the bulk mechanics in a systematic way. However, only the hybrid Bragg stacks consisting of a monolayer of Hec and two layers of PEG behaves ductile with an elongation of 8% and a yield strength of 48 MPa. Summarizing, the ductility of the hybrid Bragg stack is lost when the thickness of the PEG decoupling layer is reduced, double layers of Hec are utilized, and the nanoplatelet diameter is increased.

2 Zusammenfassung

Natürliche Verbundwerkstoffe wie Holz, Knochen oder Perlmutt dienten schon immer als Inspiration für das Design fortschrittlicher und funktionaler Materialien. Alle natürlichen Verbundwerkstoffe haben eines gemeinsam: Die Bestandteile sind hierarchisch über mehrere Längenskalen strukturiert. Im Falle von Perlmutt gilt die hierarchische Anordnung des starken und des schwachen, aber zähen Bestandteils in einer so genannten "Backsteinmauer"-Struktur als Voraussetzung für die Kombination von Festigkeit und Zähigkeit. Eigenschaften, die sich eigentlich gegenseitig ausschließen.

Die Realisierung solcher hoch geordneten Strukturen ist bei synthetischen Polymer-Schichtsilikat-Nanokompositen jedoch nicht so einfach zu verwirklichen. Abgesehen von der variierenden Qualität des Schichtsilikats und unzureichenden Herstellungsmethoden, ist die Phasensegregation ein weit verbreitetes Problem. Die Phasensegregation stellt nicht nur ein Problem bei der Reproduzierbarkeit dar, sondern macht auch eine systematische Variation der Parameter und deren Einfluss auf die Materialeigenschaften zu einer Herausforderung.

Diese Arbeit basiert auf der einzigartigen Fähigkeit, homogen geordnete eindimensional- (1D) kristalline Nanokompositfilme durch Spray Coating herzustellen. Diese dienen als Modellsysteme zur Untersuchung der thermoelastischen, mechanischen und Gasbarriereeigenschaften. In der Literatur werden solche 1D-Kristalle als hybride Bragg-Stapel bezeichnet. In dieser Arbeit werden zwei Polymer/Schichtsilikat-Systeme vorgestellt, die die Realisierung einer 1D-kristallinen Anordnung von Schichtsilikat-Nanoplättchen für zwei unterschiedliche Polymergehalte ermöglichen: Polyvinylpyrrolidon (PVP) und Polyethylenglykol (PEG).

Ein Faktor, der diese Synthese ermöglicht, ist der verwendete synthetische Natriumfluorohectorit (Hec) und dessen einzigartiges und seltenes Phänomen der repulsiven osmotischen Quellung. Die resultierenden Nanoplättchen von gleichmäßiger Dicke bilden nematische flüssigkristalline Phasen. Mischt man diese Hec Phase mit einem Polymer, bildet sich eine perfekt homogene nematische Hybridphase aus. Durch Spray Coating wurden transparente, selbststehende und monokristalline Filme hergestellt.

Durch eine sorgfältige Anpassung des Hec zu PVP-Gehalts kann der Schichtabstand im Bereich von 1,9 bis 3,8 nm eingestellt werden. Die einzigartigen geordneten 1D-Hybridfilme in Kombination mit fortschrittlichen Charakterisierungsmethoden ermöglichen die Bestimmung der richtungsabhängigen thermoelastischen Eigenschaften. Die Anisotropie der Wärmeleitfähigkeit innerhalb und senkrecht zur Stapelrichtung ist für ein elektrisch isolierendes Hybridmaterial

erstaunlich hoch. Darüber hinaus zeigt sich die strukturelle Anisotropie der Hybridfolien auch in der Anisotropie der richtungsabhängigen E-Module. Obwohl das Polymer-Confinement der Hybridfilme sehr stark ist, zeigen Dichte, spezifische Wärme, Wärmeleitfähigkeit innerhalb zur Stapelrichtung und alle mechanischen Moduli ein effektives Mediumverhalten. Die Wärmeleitfähigkeiten senkrecht zur Stapelrichtung gehorchen jedoch nicht einer einfachen Mischungsregel, da der Wärmetransport senkrecht zur Stapelrichtung stark von der Schichtsilikat/Polymer-Grenzfläche bestimmt wird.

Die hybriden Bragg-Stapel mit einem PVP-Gehalt von 40 und 31 Vol.-% unterscheiden sich nur in der Füllstoffbeladung und sind hinsichtlich Füllstofftyp, Aspektverhältnis, Texturqualität und eindimensionaler Kristallinität vergleichbar. Die Schichtabstände von 2,3 bzw. 3,0 nm entsprechen einer Mono- bzw. Doppelschicht aus PVP. Da die Höhe der Zwischenschicht kleiner als der Gyrationsradius des Polymers ist, erfährt das Polymer ein starkes Confinement. Daher stellen die hybriden Bragg-Stapel ein perfektes Modellsystem dar, um den Einfluss des Polymer Confinements auf die Permeabilität zu untersuchen. Die Theorie von Cussler besagt, dass die Permeabilität nicht-linear vom Aspektverhältnis und dem Volumenanteil des Schichtsilikats abhängt. Im Rahmen dieser Untersuchung wird jedoch ein zusätzlicher nichtlinearer Effekt des Confinements auf die Permeabilität festgestellt.

Schließlich wird die Kombination von Mono- und Doppelschichten aus Hec und PEG verwendet, um hybride Bragg-Stapel herzustellen, die sich in der Dicke der Hec-Schichten, der Dicke der Polymerschichten und dem Durchmesser der Nanoplättchen unterscheiden. Die Füllstoffgehalte können im Bereich von 73 bis 91 Gew.-% eingestellt werden. Der Füllstoffgehalt von 91% stellt dabei den Rekordfüllstoffgehalt in einer Perlmuttanaloga auf. Diese hochgefüllten hybriden Bragg-Stapel erlauben es, die Bulk-Mechanik systematisch zu untersuchen. Allerdings zeigt nur der hybride Bragg-Stapel, der aus einer Monolage Hec und zwei Lagen PEG besteht, ein duktiles Verhalten mit einer Dehnung von 8 % und einer Streckgrenze von 48 MPa. Zusammenfassend lässt sich sagen, dass die Duktilität des hybriden Bragg-Stapels verloren geht, wenn man die Dicke der PEG-Entkopplungsschicht reduziert, Doppelschichten von Hec verwendet und den Nanoplättchen-Durchmesser erhöht.

3 Introduction

Natural materials have been recognized as a source of inspiration, as they offer optimized solutions for problems, which have been carved out in an evolutionary process lasting millions of years. By studying nature, these inspirations can be transferred to the design of new and innovative materials. The Italian Leonardo da Vinci is considered as pioneer of this principle.[1] In 1505, he studied the flight of birds and bats and used his observation to design flying machines. Nowadays many more examples can be found, where nature's bag of tricks serves as a model, ranging from the lotus effect for dirt repelling house facades, to Velcro fastener, to the ventilation system of termite buildings for ventilation elements in office buildings. Also in the field of composite materials, natural materials like bone, wood or nacre serve as inspiration as they uniquely combine the mutually exclusive properties toughness, strength and stiffness and in addition are lightweight.[2] These unquestionably exclusive combinations of properties were found to be difficult to achieve with synthetic materials, even though an unlimited combination of elements, harsher temperatures and pressures can be used. Therefore, it is only logical that scientists and chemists have made efforts to synthesize composites inspired by natural materials. Nanocomposites are multiphase materials consisting of two or more components with different physical or chemical properties. Nanocomposites are further characterized by at least one component having dimensions of less than 100 nm or structures with repeating distances of the two components in the nanometer range.[3] It is the goal to form a defined nanoscale structure and synergistically improve the material's properties beyond the properties of the individual constituents. Generally, nanocomposites can demonstrate different or enhanced mechanical, electrical, optical, electrochemical, catalytic, and structural properties than those of each individual constituent.[4] Nanocomposites can contribute to solve the problems of the 21st century, namely the climate change and the gentle and responsible use of resources. With lightweight composites, replacing steel in the automotive and aviation sector, the carbon dioxide emission and fuel consumption is reduced. Moreover, the improved gas barrier of nanocomposites and their use in plastic packaging leads to an enhanced shelf life of food. Therefore, it is not surprising that the global market for nanocomposites is estimated to grow from \$ 2.0 billion in 2017 to \$ 7.3 billion in 2022.[5] These are promising prospects and one more reason to concentrate on nanocomposites. In the following, this thesis will focus on polymer-clay nanocomposites.

3.1 Layered 2D materials - Smectites

Like graphite oxide, layered double hydroxide, and layered titanate, clay belongs to the class of two-dimensional (2D) layered materials, defined by their anisotropic (directional dependence of properties) bonding. Generally, layered materials exhibit strong covalent bonding within the layer (in-plane) and comparatively weak forces between adjacent layers, holding the tactoids (a stack of layers) together. This anisotropic bonding leads for instance to the desired intracrystalline reactivity[6] or to the loss of the long-range three-dimensional (3D) order.[7]

Clay minerals can be divided into groups depending on the layer charge, structure and composition of the octahedral sheet (OS). As smectites (montmorillonite (MMT), hectorite) are the main choice for polymer-clay nanocomposites, due to their rich intracrystalline reactivity and swelling ability, we will further concentrate on this group of clays. Smectites are 2:1 layered clays, consisting of two tetrahedral sheets (TS) and one OS in the middle (Figure 1). The TS consists of SiO_4^{4-} tetrahedra, which are linked together by three basal oxygen atoms, building up the 2D lattice with hexagonal cavities. The fourth oxygen atom, the apical oxygen atom, is connected to the OS. The OS consists of various cations, for example Mg^{2+}, Li^{+}, Al^{3+}, being coordinated by four oxygen atoms shared with the tetrahedral sheet and two additional fluoride or hydroxyl groups. Structures with six octahedral sites occupied are referred to as trioctahedral structure (hectorite), whereas in dioctahedral structures (MMT) only four of the six octahedral sites are occupied. Isomorphous substitution of a higher valent cation against a lower valent cation within the TS and/or OS, leads to a negative layer charge. In case of smectite clays, the resulting layer charge ranges from - 0.2 to - 0.6 per formula unit and is counterbalanced by cations in the interlayer space between adjacent layers. The basal spacing (d_{001} also defined as d-spacing) is the sum of the interlayer height and the platelet (TS-OS-TS) thickness and represents the periodicity along the stacking direction.[6] For instance, the basal spacing of hectorite is 9.67 Å (Figure 1).

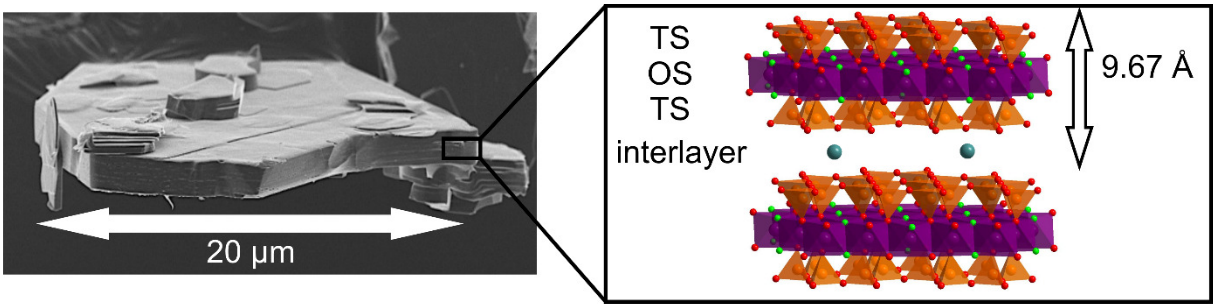

Figure 1: Scanning electron microscopy (SEM) image of a synthetic sodium fluorohectorite tactoid and the characteristic structure of hectorite with TS-OS-TS and interlayer. SEM image reprinted with permission from Reference 23. Copyright 2014 American Chemical Society.

The type of the interlayer cation influences the mechanical properties[8] and the stage of hydration.[9] Furthermore, the interlayer cations can be exchanged with various positively charged ions or molecules. This intracrystalline reactivity is a unique characteristic for layered materials and especially the exchange with organic cations renders smectite the perfect candidate for nanocomposites. Due to this modification, the initially highly hydrophilic smectite becomes more hydrophobic. The thus lower surface energy is required to achieve an incorporation of clay into hydrophobic polymers.[10] However, for a homogeneous intracrystalline reactivity, a homogeneous charge density is mandatory. The charge homogeneity is affected by the isomorphous substitution, which in turn is highly influenced by the synthesis temperature. Temperatures above 1000 K are required to prevent the clustering of different cations into domains of higher and lower charge density. In natural clays with lower synthesis temperatures (< 400 K), this clustering cannot be prevented. This finally also affects the intracrystalline reactivity, becoming noticeable during modification, swelling or osmotic delamination.[11] Moreover, natural clays lack of phase purity and optical quality, due to impurity phases and incorporated coloured transition metals like iron. Additionally, natural clays exhibit smaller platelet diameters than some synthetic clays. As the permeability of gases is nonlinearly dependent on the aspect ratio (ratio of diameter to layer thickness),[12] this is just another aspect to intensively study the synthesis of synthetic clays.

3.2 Synthetic sodium fluorohectorite - the gold standard

Breu and coworkers perfected the synthesis of a synthetic sodium fluorohectorite (Hec, $[Na_{0.5}]^{inter}[Mg_{2.5}Li_{0.5}]^{oct}[Si_4]^{tet}O_{10}F_2$) by combining melt synthesis with subsequently long-term annealing at 1040°C.[13-14] The resulting Hec impresses with phase purity, large platelet diameter of 18 µm (Figure 1), homogeneous charge density and a resulting uniform intracrystalline reactivity. The homogeneous intracrystalline reactivity not only leads to discrete hydration steps in humid air, but also to the complete and spontaneous delamination of the tactoids into single, individual layers with a height of 1 nm, when immersed in deionized water. In the first swelling regime, the crystalline swelling, one, two or three water layers are realized, related to the relative humidity (RH) and the type of interlayer cation. For Hec, the nonhydrated structure at 0% RH shows a *d*-spacing of 0.96 nm (Figure 1).[14-15] At 43% RH, the *d*-spacing increases to 1.25 nm and three water molecules coordinate the sodium cation. In this one-layer hydrate, sodium is located either towards the upper or the lower TS and is thus in close contact with basal oxygen atoms of the TS.[15] In the two-layer hydrate, at almost 100% RH, six water molecules coordinate sodium and the *d*-spacing grows to 1.55 nm.[14] Sodium is located in the middle of the interlayer space, while the water molecules can form hydrogen bonds with the basal oxygen atoms of the TS.[15] When immersing Hec powder into ultrapure water, Hec gently and completely delaminates into individual single nanoplatelets with a thickness of about 1 nm, while the initial diameter of the platelet of 18 µm is preserved. The distance between adjacent nanoplatelets increases related to the added amount of water.[6, 16] The homogeneous swelling can be studied by small angle X-Ray scattering (SAXS). The rare phenomenon of osmotic swelling[17] is for instance also observed for layered titanates[18] and is a thermodynamically favored, repulsive process. Because of the large platelet diameter, the free rotation of individual platelets is even in dilute suspensions (< 1 vol%) not possible, and nematic phases are formed. In suspension, the negatively charged platelets arrange parallel in a cofacial arrangement with distances of more than 55 nm between adjacent nanolayers.[16]

For 2D layered materials, the properties of such nanometer thick nanoplatelets change compared to bulk properties. The Hec nanoplatelets for instance are highly flexible with an in-plane modulus of 142 GPa,[19] as determined by a wrinkling technique. Not only can the mechanical properties change but also the thermal properties. For instance, the thermal conductivity of disordered randomly stacked single layers of WeS_2 is 30 times smaller, compared to the bulk single WeS_2 crystal.[20]

Moreover, the homogeneous charge density accompanied by the homogeneous intracrystalline reactivity of Hec, opens up the opportunity to a selective exchange of the interlayer cations. The Coulomb interaction between the negatively charged layer and the positively charged interlayer cations, fosters the segregation of cations of different size and hydration into different interlayer spaces.[13, 21] The Coulomb attraction favours this segregation as in this way the average basal spacing is minimized and consequently the Coulomb interaction for this system is maximized. Carefully adjusting the ratio of different cations, it is possible to synthesize ordered interstratifications with alternating layers of inorganic - organic intercalation compounds [22-23] or swelling - nonswelling cations.[21] If these ordered interstratification structures still contain an osmotically swelling sodium interlayer, the structure will spontaneously delaminate into double stacks (DS) in deionized water. The double stacks consist of two highly transparent and flexible silicate layers, encapsulating a central ion or an air / humidity sensitive organic molecule. The in-plane modulus of such a double stack with ammonium in the interlayer was determined to be 171 GPa, by applying a wrinkling technique.[24] Also in this case, the applied wrinkling technique verifies the extreme flexibility of these double stacks.

3.3 Polymer-clay Nanocomposites

The Toyota research centre synthesized one of the first polymer-clay nanocomposites in the 1990s. By in-situ polymerization of ε-caprolactam with organo-modified MMT, a Nylon 6 - MMT nanocomposite was produced. MMT was fully delaminated and uniformly dispersed in the polymer matrix. The resulting nanocomposites impressed with enhanced mechanical, and gas barrier properties, an improved electrical conductivity, and a decreased thermal expansion coefficient.[25-27] The significant improvement of the engineering properties by reinforcing polymers with clay on the nanoscale, resulted in extensive research in this field.

The synthesis of polymer-clay nanocomposites is difficult and several processing methods like in-situ polymerization,[27] solution (suspension) blending with subsequent self-assembly[28] and melt processing[29] exist. Each strategy has advantages and drawbacks and results in nanocomposites of varying quality. Overall, the term nanocomposite is not clearly defined, as it covers a wide range of nanocomposites with variations in clay content, quality of clay distribution within the polymer matrix, quality of clay (natural or synthetic clay) and aspect ratio. It is therefore important to be aware of these differences and to take a differentiated approach when comparing several composites.

The term nanocomposites includes nanocomposites with exfoliated stacks or completely delaminated single nanoplatelets. Generally, exfoliation describes the process of slicing tactoids into thinner stacks, whereas during delamination, the tactoids were exfoliated to the level of an individual nanoplatelet.[6] As discussed above, delamination and exfoliation highly depends on the uniform intracrystalline reactivity, resulting in turn from charge homogeneity. For Hec, this precondition is achieved by long term annealing. However, for some synthetic clays or natural clays, a homogeneous charge density is not given. Thus, delamination is prevented and a mixture of mono, few- and multilayer stacks exist. An example for a polymer-clay nanocomposite, consisting of multilayer stacks smaller than 100 nm is given in Figure 2A. In Figure 2B, delaminated nanoplatelets are randomly dispersed in the polymer matrix and an isotropic nanocomposite is formed. It is undeniable that even small clay loadings improve the physical properties of nanocomposites.[28, 30] However, the aspect ratio, which is influenced by exfoliation or delamination, and the filler content are significant and crucially affect the nanocomposite's properties like permeability[12, 31] or bulk modulus[32] in a highly nonlinear manner. Moreover, the distribution of the filler within the polymer matrix is important. In such inhomogeneous isotropic and low-filled systems (Figure 2A-B), the permeability of the nanocomposite is not sufficiently reduced by the creation of a tortuous path. Overall, delaminated systems with higher filler contents are favored.

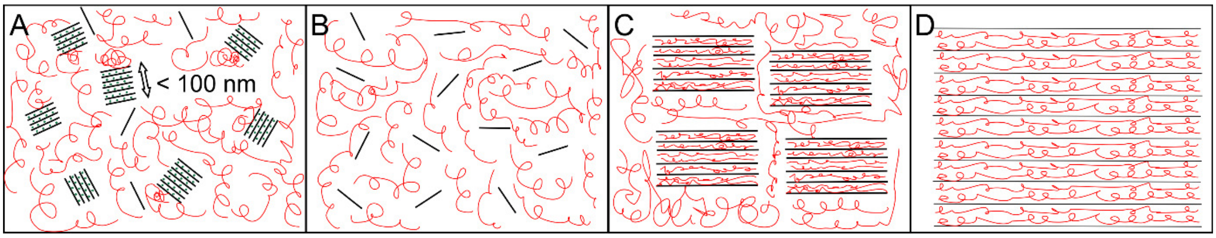

Figure 2: Schematic of different nanocomposites consisting of polymer (red) and clay platelets (black). A) Nanocomposite containing a mixture of mono- few- & and multilayer stacks. B) Nanocomposite with delaminated platelets and low filler content isotropically dispersed. C) Phase-segregated nanocomposite, with a polymer-rich phase and an intercalated phase. D) Hybrid Bragg stacks with strictly alternating nanoplatelets and polymer layers.

Higher filler loadings in combination with delaminated nanoplatelets strengthen the impact of the interface. Assuming a homogeneous distribution of the nanoplatelets within the nanocomposite and a clay content greater than 30 vol%, the interlayer space between adjacent nanosheets is as narrow as 2 nm. The available interlayer space is consequently even smaller than the radius of gyration of the interlayered polymer. Obviously, such a polymer confinement also affects the properties of the confined polymer as compared to the bulk properties. In literature, the impact of the confinement on the segment mobility,[33] glass transition temperature (Tg),[34-37] and viscosity[38] was proven. In chapter 4.2 the influence of polymer confinement on permeability is demonstrated.[39]

Homogeneous suspensions with delaminated nanoplatelets and high filler loadings can form two distinct structures during drying. The resulting nanocomposite can either be a two-phase intercalated nanocomposite or a single-phase hybrid Bragg stack (Figure 2C-D). In a two-phase nanocomposite, phase segregation is observed and a polymer rich and an intercalated phase, with polymer being intercalated in the interlayer space, coexist. Phase segregation is driven by thermodynamics, is likely to happen[40-44] and creates a problem with reproducibility.[45] A perfect example is a mixture of Hec and polyethylene glycol (PEG). [33, 45] At a composition of 31 vol% Hec and 69 vol% PEG, a segregated polymer rich phase and an intercalated phase coexist. The polymer dynamics were studied by nuclear magnetic resonance. [33] The identified molecular mobilities varied and were attributed to strongly immobilized (intercalated) and mobile (segregated) polymer phases.[33] Nevertheless, PEG is known to form intercalated phases with two different PEG volumes, as phase segregation can be counterpoised by the interaction with the interlayer cation.[46] In chapter 4.3 single-phase materials with two different PEG contents, corresponding to a basal spacing of 1.8 and 1.4 nm were synthesized. In literature, this 1D crystals are referred to a hybrid Bragg stack.[47]

3.4 Hybrid Bragg stack

Hybrid Bragg stacks and their 1D crystallinity can be verified by XRD measurements and TEM microscopy images. According to Meuring's rules,[48] the 1D crystallinity is determined in XRD pattern by a (perfectly) rational *00l* series, which is expressed by a low coefficient of variation (CV). Furthermore, they are characterized by a small full width at half maximum (FWHM), intensive reflections and the match of calculated and observed *d*-spacing. In the following, the synthesis and identification of hybrid Bragg stacks will be investigated for the Hec/PEG system (also see chapter 4.3).

As stated above, for a Hec to Peg ratio of 50:50 wt% (31:60 vol%), a two-phase nanocomposite with a polymer rich phase and an intercalated polymer phase is observed. How was this verified? Assuming in a first approximation that the intercalated polymer has the same density as in bulk, the expected *d*-spacing of the nanocomposite can be calculated. First, the volume content of Hec and PEG are calculated by assuming PEG and Hec densities of 1.2 and 2.7g cm^{-3}, respectively.[49] Based on a simple geometric consideration using the Hec thickness of 0.96 nm and the corresponding volume content of Hec, the *d*-spacing can be calculated.[41, 50]

For a mixture of 50:50 wt%, corresponding to 31:60 vol% a *d*-spacing of around 3.1 nm is calculated and therefore expected. However, the observed *d*-spacing is only 1.8 nm. Consequently, the composite is phase segregated in a polymer phase and an intercalated phase with a *d*-spacing of 1.8 nm. Although segregated amorphous polymer domains cannot be detected with XRD measurements, phase segregation can nevertheless be confirmed as the calculated and observed *d*-spacing do not match.

Generally, a single-phase nanocomposite can be produced by exactly adjusting the clay to polymer ratio in order to match the *d*-spacing of the intercalated domains. This adjustment may yield a single-phase material of of 1D crystallinity, displaying long-range periodicity along the stacking direction. If we look at the example of Hec/PEG again, a hybrid Bragg stack can be produced, if the PEG to Hec ratio is specifically adapted exactly to the ratio of the intercalated domains of 1.8 nm. This is fulfilled at a content of 54 vol% Hec. For this composition, the calculated and observed *d*-spacing of 1.8 nm match (Figure 3A). This accordance suggests that within experimental error, the available PEG is included in the periodic domains and no extra segregated PEG volume exists. A homogenously ordered, 1D crystalline hybrid Bragg stack is formed. The XRD pattern show a rational 00l series up to the 5th order and a CV of 0.18%. In general, large CV values (> 3%)[48] and large variations in FWHM indicate non-rationality of the diffraction pattern, caused by a random interstratification of different interlayer heights.

Moreover, a second intercalated phase is known in literature with a periodicity of 1.4 nm.[46] By optimizing the volume content of PEG, a hybrid Bragg stack is observed for 70 vol% of Hec with a *d*-spacing of 1.4 nm (Figure 3B; see also chapter 4.3). The XRD pattern verify the 1D crystallinity by a rational *00l* series up to the 4th order with sharp and intense reflections, a low FWHM and a low CV of 0.63%. In addition, calculated and observed *d*-spacing match.

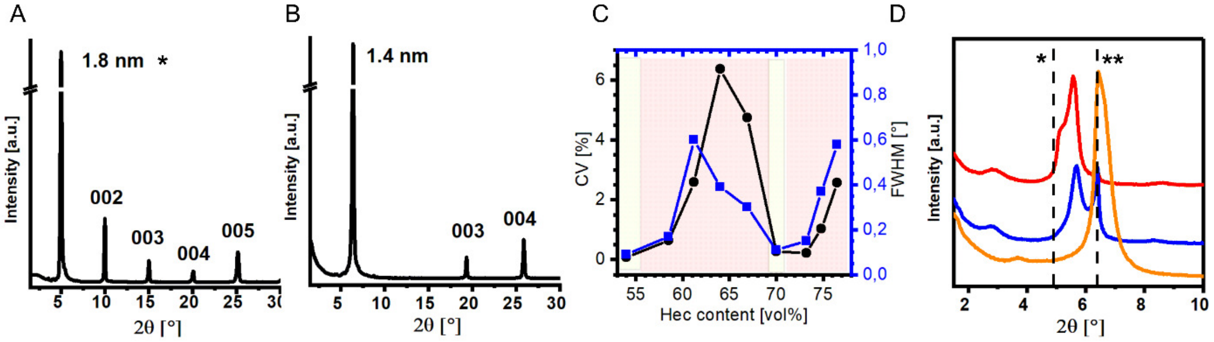

Figure 3: XRD pattern and study of CV and FWHM. A) XRD pattern of the hybrid Bragg stack with a Hec content of 54 vol%, showing a *d*-spacing of 1.8 nm and a rational series up to the 5th order. B) XRD pattern of the hybrid Bragg stack with a Hec content of 70 vol% showing intense reflections. C) Variation of CV (black circle) and FWHM (blue square) with varying Hec weight content. The minima at a Hec content of 54 and 70 vol% confirm the best 1D periodicity. D) XRD patterns of the *001*-reflection at a Hec content of 61 vol% wt% (red),67 vol% (blue) and 77 vol% (orange). The lines marked with asterisks correspond to the basal spacing of the hybrid Bragg stacks with a Hec content of 54 vol% (*) and 70 vol% (**).

As stated before, instruments for the identification of hybrid Bragg stacks are CV, FWHM, intensity and maximum visible order of the *00l* series. These characteristics and their correlation provide valuable information about the existence of hybrid Bragg stacks and the quality of the 1D crystalline order. As already mentioned, the interlayer height is smaller than the radius of gyration and consequently, the polymer experiences strong confinement. The interlayer height corresponds to the dimensions of the polymer chains. As a result, the interlayer height can only be changed in defined steps, related to the diameter of the polymer chain. As stated above, the XRD patterns of hybrid Bragg stacks, which are periodically homogeneous over long ranges, show nicely rational *00l*-series as indicated by low CVs. Moreover, the FWHM of individual reflections are very similar. If the height of the PEG layers, sandwiched between Hec nanoplatelets varies, the *00l* reflections would instantly and with high sensitivity broaden and result in irrationality. Even slight deviations from the ideal composition lead to significant increases in CV and FWHM of the *00l* reflections.[37] The formation of a hybrid Bragg stack can therefore also be tracked by studying CV and FWHM at different Hec contents. The curves for CV and FWHM show indeed a minimum for 54 and 70 vol% Hec (Figure 3C).

In addition, the XRD patterns with varying contents of Hec are investigated and vividly show the change from the hybrid Bragg stack with 54 vol% to the second hybrid Bragg stack with a higher filler loading of 70 vol% (Figure 3D). It is clear, that the interlayer space can only be varied in defined and discrete steps related to the dimensions of the intercalated polymer. Consequently, with decreasing PEG content, a random interstratification of two layers of PEG and one layer of PEG appears. If the interlayer height varies randomly within the coherence length of the X-ray beam, a weighted average of the *d*-spacing is observed.[7] The position of the *00l*-reflection lies in between the positions of the real *d*-spacing for the hybrid Bragg stacks. The experimentally observed but virtual *d*-spacing shifts continuously with the real frequency of the two different layer spacings.[7] This observation can be studied for the XRD pattern of the nanocomposite with a Hec content of 61 vol% (Figure 3D, red). As the PEG content decreases, the *d*-spacing continuously moves to smaller *d*-spacings, accompanied by a broadening of the *001* reflection and a visible shoulder. If the basal spacing however varies randomly out of the coherence length of the X-ray beam, two distinct reflections are observed. This is observed for the nanocomposite with a Hec content of 67 vol%. Further decreasing the PEG content below the composition of the hybrid Bragg stacks directly result in a broadening of the *001*-reflection peak for the nanocomposite with a Hec content of 77 vol% (Figure 3D, orange).

Apart from the Hec/PEG system, a second polymer/clay combination was identified, where hybrid Bragg stacks can be produced. By applying synthetic Hec and polyvinylpyrrolidone (PVP),[51] the interlayer space can be tuned from 2.0 nm to 1.3 nm, caused by a mono- and a bilayer of PVP. More details are given in chapter 4.1.

3.5 Nacre

Biological composites like bamboo, bone or nacre always inspired scientists for the fabrication of advanced, multifunctional materials. Especially the combination of strength and toughness is desirable, but also seems to be mutually exclusive. Why is this the case? How can natural materials defeat the conflict of strength versus toughness? For a deeper understanding, it is first necessary to explain the properties strength and toughness. Strength is the material's resistance to permanent (plastic) deformation, measured as stress.[52] In contrast, toughness is the material's resistance to a fracture, measured as energy needed to cause fracture.[52] An important requirement for toughness is the ability of a material to dissipate local high stresses by a limited deformation. A limited deformability (ductility) is therefore a prerequisite. In natural materials, the processes that allow limited deformation are widely diverse and will later be examined for nacre. Knowing that toughness requires limited deformation, while strength is the resistance to this deformation, it is not surprising that the combination of these two properties is unique. Generally, a strong material tends to be brittle, whereas deformable, lower strength materials tend to be tough.

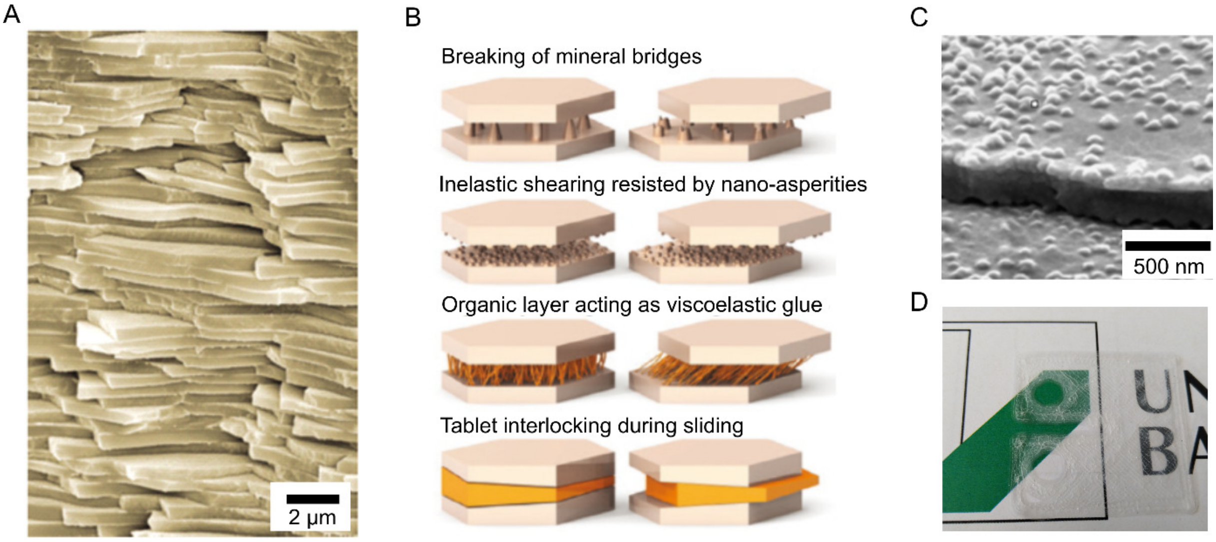

Figure 4: Images and schematics of nacre and a 3D bulk nacre-mimetic. A) Brick and mortar structure of nacre and B) schematic illustration of the different toughening mechanisms in nacre. A) and B) reprinted with permission from Springer Nature Customer Service Centre GmbH: Nature, Nature Materials, Reference 2, Copyright 2014. C) Asperities on the aragonite surface. Reprinted from Reference 54, Copyright 2008, with permission from Elsevier. D) 3D bulk nacre-mimetic obtained by 3D printing.

One prominent example is nacre, a hard-soft composite, hierarchically arranged in a so-called "brick-and-mortar" structure (Figure 4A). Nacre consists of 95 vol% strong aragonite ($CaCO_3$)

platelets (~200-900 nm thick with a diameter of 5-8 µm) separated from each other by a thin layer of organic biopolymer (~10-50 nm thick).[2] This strictly alternating arrangement resembles hybrid Bragg stacks mentioned earlier. The ceramic mineral provides the high strength of nacre. However, without the dissipative nature of the biopolymer, the directly connected platelets would be unable to distribute local high stresses and nacre would be brittle. The minor organic phase acts as a lubricant and allows sliding of the platelets.[53] However, the sliding must be limited, as otherwise nacre would lose its strength. The considered mechanism restraining the sliding range from the molecular to the micrometer level (Figure 4B) are mineral bridges connecting platelets,[54] nanoscale asperities on the aragonite surface (Figure 4C),[55] platelet interlocking due to corrugated platelets,[56] and the breakage of sacrificial bonds in the viscoelastic biopolymer.[57] Further toughening mechanisms are crack bridging, which result in a tortuous crack path, and the pull-out of mineral platelets.[52] In tensile tests, the strength and Young's modulus of nacre were determined to be 140 MPa and 60 GPa,[58] respectively. The determined toughness (1.24 kJ m^{-2}) is about 3000 times higher compared to monolithic $CaCO_3$.[59]

For mimicking nacre, the used inorganic materials as hard component are more than diverse and range from clay,[60] graphene oxide,[61] and alumina[62] to glass flakes.[63] A wide variety of polymers are mainly used as soft component and in few works, a glass-forming alloy is used.[64] A controlled and defined alignment of both components is a precondition for good mechanical properties and various processing methods with varying control over the structure were examined. Common methods are layer-by-layer deposition,[65] vacuum filtration,[66] evaporation or solution casting,[67] and evaporation induced self-assembly.[60] However, these methods are limited to 2D films. Lately, 3D bulk nacre-mimetics were produced by ice templating and sintering of ceramics,[64] magnetic particle alignment,[68] lamination and hot pressing.[44, 69] With 3D materials, the mechanical characterization can be performed with even more testing methods, which require mm or cm thick samples, and enables also to study the crack propagation. The centimeter thick laminates of self-assembled clay/polymer nanocomposite films showed crack deflection, microcracking and uncracked ligament bridging, comparable to nacre. [44, 70] Nevertheless, the growing direction of the crack is between the clay platelets, rather than cross-plane, which suggests that a stronger adhesion between the platelets is required. In this context, features not yet realized for clay-based nacre-mimetics are mineral bridges and nanoasperities, which contribute as toughening mechanism. The groups of Deville[64] and Studart[63, 68, 71] intensively studied this topic. Theoretical analysis and experimental observations reveal that strength and elastic modulus increase linearly with the relative fraction of mineral bridges. Moreover, the tension transfer in the entire stiff phase is enhanced, leading to an increased bending strength.

In the following, we will concentrate on clay-based nacre-mimetics. Typical nacre characteristics like mineral bridges, nanoasperities or platelet interlocking are difficult or at least not yet realized. Therefore, a tighter focus must be on the homogeneously ordered arrangement of clay and polymer, the design of the polymer itself and the polymer-polymer and polymer-clay interface.

As stated in chapter 3.4, the fabrication of strictly alternating clay nanoplatelets and polymer layers in so-called hybrid Bragg stacks is challenging. However, some processing methods provide too little control over the structure. Layer-by-layer deposition for instance is unsuitable to prevent direct platelet-platelet contact, as during one cycle several platelets or polymer chains were deposited. More suitable methods are evaporation induced self-assembly or spray-coating. We recently proved that spray-coating is superior to doctor-blading, as it yields higher ordered structures.[41] Moreover, the usage of natural clays is a drawback due to the limited delamination. Suspensions of commonly used clays contain mixtures of auxiliary minerals, mono-, few-, and multilayer stacks. This consequently results in higher disorder and direct platelet-platelet contact. In addition, phase segregation is likely to happen for a wide range of polymers like polyvinyl alcohol,[42, 44] glycol chitosan[72] or PEG.[33, 45] With such intercalated but still phase-segregated nanocomposites, a systematic investigation of the influence of the polymer content on the mechanical properties is not possible.

Apart from the homogeneous alignment, the design of the polymer itself and the interface between polymer-clay and polymer-polymer is important. Especially early works concentrate on high Tg polymers.[44] Additionally, strong covalent[60, 73] or ionic bonds[74-75] were integrated either by post infiltration or by a suitable polymer. These attempts resulted in strong and stiff nanocomposites, characterized by high tensile strengths and Young’s moduli. For the realization of tough nanocomposites with increased elongation by frictional sliding, a low Tg polymer is required[76]. Moreover, sacrificial bonds for a stress-induced opening and rebinding are required for a concomitantly stiff and tough material. As covalent and ionic bonds are too strong, weaker hydrogen bonds are the choice. A low Tg non-ionic copolymer with ureidopyrimidinone (UPy) as 4-fold hydrogen bonding unit allowed to adjust the mechanical properties from brittle to ductile.[77] The nanocomposite with 30 mol% of UPy units is brittle and stiff with a Young’s modulus of 40 GPa, a tensile strength of 265 MPa and a limited elongation of 1.3 %. Unsurprisingly, the too high amount of supramolecular hydrogen bonds inhibits frictional sliding of the nanoplatelets and inelastic deformation. However, reducing the UPy content to 13 mol%, a ductile material with an elongation of 8% and a still considerable high Young's modulus of 22 GPa is generated. Moreover, a nanocomposite with synergistically improved stiffness and toughness could be realized by combining a stiff, high Tg polymer (PVA) and a ductile, low Tg polymer (polyvinylamine).[78] Compared to the 4-fold binding unit UPy, the formed hydrogen bonds are weaker, but present in larger amounts. The nanocomposite showed an elongation of close to 50% and a very high toughness (> 27 MPa).

Note that all clay containing nacre-mimetics are defined by high filler loadings. If clay is delaminated in 1 nm thick nanoplatelets, in composites with a ratio of clay to polymer of 50:50 wt%, the interlayer between adjacent nanoplatelets is as small as 2 nm and falls beneath the polymer's radius of gyration. The polymer features strong confinement, which alters the polymer's properties. In this context, the change in segment mobility and glass-transition temperature are of major importance. The potential of greater flexibility and deformability of low Tg polymers can therefore not be exploited. Moreover, confinement forces polymer chains in a more or less stretched state and entanglements are hindered. This in turn inhibits the dissipation of energy by the breaking and reforming of sacrificial bonds. In contrast to highly filled nanocomposites with clay and polymer thicknesses around 1 nm and 2 nm, respectively, the dimensions of inorganic and organic phase in nacre are completely different. Aragonite has a thickness of 200-900 nm with a diameter of 5-8 µm, the aspect ratio ranges from 25 to 9. The corresponding organic phase is 10-50 nm thick and thus entanglements of polymer chains are possible. Moreover, the Young's modulus of Hec itself is about two times higher compared to pure aragonite (commonly accepted value E = 70 GPa).[79] A sufficient strengthening could therefore also be achieved with a lower clay loading. Future nacre-mimetics should therefore focus on higher organic contents, associated with an increased interlayer space, which in turn decreases the confinement effects and allows polymer entanglement. The potential polymer should further possess hydrogen bonds as sacrificial bonds. Additionally, an enhanced stress transfer from the polymer matrix into the clay platelets should be realized, for instance with modifiers also interacting with the polymer phase or by polymers, which could be switched to be cationic by cleaving light-adaptive or thermo-reversible side groups. Moreover, the realization of mineral bridges could be tested by the silanization of hydroxyl groups bearing clays. Also new processing methods like 3D-printing should be considered. In preliminary experiments, with a 10 wt% suspension of Hec:PEG (73:27 wt%), promising structures could be printed (Figure 4D). This not only opens the opportunity to print thicker 3D bulk-materials but also to integrate different nanoplatelet orientations within one sample.

3.6 Mechanical Properties of Hybrid Bragg stacks

Generally, stress (σ) and strain (ε) of a body are interdependent. In the linear elastic region, Hooke's law (equation 1) applies. The constant of proportionality is called modulus of elasticity (E).

$$\sigma = E\,\varepsilon \tag{1}$$

In a 3D body, Hooke's law is expressed by a linear tensor equation of the 4th degree (equation 2). Here, the elasticity tensor C_{ijkl} characterizes the elastic properties of the deformed matter with 81 elastic constants. [80]

$$\sigma_{ij} = C_{ijkl}\,\varepsilon_{kl} \tag{2}$$

Due to the symmetry of the stress and strain tensor, the elastic constants can be reduced to 36, allowing the transformation of Hooke's law into a matrix equation. The elasticity tensor is replaced by a 6 x 6 matrix and the symmetric stress and strain tensors are presented as six-dimensional vectors, according to Voigt notation. In addition, the elastic tensor itself is a symmetric tensor, which reduces the maximum number of independent elements to 21 (equation 3):[80]

$$\begin{bmatrix}\sigma_1\\ \sigma_2\\ \sigma_3\\ \sigma_4\\ \sigma_5\\ \sigma_6\end{bmatrix} = \begin{bmatrix} C_{11} & C_{12} & C_{13} & C_{14} & C_{15} & C_{16}\\ C_{12} & C_{22} & C_{23} & C_{24} & C_{25} & C_{26}\\ C_{13} & C_{23} & C_{33} & C_{34} & C_{35} & C_{36}\\ C_{14} & C_{24} & C_{34} & C_{44} & C_{45} & C_{46}\\ C_{15} & C_{25} & C_{35} & C_{45} & C_{55} & C_{56}\\ C_{16} & C_{26} & C_{36} & C_{46} & C_{56} & C_{66}\end{bmatrix} \begin{bmatrix}\varepsilon_1\\ \varepsilon_2\\ \varepsilon_3\\ \varepsilon_4\\ \varepsilon_5\\ \varepsilon_6\end{bmatrix} \tag{3}$$

The number of independent elastic constants is further reduced if the studied material has symmetry elements. A transversely isotropic material has a plane within which the material's properties are isotopic. Perpendicular to this plane, the properties differ and the direction is favored.[81-82] This is also the case for hybrid Bragg stacks, in which the clay nanoplatelets are precisely oriented in the stacking direction, but are randomly arranged in the lateral direction, perpendicular to the stacking direction.[51] Because of the transversely isotropic symmetry class, the elastic tensor can be reduced to five independent elastic constants as follows (equation 4):[83]

$$\begin{bmatrix}\sigma_1\\ \sigma_2\\ \sigma_3\\ \sigma_4\\ \sigma_5\\ \sigma_6\end{bmatrix} = \begin{bmatrix} C_{11} & C_{12} & C_{13} & & & \\ C_{12} & C_{11} & C_{13} & & & \\ C_{13} & C_{13} & C_{33} & & & \\ & & & C_{44} & & \\ & & & & C_{44} & \\ & & & & & C_{66} = \dfrac{C_{11}-C_{12}}{2} \end{bmatrix} \begin{bmatrix}\varepsilon_1\\ \varepsilon_2\\ \varepsilon_3\\ \varepsilon_4\\ \varepsilon_5\\ \varepsilon_6\end{bmatrix} \tag{4}$$

The constants of the elastic tensor can be connected with the engineering mechanical properties.[84] In the following, the formulas for the direction-dependent elasticity modulus (Young's modulus), the cross-plane ($E_{\perp}$) and in-plane ($E_{\parallel}$) Young's modulus are shown (equation 5-6):

$$E_{\perp} = C_{33} - \frac{2\,C_{13}^2}{C_{11}+C_{12}} \tag{5}$$

$$E_{\parallel} = \frac{(C_{11}-C_{12})[C_{33}(C_{11}+C_{12}) - 2C_{13}^2]}{C_{11}C_{33} - C_{13}^2} \tag{6}$$

Here, the terms cross-plane and in-plane are connected to the stacking direction and the direction perpendicular to the stacking direction in the hybrid Bragg stack, respectively, rather than directions parallel or perpendicular to the symmetry axis.

In chapter 4.1 the direction-dependent mechanical properties of hybrid Bragg stacks will be probed with Brillouin light spectroscopy (BLS).

3.7 Tensile Test

For the estimation and determination of mechanical properties of materials, tensile tests are an important and common tool. Especially for thin 2D samples, like mostly obtained for nacre-mimetics, tensile tests allow their characterization. The sample geometry, testing temperature, RH, and test speed influence the results, why these values are standardized according to DIN EN ISO 527.[85] Moreover, anisotropy highly influences the mechanical properties and should therefore be considered. This is followed by preparing samples oriented parallel and perpendicular to the orientation/stacking direction. However, for most nacre-mimetics, the thickness is limited due to the processing method and only samples oriented parallel to the stacking direction are produced. Keeping this in mind, the tensile test of nacre-mimetics is highly influenced by the sliding of the platelets against each other.

In tensile tests, the samples are elongated with a constant speed and the change in length (ΔL) and the required force (F) are measured. The tensile stress values (σ) are calculated based on the initial cross-sectional area (A_0) of the sample (equation 7)

$$\sigma = \frac{F}{A_0} \tag{7}$$

The strain (ε) is calculated based on the initial length (L_0) of the sample (equation 8):

$$\varepsilon = \frac{\Delta L}{L_0}\, 100\% \tag{8}$$

In the linear elastic region, Hooke's law can be applied and the bulk Young's modulus, the modulus of elasticity, is calculated from the change in force $\Delta F = F_2 - F_1$ and the change in elongation $\Delta\varepsilon = \varepsilon_2 - \varepsilon_1$ (equation 9). The evaluation is limited to the deformation range from 0.05 % to 0.25 % in strain.

$$E = \frac{\sigma_2 - \sigma_1}{\varepsilon_2 - \varepsilon_1} = \frac{F_2 - F_1}{0.002\, A_0} \tag{9}$$

Note, that the determined bulk Young's modulus is not identical to $E_{\parallel}$, determined by the direction-dependent BLS.

Discussing the elastic properties of solids, one distinguishes between elastic and plastic deformation. In case of elastic deformation, the deformation is reversible and the stretched body obtains his original state, when the stress is not applied. The elastic region is further distinguished in a linear elastic region for low strain, in which a linear relationship applies between stress and strain, and a linear-plastic region, in which this relationship is nonlinear. In case of plastic deformation, the deformation is irreversible and goes along with the breaking of bonds. The transition between elastic and plastic region occurs at the yield point.

According to DIN EN ISO 527,[85] the following characteristic values are defined:

- Yield strength σ_Y: The first stress value, at which an increase in strain without an increase in stress is observed.
- Ultimate tensile strength σ_M: The maximum stress, observed during the experiment.
- Strength at break σ_B: Tensile stress at the moment of break.

The designation is identical for the observed elongation and thus one can distinguish between elongation at the yield point (ε_Y), maximum elongation (ε_M), and elongation at break (ε_B).

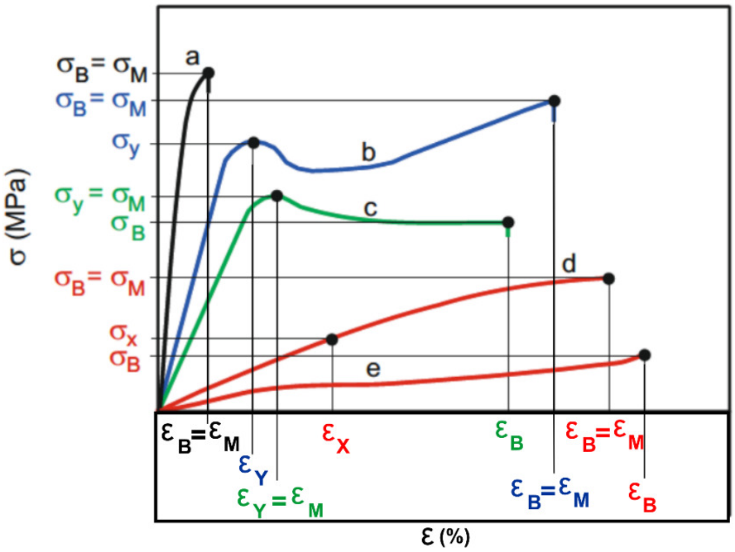

Figure 5: Characteristic stress-strain curves for different polymers: a) brittle polymer, b-c) ductile polymers with yield point, d) ductile polymer without yield point, e) elastomer. Reprinted and modified with permission from Reference 86. Copyright 2020, Carl Hanser Verlag.

In the following, characteristic stress-strain curves of different polymers will be studied and on this basis, the polymers will be divided into ductile and brittle materials (Figure 5).[86] A brittle polymer, is characterized by a high maximum tensile strength (σ_M) and a comparably low elongation at break (ε_B) (Figure 5a). The polymer is unable to deform plastically and therefore, the broken parts of the testing sample can be reassembled to the original shape of the sample. Ductile materials are characterized by their ability to yield and thus reach high elongations, but relatively low tensile strength (Figure 5b-d). In the linear elastic region, the stress-strain curves of type b) and c) are identical to type a), but show a lower slope, resulting in a lower modulus of elasticity. However, at the yield point, type b) and c) start to deform plastically going along with a local necking of the sample. In the following constant stress plateau, cold drawing is observed, whereby the stretched material pulls out of the unstretched part of the test specimen. The process goes along with an orientation of the molecules in stress direction. The cross sectional area in the necking region is steadily reduced until the material breaks abruptly, like for type c). The polymer of type b), however, shows the phenomenon of strain hardening and the resulting break at much higher stresses. The completely oriented and aligned polymer chains increase the strength and stiffness of the polymer in the stretched direction as the load is no longer absorbed by intermolecular forces but by the main valence bonds.[86] The stress-strain curve of type e) corresponds to an elastomer with low Young's modulus and tensile strength, but very high elongations at break.

4 Synopsis

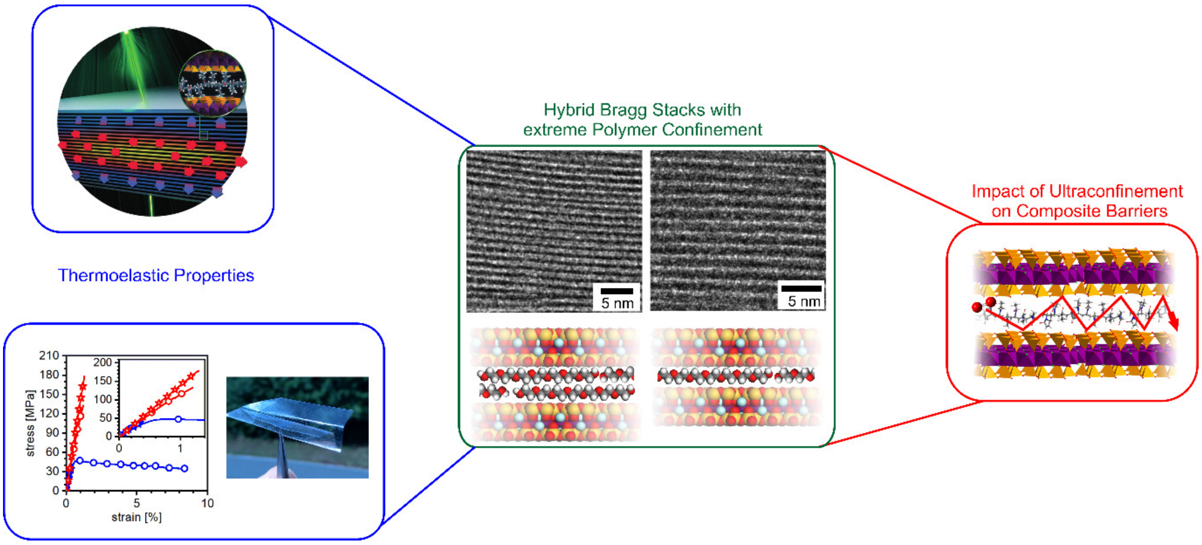

Figure 6: Schematic representation of the results of this work.

The present work contains two publications and one manuscript. For further publications I contributed to, please see list of publications.

All works are based on the unique ability to produce highly homogeneously ordered, 1D crystalline polymer-clay nanocomposite films. In literature, these 1D single crystals are referred to as hybrid Bragg stacks. Within this work, two polymer/clay systems are presented, that enable the realization of a 1D crystalline arrangement of clay nanoplatelets for two different polymer contents: PVP and PEG. These hybrid Bragg stacks mark a turning point for the characterization of nanocomposites in general and serve as model system for investigating the thermoelastic, permeability and mechanical properties.

The publication “Tunable Anisotropy in Hybrid Bragg Stack with Extreme Polymer Confinement” focusses on hybrid Bragg stacks, consisting of synthetic sodium fluorohectorite and polyvinylpyrrolidone (PVP), which allowed the first time to determine the direction-dependent thermoelastic properties. The anisotropy between the thermal conductivity studied in-plane and cross-plane was record-high. This strong anisotropy was also found for the direction-dependent Young’s and shear moduli. Moreover, the results from the thermal and mechanical analyses were correlated and the strong influence of the clay/polymer interface was highlighted.

The follow-up publication “Impact of Ultraconfinement on Composite Barriers” also builds on hybrid Bragg stacks system consisting of Hec and PVP and investigates the relation between permeability and relative humidity (RH). Also this study was only possible because of the targeted synthesis of two hybrid Bragg stacks, which are comparable with respect to aspect ratio, filler type, quality of texture and one-dimensional (1D) crystallinity, but only differ in the filler content. By studying the permeability with increasing RH we found evidence for an additional linear effect of confinement on the permeability.

In the manuscript “One-dimensional crystalline clay nacre-mimetics with record filler contents (73 wt% - 91 wt%): From brittle to ductile to brittle”, the hybrid Bragg stacks consisting of PEG vary with respect to nanoplatelet diameter, thickness of the polymeric decoupling layer and thickness of filler (utilization of Hec or DS). This allows to study the mechanical dependence on these parameters systematically. Only one sample, consisting of Hec monolayers and two layers of PEG was found to be ductile with an elongation of 8%. The ductility of the hybrid Bragg stack is completely lost when reducing the thickness of the PEG decoupling layer, utilizing DS and increasing the nanoplatelet diameter.

4.1 Tunable Thermoelastic Anisotropy in Hybrid Bragg Stacks with Extreme Polymer Confinement

Heat management is considered a key technology and could help to solve the central problem of the 21st century, global warming. Generally, heat management is divided into four fields, covering building insulation, passive cooling, thermoelectricity, and thermal interface materials. These fields illustrate the goal to control the elusive flow of heat across multiple length scales, materials, and most important in a direction dependent manner. An anisotropic heat transport is easily achieved with 2D materials, since these already inherently exhibit a structural anisotropy. High anisotropies are achieved when these “hard” 2D materials are combined with “soft” materials, like polymers. In principle, the anisotropy is enhanced for small stacking periodicities, disordered stacking, and by choosing constituents with large thermoelastic contrast. In dielectrical (partially) crystalline hybrid materials, phonons are the main energy carrier in heat transport. Thermal transport studies would therefore greatly benefit from understanding the direction-dependent mechanical properties. What are the requirements for an ideal model system for such a study? Such a model system should exhibit homogeneity, translational crystallographic symmetry, tunability with respect to filler loading, strong anisotropy, perfect texture, and transparency.

The hybrid Bragg stacks, consisting of synthetic Hec and PVP, fulfill all requirements. During spray coating and subsequently drying, the Hec nanoplatelets and PVP arrange in a homogeneously ordered structure. By varying the polymer content, the *d*-spacing can be tuned from 1.9 to 3.8 nm, corresponding to a PVP layer thickness ranging from 0.9 to 2.8 nm. The interlayer height is smaller than the polymer’s radius of gyration ($R_g \sim 13$ nm), which emphasizes the strong polymer confinement. As stated in chapter 3.4, the accordance of interlayer height and dimension of the polymer chain also means that the interlayer height can only be changed in defined steps related to the diameter of a PVP chain. Two perfect homogeneous 1D crystalline hybrid Bragg stacks with a *d*-spacing of 2.3 and 3.0 nm, corresponding to a filler content of 40 and 31 vol%, were found (Figure 6A, 6C). The hybrid films impress with a rational series up to the 9th order, low CVs, and sharp and intense reflections. The interlayer height of 1.3 and 2.0 nm can be traced back to a monolayer (Figure 6B) and a bilayer (Figure 6D) of PVP chains, respectively. For filler contents of 23 and 51 vol%, volume ratios do not match and random interstratifications of two interlayer heights are observed, as indicated by increasing CVs and less intense reflections.

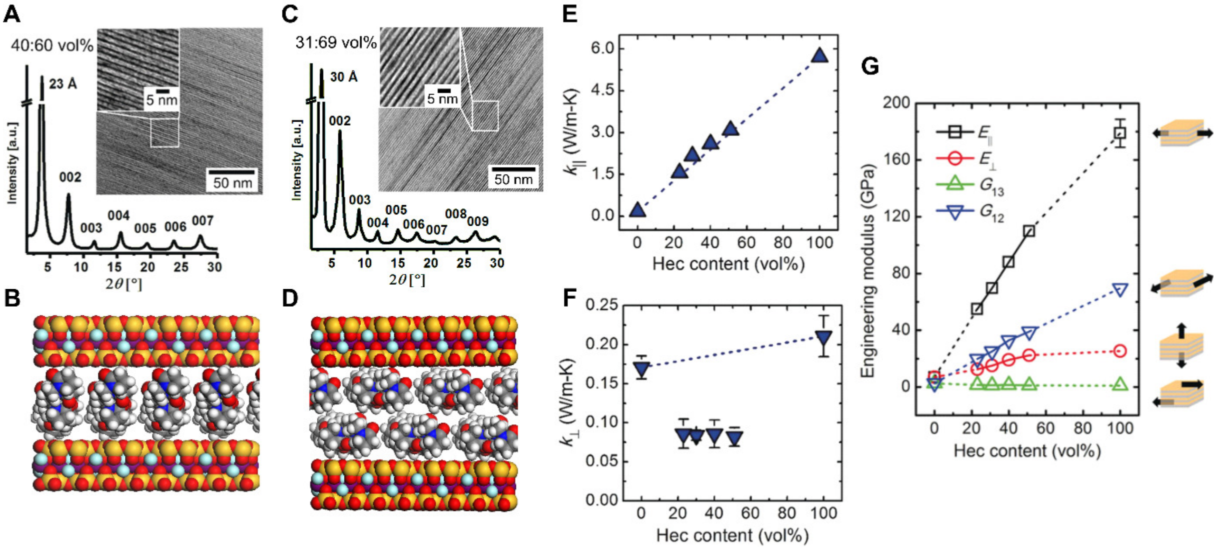

Figure 7: XRD patterns, TEM images and direction-dependent thermoelastic measurements. XRD patterns of the hybrid Bragg stack with a Hec content of A) 40 vol% and C) 31 vol% showing 1D crystallinity as indicated by a rational *00l*-series up to the 7th and 9th order. B) Schematic of the monolayer of PVP, which corresponds to the observed interlayer height of 1.3 nm. D) Schematic of the bilayer of PVP, which corresponds to the observed interlayer height of 2.0 nm E) In-plane and F) Cross-plane thermal conductivity, as a function of the Hec volume content. G) Engineering moduli as function of the Hec volume content. Reprinted with permission from Wang et al.[51] Copyright 2019 The Authors.

The thermal transport in nanocomposites with defined structure on the nanoscale is highly influenced by the increasing amount of interfaces, which lead to the scattering of phonons. Additionally, in hard-soft composites, the acoustic mismatch of the two different materials with varying speed of sounds inhibits the thermal transport. The in-plane thermal conductivity ($k_{\parallel}$) is determined by lock-in thermography and achieves the highest value for the pure Hec film (Figure 6E). The in-plane conductivity of the hybrid Bragg stacks lies in between the limiting values of the pure Hec and pure PVP film and thus follows a simple parallel mixing rule. This is surprising as this implies that the strong polymer confinement has no impact on the in-plane thermal transport. The cross-plane conductivity ($k_{\perp}$) was determined by photoacoustic measurements and deviates from the effective medium behavior, as the hybrid Bragg stacks show a broad minimum at $k_{\perp}$ = 0.09 W/mK (Figure 6F). This deviation is attributed to the tremendous amount of interfaces. As expected for anisotropic nanocomposites, the anisotropy ($k_{\parallel}/k_{\perp}$) is exceptional high and has its highest value of 38 for the hybrid film with the lowest PVP content.

The direction-depended mechanical properties of hybrid Bragg stacks can easily be probed with Brillouin light spectroscopy (BLS). The underlying principle is Brillouin light scattering, the inelastic scattering of the probing single-frequency laser light (photons) on the phonons in the probed material.[87] This allows determining the speed of sound of the material and thus the calculation of the elastic constants, which are connected with the engineering mechanical properties (chapter 3.6). Because of the unique macroscopic orientation, the Hec:PVP system is the first polymer-clay nanocomposite for which the direction-dependent Young's and shear moduli are reported. Comparable to the in-plane thermal conductivity, all engineering mechanical properties obey a simple mixing rule and the values for the hybrid films lie in between the pure Hec and PVP film (Figure 6G). Despite the strong polymer confinement, bulk properties are sufficient to describe the properties of the hybrid Bragg stacks. Furthermore, the Young's moduli and the torsional shear modulus (G_{12}) increase with increasing Hec content, whereas the sliding shear modulus (G_{13}) decreases. Potentially this can be explained with the reduced polymer chain entanglement upon confinement. Moreover, the structural anisotropy results in a mechanical anisotropy ratio of 7, as the Young's moduli ($E_{\parallel}/E_{\perp}$) exhibit large differences in the in-plane and cross-plane direction.

Finally, the results from the thermal and mechanical characterization were correlated. The average phonon mean free path was calculated and ranges in-plane from 0.8 to 1.1 nm for the hybrid Bragg stack films and reaches a maximum of 1.4 nm for the pure Hec film. The lateral size of a Hec nanoplatelet (20 000 nm) by far exceeds the average mean free path of a phonon. Consequently, the in-plane thermal conductivity is influenced by intrinsic material properties and not by grain boundaries. Moreover, $E_{\parallel}$, $E_{\perp}$, and G_{12} directly correlate with the in-plane conductivity. Comparable to the cross-plane thermal conductivity, the mean free path of a phonon for the hybrid Bragg stacks in the cross-plane direction is independent of the composition with a value comparable to the lattice periodicity (~0.1 nm). As confirmed with a series resistance model, the thermal transport in the cross-plane direction is governed by the clay/polymer interface and the strongly reduced interfacial conductance. Changes in the composition and consequently in the interlayer height are insignificant due to the overwhelming contribution of the reduced interfacial conductance. This observation is as well highlighted by the non-existing correlation between thermal and mechanical properties for the cross-plane direction.

4.2 Impact of Ultraconfinement on Composite Barriers

Polymer-clay nanocomposites are appreciated for their ability to improve the barrier performance. The permeability (*P*) of a gas through a barrier coating is given by *P = DS*,[88] with *D* and *S* as diffusivity and solubility, respectively. In nanocomposites, *D* is reduced due to the incorporation of crystalline and impermeable fillers like clay. Like that, the diffusion path (tortuous pathway) of gas molecules is increased. Knowing that it is important to increase the pathway of the gas molecules, it becomes clear that the distribution of clay in the nanocomposite is crucial. According to chapter 3.3, in an exfoliated or delaminated but inhomogeneously distributed nanocomposite, the effect is lower compared to higher filled phase-segregated nanocomposite or hybrid Braggs stacks. Like predicted by Cussler's theory, *D* and consequently *P* nonlinearly depends on the aspect ratio (α) and volume fraction (ϕ) of filler (equation 10).[12]

$$P_{rel} = \frac{P}{P_0} = \left(1 + \mu\left(\frac{\alpha^2\phi^2}{1-\phi}\right)\right)^{-1} \tag{10}$$

With P = permeability of the filled polymer matrix, P_0 = permeability of the neat polymer matrix, ϕ = filler content (volume fraction), α = aspect ratio of the filler, and μ = geometrical factor of the filler depending on its shape.

In highly filled and homogeneously ordered hybrid Braggs stacks, the polymer features strong confinement, which also alters the polymer's properties like segment mobility[33] or glass transition temperature.[37] However, this aspect is not considered by Cussler's theory and was studied within this publication.

The moisture sensitivity of barrier coatings is a known problem and reasoned by the solubility of the permeate within the matrix. Generally, polar molecules are more soluble in polar than in nonpolar matrices and vice versa. At low RH, hydrophilic polymers like PVA or PVP are perfect barrier matrices for hydrophobic permeates like oxygen. However, polar polymers are sensitive to water and swell, which consequently leads to increasing oxygen permeabilities (OP). The reason is that the dissolved water molecules act as softener and increase the segment mobility.[89] Up to now, a systematic study of the relation between permeability and moisture sensitivity is missing. For such a study, a model system is required that differs in filler content but at the same time is identical with respect to aspect ratio, filler type, quality of texture, and 1D crystallinity. Clearly, delaminated or phase-segregated nanocomposites, which are by far the most common types of nanocomposites, cannot serve as such a model system. However, the two hybrid Bragg stacks, comprising Hec and PVP (also see chapter 4.1) are the perfect candidate due to their 1D crystallinity, as verified by XRD patterns and TEM images. At a filler content of 40 and 31 vol%, interlayer heights of 1.3 and 2.0 nm, corresponding to a monolayer and bilayer of PVP, respectively, were realized (Figure 7A-D).

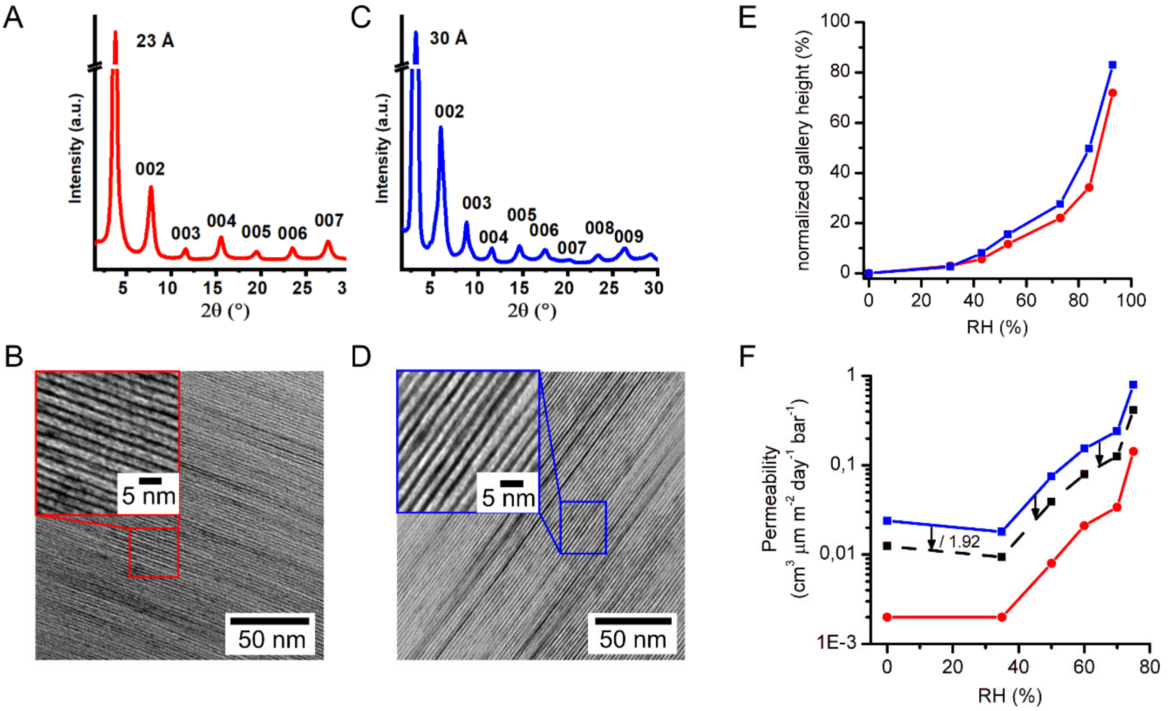

Figure 8: XRD patterns, microscopy images, and study of swelling behavior and oxygen permeability. XRD patterns of the hybrid Bragg stack with a Hec content of A) 40 vol% and C) 31 vol%, displaying intense reflections and a rational series up to the 9th order. TEM images of the hybrid Bragg stacks with a Hec content of B) 40 vol% and D) 31 vol%, confirming the perfect translationally homogeneity. E) Increase of the normalized interlayer height and F) Oxygen permeability of the hybrid Bragg stack with a Hec content of 40 vol% (red) and 31 vol% (blue). Reprinted with permission from Reference 39. Copyright 2020, American Chemical Society.

First, the swelling behavior of both hybrid films is studied by measuring XRD at different RH. Both films swell as indicated by increasing interlayer heights. Hence, the difference between the increase of the normal interlayer height is low for both films and less than 15 %. In total, the water uptake of the less-filled hybrid film (31 vol%) is slightly higher (Figure 7E).

However, it is known that the oxygen transmission rate and the resulting OP is more sensitive to changes in RH and thus the more appropriate method of analysis. With rising RH, the OP first slightly decreases (Figure 7F). This phenomenon is also observed for other polymers[90] or cellulose films.[91] Up to a certain threshold value (< 35% RH), the absorbed water first fills the free volume in the system, which leads to a lower diffusivity. Above this threshold value, the permeability drastically increases. Comparing both hybrid films, the OP of the higher filled hybrid film (40 vol%) is around a factor of 8 lower. Hence, this reduction in OP due to the higher filler content is higher than expected. Based on Cussler's theory, as the aspect ratio (α), the geometrical factor (μ), and the permeability of the neat polymer matrix (P_0) are the same for both hybrid films, the permeability is only expected to be reduced by a factor of 1.92, if the filler content is increased from 31 to 40 vol%. The enhanced offset in permeability cannot be attributed to the effect of the increased filler content. Once again, it has to be considered that in such highly filled hybrid films, the polymer features strong confinement. We therefore attribute this enhanced offset in permeability to the confinement effect. It was recently suggested by Eckert et al.[33] that the confinement reduces the segment mobility. We suggest that the reduced mobility of the chains also reduces the diffusivity of oxygen. In summary, besides the nonlinear dependence of diffusivity on aspect ratio and volume content of filler, also a linear effect of confinement exists.

4.3 One-dimensional crystalline clay nacre-mimetics with record filler contents (73 wt%-91 wt%): From brittle to ductile to brittle

For mimicking nacre, the realization of a homogeneous periodic mechanical decoupling is the key in order to generate materials, which are strong as well as tough. For such a homogeneous decoupling, 1D arrangements of filler platelets and polymer with uniform thickness are required. Platelets with uniform thickness are easily achieved by osmotic swelling, a thermodynamically favored repulsive progress. As stated above, NaHec shows this rare phenomenon and forms nematic liquid crystalline phases, which can easily be mixed with polymer solutions. Nevertheless, another problem needs to be addressed for the synthesis of hybrid Bragg stacks: phase segregation during the drying process. However, phase segregation can be counterbalanced by a sufficient interaction with the clay surface or the interlayer cation. The polymers PVP and PEG are well known for complexing ions and enable the fabrication of homogeneous non-segregated hybrid Bragg stacks. In literature, intercalated phases with a basal spacing of 1.8 and 1.4 nm were described for PEG.[33, 45-46]

Within this work, the PEG volume contents for these two hybrid Bragg stacks were optimized and the defect-free crystallinity of the hybrid Bragg stacks with a basal spacing of 1.77 (Figure 8A) and 1.38 nm for PEG volume contents of 46 and 30 vol%, respectively, was verified by PXRD measurements. The XRD pattern show a rational *00l* series up to the 5th and 4th order with small FWHM and very low CVs of 0.08 and 0.7%.

Additionally, we exploit the ability of the charge homogeneous Hec for the synthesis of ordered interstratifications, consisting of strictly alternating osmotically swelling Na^+ interlayers and NH_4^+ interlayer. Immersed in water, the Na^+ interlayers osmotically swell. This results in double stacks (DS), two hectorite platelets connected by a non-swelling NH_4^+ interlayer. Equally to monolayers of Hec, hybrid Bragg stacks with two different thicknesses of the PEG decoupling layer can be synthesized. Compared to the basal spacing of the hybrid Bragg stacks containing monolayers, the periodicity is increased by the thickness of the NH_4^+ hectorite of 1 nm. The basal spacing is thus 2.79 (Figure 8B) and 2.38 nm for a PEG content of 30 and 18 vol%. The quality of the 1D crystalline order is as well verified in the XRD patterns by rational 00l series up to the 9th and 6th order, low FWHM and low CVs.

The prepared samples allow to systematically study the influence of filler content, thickness of PEG decoupling layer and thickness of Hec platelet on the bulk mechanical properties. Moreover, the platelet diameter was adjusted by ultra sonication from 18000 nm to 340 nm and 406 nm for Hec and DS, respectively.

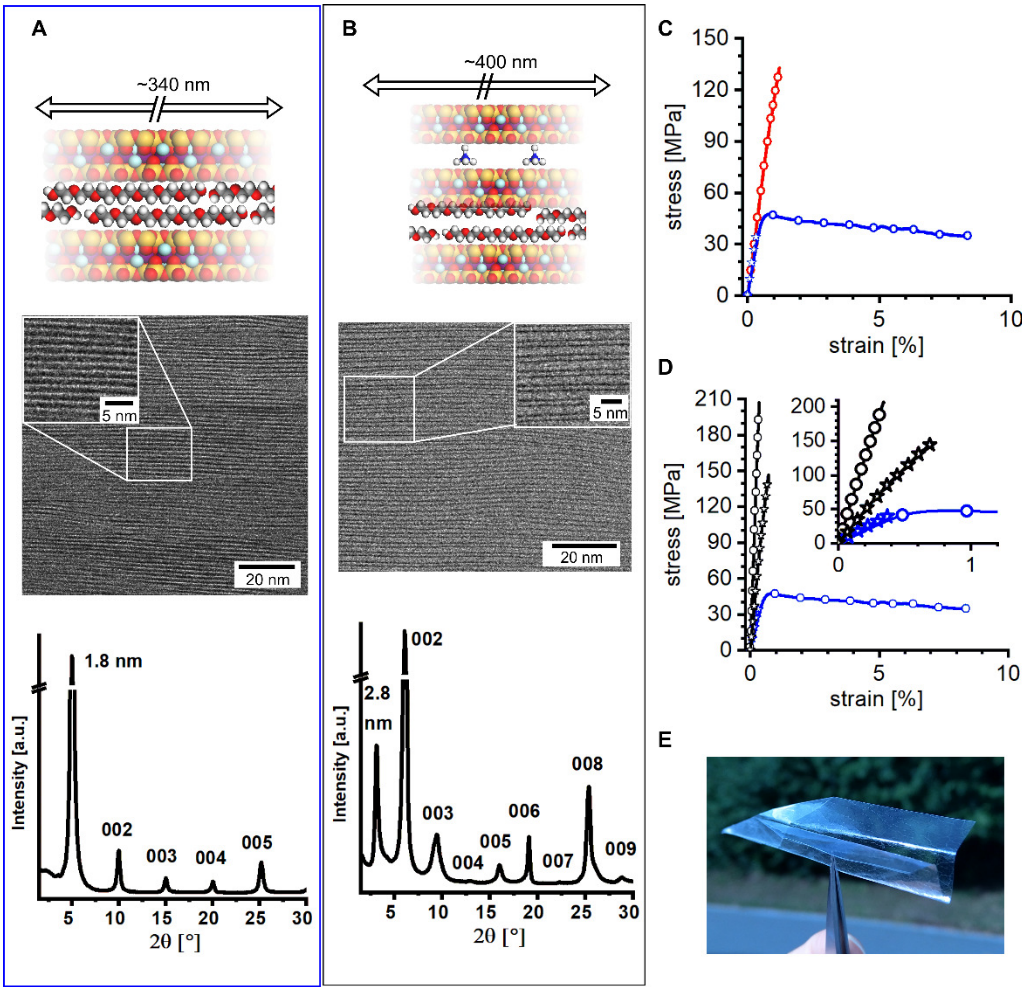

Figure 9: Schematic structure of the hybrid Bragg stacks (top), TEM microscopy images (middle), XRD pattern and stress strain curves. The XRD patterns and TEM images for A) 54 vol% of monolayers of Hec and B) 70 vol% of DS confirm the perfect 1D crystallinity as indicated by intense basal reflections, rational *00l* series and long range periodicity as observed in the TEM images. C) Stress strain curve displaying the influence of filler diameter while keeping the filler content constant (54 vol%): large nanoplatelet diameter (red, circle) vs. small nanoplatelet diameter (blue circle) for 54vol% Hec. D) Stress strain curves illustrating the influence of thickness of filler (Hec - blue vs DS -black) and thickness of decoupling layer (82 vol% DS - black asterisk, 70 vol% DS - black circle, 70 vol% Hec - blue asterisk, 54 vol% Hec - blue circle). E) Transparent and flexible self-supporting films allowing folding without breaking.

First, the impact of the nanoplatelet diameter on the mechanical properties was investigated (Figure 8C), while keeping the filler content constant to 54 vol%. The stress strain curve of the hybrid Bragg stack with large nanoplatelet diameter Hec shows a brittle failure with a maximum strength of 147 MPa and a small elongation of 1.1% (Figure 8C-red circle). However, if the Hec nanoplatelet diameter is reduced from 18000 nm to 340 nm, the mechanical properties completely change, leading to a ductile material with an elongation increased by a factor of 8 (Figure 8C -blue circle). At a yield strength of 48 MPa, plastic deformation is observed, until the sample breaks at an elongation of 8.4%. In contrast to the large Hec nanoplatelets, which appear to be rigidly locked together, the smaller Hec platelets with a diameter of 340 nm allow the sliding of the platelet against each other, which leads to a dissipation of local high stresses. Moreover, the transparent nacre-mimetic can be folded like a paper (Figure 8E).

Obviously, smaller diameters are advantageous for tough nacre-mimetics, why we focused on hybrid Bragg stacks made with the small diameter of Hec and DS.

Further increasing the Hec content to 70 vol% is expected to improve the Young's moduli and possibly also the strength (Figure 8D-blue asterisk). While the Young's modulus increases slightly to 13 GPa, the strength however decreases from 48 MPa to 42 MPa. Apparently, the sliding of the Hec platelets is hindered due to the coordination of the single layer PEG chain in the interlayer to Na^+ interlayer cations.

Moreover, DS are utilized, which are inherently 15% stiffer compared to monolayers of Hec, as determined by a wrinkling technique.[24] Consequently, this should allow to further increase the Young's moduli and possibly strength. Indeed, the Young's moduli increase up to 32 GPa and 26 GPa for a DS content of 70 vol% (Figure 8D-black circle) and 18 vol% (Figure 8D-black asterisk), respectively. However, the fact that the higher filled hybrid Bragg stack shows a lower Young's modulus implies that the mixing rule is not applicable. This counterintuitive trend is also observed for the strength. In addition, comparing the hybrid Bragg stacks with the same thickness of the decoupling PEG interlayer, the ductility of the hybrid Bragg stack containing monolayers of Hec (Figure 8D-blue circle) is completely lost when applying DS (Figure 8D-black circle). The reasons for the catastrophic failure remain unclear. However, the strength (≈ 200 MPa) and stiffness (32 GPa) for the hybrid Bragg stack with DS are interestingly high, as such stiff and strong nacre-mimetics are more likely to be achieved with high Tg polymers[92] in combination with cross-linking[60, 74] or by combining low Tg polymers with a hydrogen bonding network.[77-78]

5 References

1. Nachtigall, W.; Wisser, A., *Bionik in Beispielen*. Springer-Verlag: Berlin Heidelberg, 2013.

2. Wegst, U. G.; Bai, H.; Saiz, E.; Tomsia, A. P.; Ritchie, R. O., Bioinspired structural materials. *Nat. Mater.* **2015,** *14* (1), 23-36.

3. Gao, F., Clay/polymer composites: the story. *Mater. Today* **2004,** *7* (11), 50-55.

4. Ajayan, P. M.; Schadler, L. S.; Braun, P. V., *Nanocomposite Science and Technology*. Wiley-VCH Verlag GmbH & Co. KGaA: Weinheim, 2003.

5. BCC-Research Nanocomposite, Nanoparticles, Nanoclay and Nanotubes: Global Markets to 2022. (accessed 16.10.2020).

6. Stöter, M.; Rosenfeldt, S.; Breu, J., Tunable Exfoliation of Synthetic Clays. *Annu. Rev. Mater. Res.* **2015,** *45* (1), 129-151.

7. Breu, J.; Seidl, W.; Senker, J., Synthese von dreidimensional geordneten Einlagerungsverbindungen des Hectorits. *Z. Anorg. Allg. Chem.* **2004,** *630* (1), 80-90.

8. Möller, M. W.; Handge, U. A.; Kunz, D. A.; Lunkenbein, T.; Altstadt, V.; Breu, J., Tailoring shear-stiff, mica-like nanoplatelets. *ACS Nano* **2010,** *4* (2), 717-24.

9. Bérend, I.; Cases, J. M.; Francois, M.; Michot, L.; Masion, A.; Thomas, F., Mechanism of Adsorption and Desorption of Water Vapor by Homoionic Montmorillonites: 2. The Li^+, Na^+, K^+, Rb^+, and Cs^+-Exchanged Forms. *Clays Clay Miner.* **1995,** *43* (3), 324-336.

10. Krishnamoorti, R.; Vaia, R. A.; Giannelis, E. P., Structure and Dynamics of Polymer-Layered Silicate Nanocomposites. *Chem. Mater.* **1996,** *8* (8), 1728-1734.

11. Lagaly, G., Characterization of clays by organic compounds. *Clay Miner.* **2018,** *16* (1), 1-21.

12. Cussler, E. L.; Hughes, S. E.; Ward, W. J.; Aris, R., Barrier membranes. *J. Membr. Sci.* **1988,** *38* (2), 161-174.

13. Breu, J.; Seidl, W.; Stoll, A. J.; Lange, K. G.; Probst, T. U., Charge Homogeneity in Synthetic Fluorohectorite. *Chem. Mater.* **2001,** *13* (11), 4213-4220.

14. Stöter, M.; Kunz, D. A.; Schmidt, M.; Hirsemann, D.; Kalo, H.; Putz, B.; Senker, J.; Breu, J., Nanoplatelets of sodium hectorite showing aspect ratios of approximately 20,000 and superior purity. *Langmuir* **2013,** *29* (4), 1280-1285.

15. Kalo, H.; Milius, W.; Breu, J., Single crystal structure refinement of one- and two-layer hydrates of sodium fluorohectorite. *RSC Adv.* **2012,** *2* (22), 8452-8459.

16. Rosenfeldt, S.; Stöter, M.; Schlenk, M.; Martin, T.; Albuquerque, R. Q.; Förster, S.; Breu, J., In-Depth Insights into the Key Steps of Delamination of Charged 2D Nanomaterials. *Langmuir* **2016,** *32* (41), 10582-10588.

17. Lerf, A., Storylines in intercalation chemistry. *Dalton Trans.* **2014,** *43* (27), 10276-10291.

18. Wang, L.; Sasaki, T., Titanium oxide nanosheets: graphene analogues with versatile functionalities. *Chem. Rev.* **2014,** *114* (19), 9455-9486.

19. Kunz, D. A.; Erath, J.; Kluge, D.; Thurn, H.; Putz, B.; Fery, A.; Breu, J., In-plane modulus of singular 2:1 clay lamellae applying a simple wrinkling technique. *ACS Appl. Mater. Interfaces* **2013,** *5* (12), 5851-5855.

20. Chiritescu, C.; Cahill, D. G.; Nguyen, N.; Johnson, D.; Bodapati, A.; Keblinski, P.; Zschack, P., Ultralow thermal conductivity in disordered, layered WSe_2 crystals. *Science* **2007,** *315* (5810), 351-353.

21. Möller, M. W.; Hirsemann, D.; Haarmann, F.; Senker, J.; Breu, J., Facile Scalable Synthesis of Rectorites. *Chem. Mater.* **2010,** *22* (1), 186-196.

22. Stöter, M.; Biersack, B.; Rosenfeldt, S.; Leitl, M. J.; Kalo, H.; Schobert, R.; Yersin, H.; Ozin, G. A.; Förster, S.; Breu, J., Encapsulation of functional organic compounds in nanoglass for optically anisotropic coatings. *Angew. Chem. Int. Ed.* **2015,** *54* (16), 4963-7.

23. Stöter, M.; Biersack, B.; Reimer, N.; Herling, M.; Stock, N.; Schobert, R.; Breu, J., Ordered Heterostructures of Two Strictly Alternating Types of Nanoreactors. *Chem. Mater.* **2014,** *26* (18), 5412-5419.

24. Stöter, M.; Gödrich, S.; Feicht, P.; Rosenfeldt, S.; Thurn, H.; Neubauer, J. W.; Seuss, M.; Lindner, P.; Kalo, H.; Möller, M.; Fery, A.; Förster, S.; Papastavrou, G.; Breu, J., Controlled Exfoliation of Layered Silicate Heterostructures into Bilayers and Their Conversion into Giant Janus Platelets. *Angew. Chem. Int. Ed.* **2016,** *55* (26), 7398-7402.

25. Kojima, Y.; Usuki, A.; Kawasumi, M.; Okada, A.; Fukushima, Y.; Kurauchi, T.; Kamigaito, O., Mechanical properties of nylon 6-clay hybrid. *J. Mater. Res.* **1993,** *8* (5), 1185-1189.

26. Usuki, A.; Kojima, Y.; Kawasumi, M.; Okada, A.; Fukushima, Y.; Kurauchi, T.; Kamigaito, O., Synthesis of nylon 6-clay hybrid. *J. Mater. Res.* **1993,** *8* (5), 1179-1184.

27. Kojima, Y.; Usuki, A.; Kawasumi, M.; Okada, A.; Kurauchi, T.; Kamigaito, O., Synthesis of nylon 6–clay hybrid by montmorillonite intercalated with ε-caprolactam. *J. Polym. Sci. A Polym. Chem.* **1993,** *31* (4), 983-986.

28. Yano, K.; Usuki, A.; Okada, A.; Kurauchi, T.; Kamigaito, O., Synthesis and properties of polyimide–clay hybrid. *J. Polym. Sci. A Polym. Chem.* **1993,** *31* (10), 2493-2498.

29. Giannelis, E. P., Polymer Layered Silicate Nanocomposites. *Adv. Mater.* **1996,** *8* (1), 29-35.

30. Messersmith, P. B.; Giannelis, E. P., Synthesis and barrier properties of poly(ε-caprolactone)-layered silicate nanocomposites. *J. Polym. Sci. A Polym. Chem.* **1995,** *33* (7), 1047-1057.

31. Derocher, J.; Gettelfinger, B. T.; Wang, J.; Nuxoll, E. E.; Cussler, E. L., Barrier membranes with different sizes of aligned flakes. *J. Membr. Sci.* **2005,** *254* (1-2), 21-30.

32. Halpin, J. C.; Kardos, J. L., The Halpin-Tsai equations: A review. *Polym. Eng. Sci.* **1976,** *16* (5), 344-352.

33. Eckert, A.; Abbasi, M.; Mang, T.; Saalwächter, K.; Walther, A., Structure, Mechanical Properties, and Dynamics of Polyethylenoxide/Nanoclay Nacre-Mimetic Nanocomposites. *Macromolecules* **2020,** *53* (5), 1716-1725.

34. Zhang, C.; Guo, Y.; Priestley, R. D., Glass Transition Temperature of Polymer Nanoparticles under Soft and Hard Confinement. *Macromolecules* **2011,** *44* (10), 4001-4006.

35. Qin, X.; Xia, W.; Sinko, R.; Keten, S., Tuning Glass Transition in Polymer Nanocomposites with Functionalized Cellulose Nanocrystals through Nanoconfinement. *Nano Lett.* **2015,** *15* (10), 6738-44.

36. Kang, E.; Graczykowski, B.; Jonas, U.; Christie, D.; Gray, L. A. G.; Cangialosi, D.; Priestley, R. D.; Fytas, G., Shell Architecture Strongly Influences the Glass Transition, Surface Mobility, and Elasticity of Polymer Core-Shell Nanoparticles. *Macromolecules* **2019,** *52* (14), 5399-5406.

37. Rolle, K.; Schilling, T.; Westermeier, F.; Das, S.; Breu, J.; Fytas, G., Large Tg Shift in Hybrid Bragg Stacks through Interfacial Slowdown. under revision at ACS Nano, 2020.

38. Johnson, K. J.; Glynos, E.; Maroulas, S.-D.; Narayanan, S.; Sakellariou, G.; Green, P. F., Confinement Effects on Host Chain Dynamics in Polymer Nanocomposite Thin Films. *Macromolecules* **2017,** *50* (18), 7241-7248.

39. Schilling, T.; Habel, C.; Rosenfeldt, S.; Röhrl, M.; Breu, J., Impact of Ultraconfinement on Composite Barriers. *ACS Appl. Polym. Mater.* **2020,** *2* (7), 3010-3015.

40. Doblhofer, E.; Schmid, J.; Riess, M.; Daab, M.; Suntinger, M.; Habel, C.; Bargel, H.; Hugenschmidt, C.; Rosenfeldt, S.; Breu, J.; Scheibel, T., Structural Insights into Water-Based Spider Silk Protein-Nanoclay Composites with Excellent Gas and Water Vapor Barrier Properties. *ACS Appl. Mater. Interfaces* **2016,** *8* (38), 25535-43.

41. Tsurko, E. S.; Feicht, P.; Nehm, F.; Ament, K.; Rosenfeldt, S.; Pietsch, I.; Roschmann, K.; Kalo, H.; Breu, J., Large Scale Self-Assembly of Smectic Nanocomposite Films by Doctor Blading versus Spray Coating: Impact of Crystal Quality on Barrier Properties. *Macromolecules* **2017,** *50* (11), 4344-4350.

42. Tsurko, E. S.; Feicht, P.; Habel, C.; Schilling, T.; Daab, M.; Rosenfeldt, S.; Breu, J., Can high oxygen and water vapor barrier nanocomposite coatings be obtained with a waterborne formulation? *J. Membr. Sci.* **2017,** *540*, 212-218.

43. Verho, T.; Karesoja, M.; Das, P.; Martikainen, L.; Lund, R.; Alegria, A.; Walther, A.; Ikkala, O., Hydration and Dynamic State of Nanoconfined Polymer Layers Govern Toughness in Nacre-mimetic Nanocomposites. *Advanced Materials* **2013,** *25* (36), 5055-5059.

44. Morits, M.; Verho, T.; Sorvari, J.; Liljeström, V.; Kostiainen, M. A.; Gröschel, A. H.; Ikkala, O., Toughness and Fracture Properties in Nacre-Mimetic Clay/Polymer Nanocomposites. *Adv. Funct. Mater.* **2017,** *27* (10).

45. Habel, C.; Maiz, J.; Olmedo-Martínez, J. L.; López, J. V.; Breu, J.; Müller, A. J., Competition between nucleation and confinement in the crystallization of poly(ethylene glycol)/ large aspect ratio hectorite nanocomposites. *Polymer* **2020**, 122734.

46. Wu, J.; Lerner, M. M., Structural, thermal, and electrical characterization of layered nanocomposites derived from sodium-montmorillonite and polyethers. *Chem. Mat.* **1993,** *5* (6), 835-838.

47. Wong, M.; Ishige, R.; White, K. L.; Li, P.; Kim, D.; Krishnamoorti, R.; Gunther, R.; Higuchi, T.; Jinnai, H.; Takahara, A.; Nishimura, R.; Sue, H. J., Large-scale self-assembled zirconium phosphate smectic layers via a simple spray-coating process. *Nat. Commun.* **2014,** *5*, 3589.

48. Moore, D. M.; Reynolds, R. C.; M., D., *X-ray Diffraction and the Identification and Analysis of Clay Minerals*. Oxford University Press: Oxford, U.K., 1997.

49. Ziadeh, M.; Fischer, B.; Schmid, J.; Altstädt, V.; Breu, J., On the importance of specific interface area in clay nanocomposites of PMMA filled with synthetic nano-mica. *Polymer* **2014,** *55* (16), 3770-3781.

50. Wang, Z.; Rolle, K.; Schilling, T.; Hummel, P.; Philipp, A.; Kopera, B. A. F.; Lechner, A. M.; Retsch, M.; Breu, J.; Fytas, G., Tunable Thermoelastic Anisotropy in Hybrid Bragg Stacks with Extreme Polymer Confinement. *Angew. Chem. Int. Ed.* **2020,** *59* (3), 1286-1294.

51. Wang, Z.; Rolle, K.; Schilling, T.; Hummel, P.; Philipp, A.; Kopera, B. A. F.; Lechner, A. M.; Retsch, M.; Breu, J.; Fytas, G., Tunable Thermoelastic Anisotropy in Hybrid Bragg Stacks with Extreme Polymer Confinement. *Angew. Chem. Int. Ed.* **2020,** *59* (3), 1286-1294.

52. Ritchie, R. O., The conflicts between strength and toughness. *Nat. Mater.* **2011,** *10* (11), 817-822.

53. Wang, R. Z.; Suo, Z.; Evans, A. G.; Yao, N.; Aksay, I. A., Deformation mechanisms in nacre. *J. Mater. Res.* **2011,** *16* (09), 2485-2493.

54. Meyers, M. A.; Lin, A. Y.; Chen, P. Y.; Muyco, J., Mechanical strength of abalone nacre: role of the soft organic layer. *J. Mech. Behav. Biomed. Mater.* **2008,** *1* (1), 76-85.

55. Barthelat, F.; Espinosa, H. D., An Experimental Investigation of Deformation and Fracture of Nacre–Mother of Pearl. *Exp. Mech.* **2007,** *47* (3), 311-324.

56. Espinosa, H. D.; Juster, A. L.; Latourte, F. J.; Loh, O. Y.; Gregoire, D.; Zavattieri, P. D., Tablet-level origin of toughening in abalone shells and translation to synthetic composite materials. *Nat. Commun.* **2011,** *2*, 173.

57. Smith, B. L.; Schäffer, T. E.; Viani, M.; Thompson, J. B.; Frederick, N. A.; Kindt, J.; Belcher, A.; Stucky, G. D.; Morse, D. E.; Hansma, P. K., Molecular mechanistic origin of the toughness of natural adhesives, fibres and composites. *Nature* **1999,** *399* (6738), 761-763.

58. Jackson, A. P.; Vincent, J. F. V.; Turner, R. M., The Mechanical Design of Nacre. *Proceedings of the Royal Society B: Biological Sciences* **1988,** *234* (1277), 415-440.

59. Lin, A.; Meyers, M. A., Growth and structure in abalone shell. *Materials Science and Engineering: A* **2005,** *390* (1-2), 27-41.

60. Walther, A.; Bjurhager, I.; Malho, J. M.; Pere, J.; Ruokolainen, J.; Berglund, L. A.; Ikkala, O., Large-area, lightweight and thick biomimetic composites with superior material properties via fast, economic, and green pathways. *Nano Lett.* **2010,** *10* (8), 2742-2748.

61. Cheng, Q.; Wu, M.; Li, M.; Jiang, L.; Tang, Z., Ultratough artificial nacre based on conjugated cross-linked graphene oxide. *Angew. Chem. Int. Ed.* **2013,** *52* (13), 3750-5.

62. Bonderer, L. J.; Studart, A. R.; Gauckler, L. J., Bioinspired design and assembly of platelet reinforced polymer films. *Science* **2008,** *319* (5866), 1069-73.

63. Magrini, T.; Moser, S.; Fellner, M.; Lauria, A.; Bouville, F.; Studart, A. R., Transparent Nacre-like Composites Toughened through Mineral Bridges. *Adv. Funct. Mater.* **2020,** *30* (27).

64. Bouville, F.; Maire, E.; Meille, S.; Van de Moortèle, B.; Stevenson, A. J.; Deville, S., Strong, tough and stiff bioinspired ceramics from brittle constituents. *Nature Mater.* **2014,** *13* (5), 508-14.

65. Tang, Z.; Kotov, N. A.; Magonov, S.; Ozturk, B., Nanostructured artificial nacre. *Nat. Mater.* **2003,** *2* (6), 413-8.

66. Yao, H. B.; Tan, Z. H.; Fang, H. Y.; Yu, S. H., Artificial nacre-like bionanocomposite films from the self-assembly of chitosan-montmorillonite hybrid building blocks. *Angew. Chem. Int. Ed.* **2010,** *49* (52), 10127-31.

67. Li, Y. Q.; Yu, T.; Yang, T. Y.; Zheng, L. X.; Liao, K., Bio-inspired nacre-like composite films based on graphene with superior mechanical, electrical, and biocompatible properties. *Adv Mater* **2012,** *24* (25), 3426-31.

68. Grossman, M.; Pivovarov, D.; Bouville, F.; Dransfeld, C.; Masania, K.; Studart, A. R., Hierarchical Toughening of Nacre-Like Composites. *Adv. Funct. Mater.* **2019,** *29* (9).

69. Gao, H. L.; Chen, S. M.; Mao, L. B.; Song, Z. Q.; Yao, H. B.; Colfen, H.; Luo, X. S.; Zhang, F.; Pan, Z.; Meng, Y. F.; Ni, Y.; Yu, S. H., Mass production of bulk artificial nacre with excellent mechanical properties. *Nat. Commun.* **2017,** *8* (1), 287.

70. Verho, T.; Karppinen, P.; Gröschel, A. H.; Ikkala, O., Imaging Inelastic Fracture Processes in Biomimetic Nanocomposites and Nacre by Laser Speckle for Better Toughness. *Adv. Sci.* **2018,** *5* (1), 1700635.

71. Grossman, M.; Bouville, F.; Erni, F.; Masania, K.; Libanori, R.; Studart, A. R., Mineral Nano-Interconnectivity Stiffens and Toughens Nacre-like Composite Materials. *Adv. Mater.* **2017,** *29* (8).

72. Habel, C.; Schöttle, M.; Daab, M.; Eichstaedt, N. J.; Wagner, D.; Bakhshi, H.; Agarwal, S.; Horn, M. A.; Breu, J., High-Barrier, Biodegradable Food Packaging. *Macromol. Mater. Eng.* **2018,** *303* (10).

73. Jiao, D.; Guo, J.; Eckert, A.; Hoenders, D.; Lossada, F.; Walther, A., Facile and On-Demand Cross-Linking of Nacre-Mimetic Nanocomposites Using Tailor-Made Polymers with Latent Reactivity. *ACS Appl. Mater. Interfaces* **2018,** *10* (24), 20250-20255.

74. Walther, A.; Bjurhager, I.; Malho, J. M.; Ruokolainen, J.; Berglund, L.; Ikkala, O., Supramolecular control of stiffness and strength in lightweight high-performance nacre-mimetic paper with fire-shielding properties. *Angew. Chem. Int. Ed.* **2010,** *49* (36), 6448-6453.

75. Martikainen, L.; Walther, A.; Seitsonen, J.; Berglund, L.; Ikkala, O., Deoxyguanosine phosphate mediated sacrificial bonds promote synergistic mechanical properties in nacre-mimetic nanocomposites. *Biomacromolecules* **2013,** *14* (8), 2531-5.

76. Benitez, A. J.; Lossada, F.; Zhu, B.; Rudolph, T.; Walther, A., Understanding Toughness in Bioinspired Cellulose Nanofibril/Polymer Nanocomposites. *Biomacromolecules* **2016,** *17* (7), 2417-26.

77. Zhu, B.; Jasinski, N.; Benitez, A.; Noack, M.; Park, D.; Goldmann, A. S.; Barner-Kowollik, C.; Walther, A., Hierarchical Nacre Mimetics with Synergistic Mechanical Properties by Control of Molecular Interactions in Self-Healing Polymers. *Angew. Chem. Int. Ed.* **2015,** *54* (30), 8653-7.

78. Eckert, A.; Rudolph, T.; Guo, J.; Mang, T.; Walther, A., Exceptionally Ductile and Tough Biomimetic Artificial Nacre with Gas Barrier Function. *Adv. Mater.* **2018,** *30* (32), e1802477.

79. Xu, Z.-H.; Yang, Y.; Huang, Z.; Li, X., Elastic modulus of biopolymer matrix in nacre measured using coupled atomic force microscopy bending and inverse finite element techniques. *Mater. Sci. Eng. C* **2011,** *31* (8), 1852-1856.

80. Gross, R.; Marx, A., *Festkörperphysik*. De Gruyter, Oldenbourg: 2014; Vol. 2 ed.

81. Rösler, J.; Harders, H.; Baker, M., *Mechanisches Verhalten der Werkstoffe*. Vieweg+Teubner, GWV FAchverlage GmbH , Wiesbaden: 2008; Vol. 3 ed.

82. Popov, V. L.; Heß, M.; Willert, E., Transversely Isotropic Problems. In *Handbook of Contact Mechanics*, Springer: Berlin, Heidelberg, 2019; pp 205-212.

83. Slawinski, M. A., *Waves and Rays in Elastic Continua* World Scientific Publishing Company: 2010; Vol. 3. ed.

84. Cusack, S.; Miller, A., Determination of the elastic constants of collagen by Brillouin light scattering. *J. Mol. Biol.* **1979,** *135* (1), 39-51.

85. Shen, S.; Henry, A.; Tong, J.; Zheng, R.; Chen, G., Polyethylene nanofibres with very high thermal conductivities. *Nat. Nanotechnol.* **2010,** *5* (4), 251-255.

86. Grellmann, W.; Seidler, S., *Kunststoffprüfung*. Carl Hanser Verlag, München: 2011; Vol. 2 ed.

87. Still, T., *High frequency acoustics in colloid-based meso- and nanostructures by spontaneous Brillouin light scattering*. 1 ed.; Springer-Verlag Berlin Heidelberg: 2010.

88. Sabu, T.; Kuruvilla, J.; Malhotra, S. K.; Goda, K.; Sreekala, M. S., *Polymer Composites*. Wiley-VCH: Weinheim, Germany, 2013; Vol. 2.

89. Robertson, G. L., *Food packaging: Principles and Practice*. Taylor & Francis Group: Boca Raton, USA, 2006.

90. Kuraray Relative Humidity. http://www.evalevoh.com/en/eval-properties/barrier-to-oxygen/relative-humidity.aspx (accessed 29.01.2020).

91. Wang, J.; Gardner, D. J.; Stark, N. M.; Bousfield, D. W.; Tajvidi, M.; Cai, Z., Moisture and Oxygen Barrier Properties of Cellulose Nanomaterial-Based Films. *ACS Sustain. Chem. Eng.* **2017,** *6* (1), 49-70.

92. Das, P.; Malho, J. M.; Rahimi, K.; Schacher, F. H.; Wang, B.; Demco, D. E.; Walther, A., Nacre-mimetics with synthetic nanoclays up to ultrahigh aspect ratios. *Nat. Commun.* **2015,** *6*, 5967.

6 Tunable Thermoelastic Anisotropy in Hybrid Bragg Stacks with Extreme Polymer Confinement

Zuyuan Wang, Konrad Rolle,[§] Theresa Schilling,[§] Patrick Hummel,[§] Alexandra Philipp,[§] Bernd A.F. Kopera, Anna M. Lechner, Markus Retsch*, Josef Breu*, George Fytas*

[§] These authors contributed equally to this work

This work was published in *Angew. Chem. Int. Ed.* **2020**, *59*, 1286-1294.

Individual contribution:

Markus Retsch, Josef Breu and George Fytas initialized the idea. I explored and optimized the Hec/PVP system, fabricated the hybrid Bragg stacks, and characterized their structures. Konrad Rolle conducted the BLS experiments. Alexandra Philipp conducted and analyzed the lock-in thermography measurements to obtain the in-plane thermal conductivity. Patrick Hummel performed and analyzed the photoacoustic characterization to obtain the cross-plane thermal conductivity and measured the sample densities. Bernd Kopera conducted additional lock-in thermography measurements and contributed to the lock-in thermography analysis. Anna Lechner conducted and analyzed the DSC measurements to obtain the specific heat. Zuyuan Wang analyzed the BLS data and established the correlation between the mechanical moduli and thermal conductivity.

GDCh Research Articles Angewandte International Edition Chemie

Check for updates

Bragg Stacks

International Edition: DOI: 10.1002/anie.201911546
German Edition: DOI: 10.1002/ange.201911546

Tunable Thermoelastic Anisotropy in Hybrid Bragg Stacks with Extreme Polymer Confinement

Zuyuan Wang, Konrad Rolle[+]*, Theresa Schilling*[+]*, Patrick Hummel*[+]*, Alexandra Philipp*[+]*, Bernd A. F. Kopera, Anna M. Lechner, Markus Retsch,* Josef Breu,* and George Fytas**

Abstract: *Controlling thermomechanical anisotropy is important for emerging heat management applications such as thermal interface and electronic packaging materials. Whereas many studies report on thermal transport in anisotropic nanocomposite materials, a fundamental understanding of the interplay between mechanical and thermal properties is missing, due to the lack of measurements of direction-dependent mechanical properties. In this work, exceptionally coherent and transparent hybrid Bragg stacks made of strictly alternating mica-type nanosheets (synthetic hectorite) and polymer layers (polyvinylpyrrolidone) were fabricated at large scale. Distinct from ordinary nanocomposites, these stacks display long-range periodicity, which is tunable down to angstrom precision. A large thermal transport anisotropy (up to 38) is consequently observed, with the high in-plane thermal conductivity (up to* $5.7\,\mathrm{W\,m^{-1}\,K^{-1}}$*) exhibiting an effective medium behavior. The unique hybrid material combined with advanced characterization techniques allows correlating the full elastic tensors to the direction-dependent thermal conductivities. We, therefore, provide a first analysis on how the direction-dependent Young's and shear moduli influence the flow of heat.*

Introduction

Heat management is crucial in many applications important for fueling the growth of our technology-driven society. It needs to address not only very small length scales to dissipate the heat produced, for example, by electronic circuits, but also very large length scales to realize air conditioning, for instance, for commercial buildings. The ubiquity of heat makes it obvious that heat management is a key technology to realize international long-term goals regarding global warming. Controlling the elusive flow of heat is a complex challenge across multiple materials, length scales, and ultimately devices. This results in stringent requirements for directional control over the heat flux based on advanced material design. Whereas heat transport represents an effective, far-field phenomenon, it is decisively governed by the material structure[1] and chemistry[2] on the microscale. Extreme phenomena of both heat dissipation and thermal insulation have been demonstrated in nanostructured and hybrid materials. For heat dissipation, surprisingly high thermal conductivities have been reported for one-dimensional (1D) fibers comprising synthetic[3] and natural polymers.[4] For thermal insulation, unusually low thermal conductivities have been shown for (disordered) stacks of two-dimensional (2D) materials.[5] Extremely efficient anisotropic thermal insulation materials have been demonstrated with various mixtures of polymers and nanoparticles or 2D materials.[6]

The combination of inherently different materials, such as soft and hard matter, is attractive, as new properties, deviating from those based on the simple linear interpolation, could emerge. This is often accompanied by improved processability, which is aided by the complementary properties of the constituent components. For instance, the soft component can serve as a binder to enable fabrication of large-area, thin films of an otherwise brittle, hard component. On the contrary, the expected effective material properties, such as mechanical reinforcement, optical transparency, and electrical or thermal conductivity, have been often found inferior to the high expectations. The reason for such shortcomings is that the nanocomposite structure, particularly the soft-hard interface, is poorly controlled. Furthermore, although many characterization techniques, such as tensile testing, indentation, and abrasion tests, are capable of assessing engineering properties, they are unsuitable for directly identifying and quantifying anisotropies or microscopic contributions to the effective properties.

---

[*] Z. Wang, K. Rolle,[+] G. Fytas
Max Planck Institute for Polymer Research
Ackermannweg 10, 55128 Mainz (Germany)
E-mail: fytas@mpip-mainz.mpg.de
T. Schilling,[+] P. Hummel,[+] A. Philipp,[+] B. A. F. Kopera, A. M. Lechner, M. Retsch, J. Breu
Bavarian Polymer Institute, University of Bayreuth
Universitätsstraße 30, 95447 Bayreuth (Germany)
and
Department of Chemistry, University of Bayreuth
Universitätsstraße 30, 95447 Bayreuth (Germany)
E-mail: retsch@uni-bayreuth.de
Josef.Breu@uni-bayreuth.de
G. Fytas
Institute of Electronic Structure and Laser, F.O.R.T.H
70013 Heraklion (Greece)

[+] These authors contributed equally to this work.

Supporting information and the ORCID identification number(s) for the author(s) of this article can be found under https://doi.org/10.1002/anie.201911546.

Nevertheless, hybrid systems have been reported to drastically alter the materials' thermal transport properties,[3-6] depending on the geometry, dimensionality, crystallographic symmetry, and confinement. Interestingly, layered structures inherently exhibit structural anisotropy, a feature that can be detrimental or desirable depending on the application.[7] In particular, when polymer films are filled with nanosheets of huge aspect ratio, the resulting nanocomposite properties ought to be exceedingly anisotropic. Yet, only effective material properties such as electrical or thermal conductivity have been reported in a direction-dependent manner. Direction-dependent mechanical properties, which fundamentally translate into thermal transport properties are still missing. Strong anisotropies in hybrid materials are preferentially achieved at small stacking periodicities[5b] or by combining components with a large property contrast.[8]

For a thorough characterization of such nanosheet/polymer stacks (also known as "nacre-mimics"[9]), macroscopically oriented and homogeneous systems are paramount. Such ideal model system should also exhibit translational crystallographic symmetry, tunability, and strong anisotropy. Direction-dependent studies benefit significantly from the availability of various light-scattering methods, rendering a transparent filler such as the synthetic clay hectorite with a mica-type structure desirable. For fundamental investigations of elastic properties, Brillouin light spectroscopy (BLS) has established itself as a technique of choice, as it allows for microscopic observations of high frequency (GHz) dynamics, at which viscoelasticity effects are usually negligible.[10] On the other hand, lock-in thermography and photoacoustic techniques have been proven reliable in accessing the in-plane and cross-plane thermal conductivities of thin films.[11]

Here, we show for the first time the complete mechanical properties of clay/polymer Bragg stacks that are fabricated using a uniquely defined, scalable spray-coating process meeting all aforementioned specifications of a suitable model system. We, therefore, introduce 1D hybrid Bragg stacks based on nacre-mimetic clay/polymer with small stacking periods and large property contrast. These Bragg stacks are scalable in both lateral extension and thickness, and they are macroscopically oriented. The fully controlled microstructure allows a detailed orientation dependent characterization of the thermal and mechanical properties. We couple the thermal and mechanical analyses to achieve an in-depth understanding of the interplay between the thermal conductivities and mechanical moduli in a direction-dependent manner. The extreme confinement of polymer between the clay sheets further prompts a question regarding the validity of continuum mechanics that we also address. The combination of unique hybrid materials and advanced characterization techniques provides an unprecedented insight into the physics of direction-dependent nanomechanical and thermal transport properties in strongly anisotropic materials with polymer confinement.

Results and Discussion

Hybrid Bragg stacks with extreme polymer confinement. The Bragg stacks comprise synthetic clay sodium fluorohectorite (Hec, $[Na_{0.5}]^{inter}[Mg_{2.5}Li_{0.5}]^{oct}[Si_4]^{tet}O_{10}F_2$) and polyvinylpyrrolidone (PVP, $M_w = 40000\,g\,mol^{-1}$). Like layered titanates[12] and antimony phosphates,[13] Hec belongs to a handful of compounds showing a rare phenomenon of osmotic swelling.[14] In contrast to mechanical exfoliation by for example, sonication in the liquid phase,[15] osmotic swelling is a thermodynamically favored, repulsive process,[16] allowing for complete and gentle delamination that preserves the diameter of the parent crystals. In general, exfoliation describes the process of slicing tactoids into thinner stacks, whereas by delamination, the layered material is exfoliated to the level of individual single nanosheets.[17] For Hec, nanosheets with a thickness of 10 Å and a median diameter of 20 μm (Figure S1) are obtained by simply immersing the material into deionized water.[18] Phase purity and a homogeneous charge density guaranteeing a uniform intracrystalline reactivity are prerequisite for such a well-controlled delamination. For Hec this is achieved by long-term annealing, while less uniform natural or other synthetic clays commonly applied for nacre-mimics comprise mixtures of auxiliary minerals, mono-, few- and multilayer stacks.[18]

Because of the large aspect (diameter to thickness) ratio, polar rotation of the nanosheets in suspension is hindered, leading to parallel nanosheets after osmotic swelling. Even dilute (<1 vol.%) suspensions of Hec represent nematic phases.[19] The parallel pre-orientation of adjacent nanosheets in the highly swollen dispersion is indispensable for the fabrication of homogenous and periodic Bragg stacks via spray coating. Similar to titanate nanosheets,[20] Hec nanosheets adopt this cofacial arrangement due to strong electrostatic repulsion with inter-nanosheet distances exceeding 50 nm. Polymers can easily diffuse into these spacious galleries. By mixing Hec suspensions with varying aliquots of an aqueous PVP solution, we obtained perfectly homogeneous, nematic dispersions, as evidenced by small-angle X-ray scattering (SAXS) measurements (Figure S2).

Through spray coating of dilute nematic mixtures of high-aspect-ratio Hec nanosheets with PVP (1–2 wt% total solid content, see Section S1) highly coherent Bragg stack films with tunable gallery spacings are fabricated.[21] The transverse flexibility of clay monolayers[22] and their large aspect ratio are essentials assuring the high degree of precision obtained in the self-assembly.[23] Both, all nanosheets and the macroscopic film are aligned parallel to a polyethylene terephthalate substrate. The microscopic orientation of the Hec nanosheets prescribes the macroscopic film orientation, which is prerequisite for the direction-dependent measurements. The macroscopic film orientation is, consequently, equivalent to the microscopic polymer/clay direction and allows using far-field and integrating characterization techniques to reveal direction-dependent properties. After drying, self-supporting hybrid films with lateral extensions of several square centimeters are peeled off the substrate and used in the BLS and thermal conductivity measurements. Only by generating a nematic phase consisting of a homogeneous mixture of

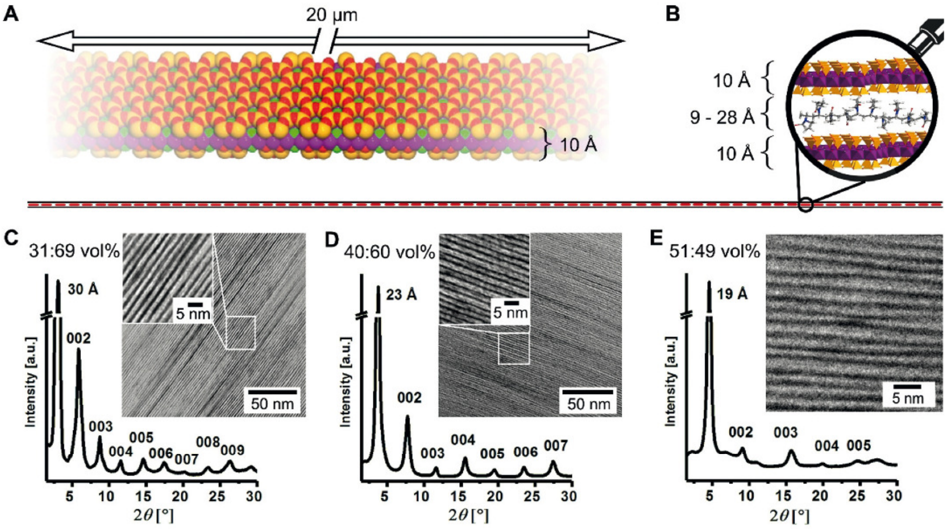

Figure 1. Schematic and microscopic images of ultra-anisotropic and extremely confined Hec/PVP Bragg stacks. A) Space-filling model of one single Hec nanosheet emphasizing the anisotropy of the nanosheet and the corrugation of the clay nanosheet allowing for interdigitation with PVP. B) True to scale schematic of the pronounced structural anisotropy. The ultra-high-aspect-ratio nanosheets stretch from left to right and have lateral dimensions much larger than the length of the PVP polymer chains. The gallery height is on the order of magnitude of the molecular dimensions. C,D) XRD patterns of Hec31/PVP69 and Hec40/PVP60 (defect-free materials) showing intense *001*-reflections and a rational series of basal reflections up to the ninth order. The cross-sectional TEM images show exceptionally periodic homogeneity of these hybrid films over large length scales. E) XRD patterns and cross-sectional TEM image of Hec51/PVP49 displaying a random stacking of two gallery heights.

large aspect ratio and flexible nanosheets allows for fabrication of large area, self-standing 1D single crystals referred to in literature as Bragg stacks or smectic films.[23] Furthermore, appropriate processing like spray coating fostering the thermodynamic equilibration of the hybrid structure during drying has to be employed.

In total, we prepared six samples: pure polymer, pure Hec, and four hybrid Bragg stacks, which are denoted as Hec0/PVP100, Hec100/PVP0, Hec23/PVP77, Hec31/PVP69, Hec40/PVP60, and Hec51/PVP49, respectively. Here, the numbers indicate the volume fractions (vol. %) of Hec and PVP, as confirmed by thermogravimetric analysis (Table S1 and Figure S3).

The Hec surface is corrugated (Figure 1 A) allowing for interdigitation and anchoring of PVP chains. Such interdigitation has been documented for intercalated molecular moieties, where structures based on single crystal data refinement are available.[24] An in-scale impression of the ultra-high aspect ratio provided by the Hec nanosheet gallery is shown in Figure 1 B, where the length of the line corresponds to the typical lateral size of a clay nanosheet, and the thickness of the line to the height of a Hec/PVP/Hec layer. The magnifying lens highlights the extreme polymer confinement in the cross-plane direction. The perfect homogeneous arrangement of Hec nanosheets and PVP is demonstrated by TEM and SEM images over different dimensions (Figure 1 C–E, Figure S7). Note that the lateral dimensions of the Hec nanosheets are much larger than the typical persistence and even contour lengths of the PVP chains. While for the polymer chains the Hec nanosheet confinement appears infinite, at the length scale of the Bragg-stack films extending over tens of centimeters, they are of course finite. At the magnification where single 1 nm thick nanosheets are observable (Figure 1 C–E, Figure S5), the occurrence of nanosheet edges is very rare (fewer than one per 2500 nm^2). Careful inspection, however, reveals few (Figure S6) of these nanosheet edges. The clay nanosheets show in-plane crystalline order resembling the structure of mica. While mica possesses 3D crystalline order, our nanocomposite films belong to the transversely isotropic symmetry class, because the adjacent Hec nanosheets are positioned randomly in the lateral direction. However, all hybrid films show translational crystallographic symmetry along *001* (the cross-plane direction), as indicated by several orders of Bragg reflections (Figure 1 C–E and Figure S5). By varying the PVP content, the basal spacing was tuned in the range from 19 to 38 Å, leading to PVP layer thicknesses ranging from 9 to 28 Å. For all samples, the gallery height is, therefore, significantly smaller than the PVP chains' radius of gyration ($R_{g,PVP} \approx 15$ nm[25]), implying strong polymer confinement.

In contrast to known nanocomposite films,[9b,26] Hec and PVP are thermodynamically miscible over a wide range of compositions. This miscibility is a prerequisite for tuning the basal spacing over a wide range with angstrom precision, which typically is only observed when vapour-phase deposition techniques are applied.[5a] The miscibility is also reflected in an agreement of the basal spacing observed by X-ray diffraction (d_{XRD}) with the nominal values calculated based on the Hec and PVP volume fractions (d_{nominal}, Table S1). To the best of our knowledge, our Hec/PVP Bragg stack films are the first of its kind showing such an agreement. Because the polymer confinement, however, is getting to the point where the gallery height is on the order of the size of an individual polymer chain, it is not possible to vary the gallery height continuously but only in incremental steps that relate to the diameter of the polymer chain. Consequently, only discrete polymer volume fractions lead to essentially defect-free Bragg stacks, as seen in Hec40/PVP60 and Hec31/PVP69. XRD patterns reflect this with a rational *001*-series, where the average basal spacing (d_{XRD}) calculated from individual reflections shows a low coefficient of variation with the reflection peaks being sharp and intense (Table S1). The two gallery heights of the two defect-free hybrid materials (1.3 nm for Hec40/PVP60 and 2.0 nm for Hec31/PVP69) might be attributed to the elliptical nature of PVP chains with principle axes of 1.0 nm and 1.3 nm (Figure S4 A). The observed gallery heights correspond to a monolayer with the longer principal axis (Figure S4 B) oriented perpendicular to the Hec nanosheets and a bilayer with the longer principle axis (Figure S4 C) lying in the plan of the Hec nanosheets, respectively.

In the two cases where the volume ratios do not happen to match (Hec23/PVP77 and Hec51/PVP49), the miscibility is nevertheless assured at small length scale by random interstratification of two gallery heights (Figure 1 E; transmission electron microscopy (TEM) close-up), and the coefficient of variation of the *001*-series increases[27] (Table S1) with the reflection peaks being less intense (Figure 1 E and Figure S5).

In-plane and cross-plane thermal conductivities. The in-plane and cross-plane thermal conductivities of the Hec/PVP hybrid Bragg stacks were characterized by lock-in thermography and photoacoustic measurements,[11,28] respectively. Since the density, ρ, and specific heat, C_p, are prerequisites for the thermal conductivity analysis, they were also determined experimentally by using helium pycnometry and differential scanning calorimetry (DSC) (Section S2), respectively. As the Hec volume fraction increases from 0 to 100 %, the density increases from 1190 to 2730 kg m^{-3} (Figure 2 A). This is well captured by a volume-fraction-based mixing model (dashed line in Figure 2 A). Correspondingly, the specific heat decreases from 1140 to 890 J kg^{-1} K^{-1} (Figure 2 B), which also follows the prediction by an effective medium model (Figure S8 B). Both analyses indicate that despite the extreme polymer confinement the properties of the hybrid stacks could be described by linearly interpolating the properties of the two bulk constituents. The polymer confinement, however, leads to a significant increase in the glass transition temperature (T_g) of PVP, with no discernable T_g below 250 °C even at the lowest Hec composition (Figure S8 A). Expectedly, the thermal conductivity of the Bragg stacks strongly depends on the direction. The in-plane thermal conductivity achieves its maximum, $k_{\parallel,\max} =$ 5.71 W m^{-1} K^{-1}, in Hec100/PVP0, which is even higher than typical in-plane thermal conductivities of natural micas (Figure 4 A).[29] The lower end is given by the isotropic thermal conductivity of Hec0/PVP100, i.e., $k_{\parallel,\min} =$

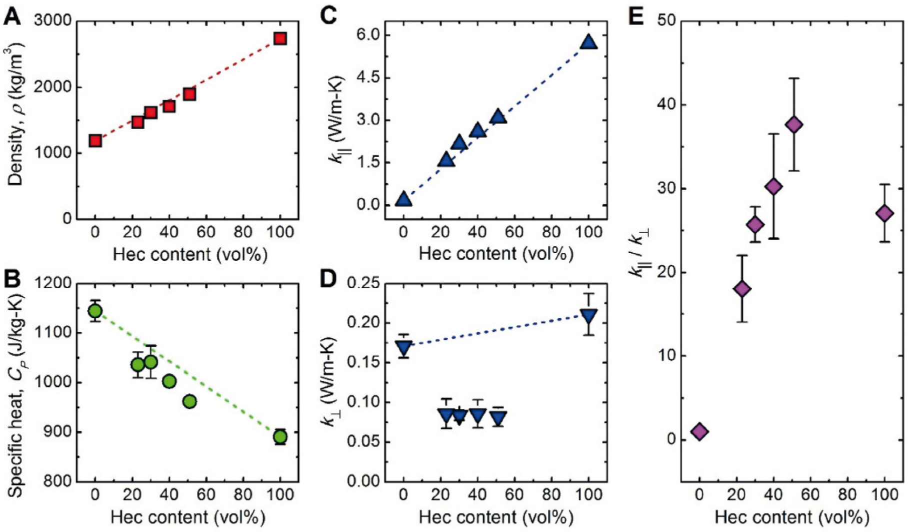

Figure 2. Direction-dependent thermal conductivities of Hec/PVP hybrid Bragg stacks. A) Film density, B) specific heat, and effective C) in-plane and D) cross-plane thermal conductivities, as a function of the Hec volume fraction. The red, green, and blue dashed lines in (A)–(D) show linear trends based on a simple mixing model, $A(x) = (1-x)A(0\%) + xA(100\%)$, where A represents ρ, C_p, $k_\parallel$, or $k_\perp$, and x denotes the Hec volume fraction. E) Ratio of the in-plane to cross-plane thermal conductivities vs. the Hec volume fraction. For clarity, error bars smaller than the symbol size are not shown.

0.17 $W\,m^{-1}\,K^{-1}$ (only determined by photoacoustic characterization). The four hybrid Bragg stacks have in-plane thermal conductivities between these limiting values following a parallel mixing model (Figure 2C).[30] This is again surprising, as it implies that the confinement of PVP has no effect on the in-plane thermal conductivity of the Hec/PVP hybrid stacks compared to bulk PVP. The cross-plane thermal conductivity exhibits a broad minimum at $k_{\perp} \approx 0.09\,W\,m^{-1}\,K^{-1}$, which is comparable to previously reported data for organoclay laminates.[5b] The deviation of the cross-plane thermal conductivities from an effective medium behavior (Figure 2D, dashed line) could be attributed to the Hec/PVP interfaces, which are the dominating contributors to the cross-plane thermal resistance, as discussed below. The thermal conductivity anisotropy, $k_{\parallel}/k_{\perp}$, depends strongly on the hybrid composition, attaining a maximum of 38 in Hec51/PVP49 (Figure 2E). We note that this anisotropy is exceptionally high for electrically insulating hybrid materials[31] and outperforms natural nacre by a factor of ≈20.[32] All in all, the structural perfection of the pure components and hybrid Bragg stacks translate into a record-high in-plane thermal conductivity and thermal transport anisotropy.

Anisotropic mechanical properties. The unique macroscopic orientation in the hybrid Bragg stacks allows us to track down the origin of their high thermal conductivity anisotropy by measuring their full mechanical tensors. The measurements were conducted by using BLS, which probes the phonon wave vector, **q**, dependent sound velocity, v, through inelastic light scattering by thermally excited, high frequency (GHz) phonons.[10] Since the hybrid Bragg stacks are transversely isotropic, only **q** vectors in a single plane containing the symmetry axis have to be considered. For such a **q** vector, the direction can be denoted by α, the angle between **q** and the normal to the sample film, and because of symmetry α can be restricted in the range from 0° to 90°. The measurements corresponding to $\alpha = 0°$, $0° < \alpha < 90°$, and $\alpha = 90°$ were conducted in the reflection, backscattering, and transmission scattering geometries, respectively, while the polarization of the phonon mode was selected using different incident and scattered light polarization configurations (e.g., VV for quasi-longitudinal (Q-L) and quasi-transverse (Q-T) modes, and VH for a pure-transverse (P-T) mode).[33] This flexibility of accessible parameters makes BLS particularly suitable for characterizing anisotropic or crystalline structures, as demonstrated in previous experiments on mica crystals.[34] Since this work is the first one to apply the BLS technique to a hybrid Bragg stack material, we briefly outline the BLS measurement and data analysis.

Consider Hec31/PVP69 as an example. A typical BLS spectrum from the reflection geometry (inset to Figure S14A) displays a cross-plane longitudinal ($L_{\perp}$) mode in the VV polarization configuration (Figure S14B). A typical BLS spectrum from the backscattering geometry (Figure 3A, top-right inset) depicts a Q-L and a Q-T mode in the VV polarization configuration (Figure 2A) and a weak P-T mode in the VH polarization configuration (Figure 3A, top-left inset). Comparatively richer information exists in a typical BLS spectrum from the transmission geometry (Figure 3B, top-right inset). In the VV polarization configuration, the BLS spectrum features an in-plane longitudinal ($L_{\parallel}$) and a Q-L mode at a small laser incident angle, β, and an additional Q-T mode at a large β (Figure 3B). In the VH polarization configuration, a weak P-T mode at all β (Figure 3B, top-left inset) is clearly resolved. In the transmission BLS spectra, the intensity ratio of the Q-L and Q-T peaks yields additional information (Figure S15B) and the Q-T mode intensity increases noticeably at higher Hec contents. By comparing the backscattering and transmission spectra, it becomes clear that the appearance of the Q-L and Q-T peaks in the latter (Figure 3B) results from the scattering of the laser beam internally reflected on the sample's backside.[35]

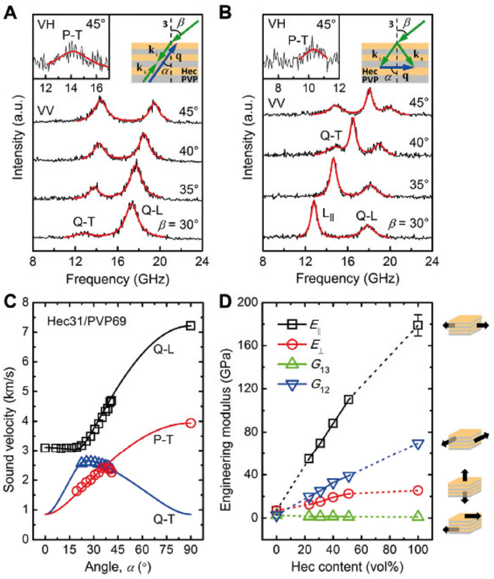

Figure 3. BLS measurements and strong mechanical anisotropy of Hec/PVP hybrid Bragg stacks. A,B) Polarized BLS spectra (anti-Stokes side) of the Hec31/PVP69 hybrid stack film recorded in (A) the backscattering geometry with **q** forming a variable angle, α, with the normal to the sample film (top-right inset to (A)) and (B) the transmission geometry with the phonon wave vector, **q**, directed in-plane ($\alpha = 90°$; top-right inset to (B)). $\mathbf{k}_i$ and $\mathbf{k}_s$ are the wave vectors of the incident and scattered light beams, respectively. β is the incident angle of the laser beam. The quasi-longitudinal (Q-L), quasi-transverse (Q-T), and in-plane longitudinal ($L_{\parallel}$) phonon modes are indicated in (A) and (B). The much weaker depolarized VH spectra of the pure transverse modes are shown in the top-left insets. Notice the correspondence between the Q-L and Q-T modes in (A) and those in (B). C) Direction-dependent sound velocities of the observed acoustic phonons in the BLS spectra of Hec31/PVP69. The three solid lines indicate theoretical representations (Equations (S6)–(S8)) of the experimental sound velocities of the three modes. D) Composition dependence of four engineering moduli. The moduli of the anisotropic hybrid films are extrapolated to those of the pure PVP and pure Hec films, as shown by the dashed lines. The four schematics beside (D) visualize the physical meanings of the corresponding moduli.

Based on the frequency shift, f, from the BLS spectrum and the phonon wave vector, **q**, from the momentum conservation analysis, we calculated the sound velocity along a certain **q** as $v = 2\pi f / |\mathbf{q}|$. Whereas the reflection measurements give the $v_{\text{Q-L}}$ at $\alpha = 0°$ and the transmission measurements result in the $v_{\text{Q-L}}$ and $v_{\text{P-T}}$ at $\alpha = 90°$, the backscattering measurements provide sound velocities for all the Q-L, Q-T, and P-T modes at intermediate α angles, as limited by the sample's refractive index. These direction-dependent sound velocities are reported in Figure 3C for Hec31/PVP69; additional data for the other samples are shown in Figure S16A–D. Since sound velocities are intimately related to the elastic stiffness tensor in the framework of the Christoffel equation,[36] the availability of the former together with the measured sample densities (Figure 2A and Table S4) enables unique determination of the latter. For a transversely isotropic material, the elastic stiffness tensor contains five independent elastic constants (e.g., C_{11}, C_{12}, C_{13}, C_{33}, and C_{44}).[37] Through χ^2 fitting,[38] we obtained the elastic stiffness constants (Figure S16E and Table S4), which allow theoretical representation of the direction-dependent sound velocities (solid lines in Figure 3C and Figure S16A–D) as well as determination of the engineering mechanical properties (Figure 3D and Table S5). In addition, we analyzed the error bars (standard deviations) of the quantities according to principles of uncertainty propagation (Section S5).

This analysis provides the first direction-dependent insights into the mechanical properties of hybrid Bragg stacks in general and of clay/polymer nanocomposites in particular. The Young's moduli, $E_{\parallel}$ and $E_{\perp}$, and torsional shear modulus, G_{12}, all increase with increasing Hec volume fraction. The sliding shear modulus, G_{13}, however, decreases from 2.6 GPa in Hec0/PVP100 to 1.0 GPa in Hec100/PVP0. A reduction in polymer chain entanglement upon confinement could be the cause of the decrease in G_{13}.[39] Since the elastic moduli of polymer nanocomposites depend on the specific filler-polymer and polymer-polymer interactions, a rationalization of the increase ($E_{\parallel}$, $E_{\perp}$, G_{12}) or decrease (for G_{13}) with Hec content would require computer simulations.[39] All the mechanical moduli of the Bragg stacks display an effective medium behavior, assuming values between those of the two bulk components. We point out that even though the PVP chains are strongly confined between the adjacent Hec nanosheets (note $R_{\text{g,PVP}} > 5(d_{\text{XRD}} - d_{\text{Hec}})$), bulk properties (e.g., ρ_{PVP}, ρ_{Hec}) are sufficient to fully capture the BLS measurements. As expected from the structural anisotropy, the Young's moduli exhibit large differences between the in-plane and cross-plane directions (Figure 3D). As the Hec volume fraction increases from 0 to 100%, the mechanical anisotropy ratio, $E_{\parallel}/E_{\perp}$, increases from 1 to 7. Concomitantly, the two characteristic Poisson's ratios, ν_{31} and ν_{12}, vary in ranges of 0.02–0.05 (nearly zero or cork-like values) and 0.34–0.41 (typical polymer values), respectively (Table S5). The reasonable values of the mechanical properties corroborate the validity of continuum mechanics at length scales of a few nanometers and in the presence of extreme polymer confinement.

In the last section, we summarize the new insights onto the anisotropic thermoelasticity that can be gained from this wholistic analysis. We firstly exploit the directly measured direction-dependent sound velocities, and secondly correlate the derived mechanical moduli to the direction-dependent thermal conductivities. We first apply a kinetic theory model, $k = C_V \bar{v}_g \bar{\Lambda}/3$ to estimate the average phonon mean free path $\bar{\Lambda}$ along different directions in the Bragg stacks.[40] We use $C_V = C_P$ and $\bar{v}_g = \bar{v}_{s\parallel} = (v_{\text{Q-L},\parallel} + v_{\text{Q-T},\parallel} + v_{\text{P-T},\parallel})/3$; a similar analysis is done for $k_{\perp}$. The in-plane $\bar{\Lambda}$ strongly depends on the hybrid composition, ranging from 14 Å for Hec100/PVP0 to 2 Å for Hec0/PVP100 (Figure 4A). We note that these $\bar{\Lambda}$ values significantly underestimate the presence of longer ranged phonons, which are typically better described by a phonon mean free path accumulation function.[40,41] It is well known that thermal transport involves phonons over a wide range of frequencies which have different specific heat capacities, group velocities, and mean free paths. The underestimated $\bar{\Lambda}$ in our analysis could be attributed to the overestimated $\bar{v}_g$ from the BLS measurements, which mainly characterizes the propagation speed of a small fraction of the low frequency (long wavelength) phonons. These low frequency phonons carry only a negligible fraction of the overall heat. For the in-plane direction, the lateral size of the Hec nanosheets by far exceeds the average phonon mean free path. Hence, the high in-plane thermal conductivities are governed by the intrinsic material properties, not by the presence of grain boundaries between the aligned Hec nanosheets. The complementary analysis for $k_{\perp}$ demonstrates a strong reduction of $\bar{\Lambda}$ down to less than 1 Å (Figure 4B) with no discernible composition dependence along the cross-plane direction. Interfacial effects apparently dominate the thermal transport in this direction, which is better analyzed using a series resistance model (SRM, Figure 4C,F) as outlined by Losego et al.[5b] The fitted value of the interfacial conductance, $G_{\text{Hec/PVP}} = 89 \pm 8\ \text{MW}\,\text{m}^{-2}\,\text{K}^{-1}$ (see Section S4), falls well into the range of reported values for other inorganic/organic interfaces.[2a,42] The intercalation of PVP between the clay sheets leads to a strong reduction of the interfacial conductance, which is $G_{\text{Hec/Hec}} = 219 \pm 28\ \text{MW}\,\text{m}^{-2}\,\text{K}^{-1}$ for the pure hectorite.

We next address the correlation between the anisotropic mechanical moduli and thermal conductivities. Two distinct conclusions can be drawn. (i) In the direction parallel to the Hec nanosheets, a correlation between the thermal conductivity and all mechanical moduli is found. Along this direction the phonon mean free path is considerably shorter than the typical lateral size of a Hec nanosheet, rendering grain boundary effects insignificant. The influence of $E_{\parallel}$, $E_{\perp}$, and G_{12} on the thermal transport dominates over G_{13} since the former moduli show a direct relation to the in-plane thermal conductivity. $E_{\parallel}$ and G_{12} show a power scaling law close to one (0.93) between in-plane thermal conductivity and modulus ($E_{\perp}$ scales with 0.38). Whereas we find a clear correlation between the moduli and the thermal conductivity, we cannot deduce which change in mechanical modulus causes which effect to the thermal transport. The applicability of a simple mixing model along the parallel direction as outlined in Figure 2A–C is certainly surprising in view of the strong polymer confinement effect on the glass transition (Figure S8). (ii) In the direction perpendicular to the Hec nanosheets, the phonon mean free path is comparable to the periodicity of the Bragg stacks. Here, the composition

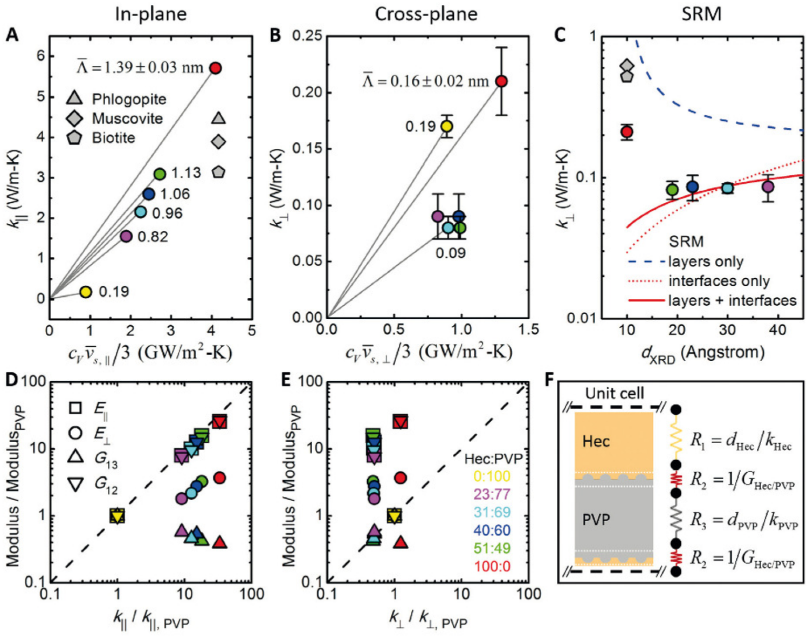

Figure 4. Analysis of anisotropic thermomechanical coupling in Hec/PVP hybrid Bragg stacks. A) Effective in-plane thermal conductivity, $k_{|}$, vs. $C_V\bar{v}_{s,\|}/3$. The yellow, purple, cyan, blue, green, and red colored symbols represent the Hec0/PVP100, Hec23/PVP77, Hec31/PVP69, Hec40/PVP60, Hec51/PVP49, and Hec100/PVP0 samples, respectively. The phlogopite data point is from our additional measurements; muscovite and biotite data points are from reference.[29] B) Effective cross-plane thermal conductivity, $k_{\perp}$, vs. $C_V\bar{v}_{s,\perp}/3$. In (A) and (B), the numbers beside the data points indicate the average phonon mean free paths, $\bar{\Lambda}$ (i.e., the slope of the gray lines). C) Effective cross-plane thermal conductivity, $k_{\perp}$, vs. the basal spacing of the Bragg stacks. The red solid line is a fit to the experimental data based on the series resistance model (SRM) shown in (F). As a comparison, the blue dashed line considers only the thermal resistances of the Hec and PVP layers, and the red dotted line considers only the thermal resistances of the Hec/PVP interfaces. D) Normalized mechanical moduli vs. normalized effective in-plane thermal conductivity, $k_{|}$. The dashed line shows a direct correlation between the two axes with a power of one. E) Normalized mechanical moduli vs. normalized effective cross-plane thermal conductivity, k . In (D) and (E), the following values of the pure PVP film, $E - E_{|} - 7.0$ GPa, $G_{13} - G_{12} - 2.6$ GPa, and $k_{|} - k - 0.17$ W m^{-1} K^{-1}, are used as references in the normalization. F) A schematic of the SRM used to analyze the Hec/PVP interfacial thermal conductance.

dependence of the mechanical properties does not influence the reduction of the cross-plane thermal conductivity (vertical spread of the data points in Figure 4E). Thus, changes to the gallery height are insignificant, which indicates the overwhelming contribution of the interfacial conductance. Considering changes to the pure components we find that reducing the sliding shear modulus G_{13} decreases the cross-plane thermal transport properties of the polymer component. The reduction in $k_{\perp}$ of the hybrid stacks relative to pure hectorite correlates to losses in $E_{|}$, $E_{\perp}$, and G_{12} that apparently counteract the increase in G_{13}. Overall, the mechanical and thermal properties are uncorrelated along the perpendicular direction, and the thermal transport is governed by the Hec/PVP interfaces.

Conclusion

In conclusion, fully delaminated hectorite platelets can be processed into hybrid Bragg stacks with unique properties, with the polymer polyvinylpyrrolidone being the intercalated second component. Such long-range 1D ordered materials become accessible by simply spray coating the desired nematic dispersions of adjusted volume fractions, which at the same time controls the periodicity of the hybrid stacks down to the angstrom level. The macroscopic lattice alignment enables the determination of direction-dependent thermoelastic properties, which we assessed by thermal transport characterization techniques and Brillouin light spectroscopy. We found a record-high anisotropy between the in-plane and cross-plane thermal conductivities in clay/polymer hybrid materials. This is corroborated by the first report of direction-dependent Young's and shear moduli that are also strongly anisotropic. The effective gallery spacing, density, specific heat, and in-plane thermal conductivity were found to conform to composition-dependent simple mixing models. Despite the nanometer-level lattice periodicity and angstrom-level polymer confinement, the Christoffel-equation-based model, derived in the framework of continuum mechanics, remains applicable for determining the anisotropic elasticity. Of general relevance is the direction dependency of the way that the mechanical moduli and thermal conductivities correlate. In the in-plane direction, where grain boundaries are negligible relative to the phonon mean free path, $E_{\parallel}$, $E_{\perp}$, and G_{12} directly correlate with the in-plane thermal conductivity. In the cross-plane direction, where the phonon mean free path is comparable to the lattice periodicity, the thermal transport is governed by the clay/polymer interfaces. We are convinced that a wholistic understanding of direction-dependent thermoelastic properties will have a broad impact on important applications such as electronic packaging and thermoelectrics. This contribution is only a first step towards this goal. More work needs to be done for the deterministic—maybe even independent—design of mechanical and thermal properties. Future studies should also address the role of enthalpic interaction at the clay/polymer interface, interdigitation of the confined polymer, size effects of the platelets, and other nanosheet materials.

Acknowledgements

We thank Sabine Rosenfeldt for conducting SAXS measurements on the gel samples. We also thank Marco Schwarzmann for preparing TEM samples and taking TEM images. The Volkswagen Foundation funded this project through a Lichtenberg professorship. DFG RE 3550/2-1 provided additional support. Z.W., K.R., and G.F. acknowledge the financial support by ERC AdG SmartPhon (Grant No. 694977).

Conflict of interest

The authors declare no conflict of interest.

Keywords: anisotropy · Brillouin light scattering · mechanical properties · organic–inorganic hybrid composites · thermal conductivity

How to cite: *Angew. Chem. Int. Ed.* **2020**, *59*, 1286–1294
Angew. Chem. **2020**, *132*, 1302–1310

---

[1] a) B. Graczykowski, A. El Sachat, J. S. Reparaz, M. Sledzinska, M. R. Wagner, E. Chavez-Angel, Y. Wu, S. Volz, Y. Wu, F. Alzina, C. M. Sotomayor Torres, *Nat. Commun.* **2017**, *8*, 415; b) M. E. Siemens, Q. Li, R. Yang, K. A. Nelson, E. H. Anderson, M. M. Murnane, H. C. Kapteyn, *Nat. Mater.* **2010**, *9*, 26–30; c) J. A. Tomko, A. Pena-Francesch, H. Jung, M. Tyagi, B. D. Allen, M. C. Demirel, P. E. Hopkins, *Nat. Nanotechnol.* **2018**, *13*, 959–964.

[2] a) M. D. Losego, M. E. Grady, N. R. Sottos, D. G. Cahill, P. V. Braun, *Nat. Mater.* **2012**, *11*, 502–506; b) G. H. Kim, D. Lee, A. Shanker, L. Shao, M. S. Kwon, D. Gidley, J. Kim, K. P. Pipe, *Nat. Mater.* **2015**, *14*, 295–300.

[3] S. Shen, A. Henry, J. Tong, R. Zheng, G. Chen, *Nat. Nanotechnol.* **2010**, *5*, 251–255.

[4] a) X. Huang, G. Liu, X. Wang, *Adv. Mater.* **2012**, *24*, 1482–1486; b) R. Fuente, A. Mendioroz, A. Salazar, *Mater. Lett.* **2014**, *114*, 1–3.

[5] a) C. Chiritescu, D. G. Cahill, N. Nguyen, D. Johnson, A. Bodapati, P. Keblinski, P. Zschack, *Science* **2007**, *315*, 351–353; b) M. D. Losego, I. P. Blitz, R. A. Vaia, D. G. Cahill, P. V. Braun, *Nano Lett.* **2013**, *13*, 2215–2219.

[6] a) B. Wicklein, A. Kocjan, G. Salazar-Alvarez, F. Carosio, G. Camino, M. Antonietti, L. Bergström, *Nat. Nanotechnol.* **2015**, *10*, 277–283; b) T. Li, J. Song, X. Zhao, Z. Yang, G. Pastel, S. Xu, C. Jia, J. Dai, C. Chen, A. Gong, F. Jiang, Y. Yao, T. Fan, B. Yang, L. Wagberg, R. Yang, L. Hu, *Sci. Adv.* **2018**, *4*, eaar3724; c) M. Chau, B. A. F. Kopera, V. R. Machado, S. M. Tehrani, M. A. Winnik, E. Kumacheva, M. Retsch, *Mater. Horiz.* **2017**, *4*, 236–241.

[7] X. Tian, M. E. Itkis, E. B. Bekyarova, R. C. Haddon, *Sci. Rep.* **2013**, *3*, 1710–1715.

[8] N. Song, D. Jiao, S. Cui, X. Hou, P. Ding, L. Shi, *ACS Appl. Mater. Interfaces* **2017**, *9*, 2924–2932.

[9] a) A. Eckert, T. Rudolph, J. Guo, T. Mang, A. Walther, *Adv. Mater.* **2018**, *30*, 1802477; b) T. Verho, M. Karesoja, P. Das, L. Martikainen, R. Lund, A. Alegría, A. Walther, O. Ikkala, *Adv. Mater.* **2013**, *25*, 5055–5059; c) T. Szabó, M. Szekeres, I. Dékány, C. Jackers, S. De Feyter, C. T. Johnston, R. A. Schoonheydt, *J. Phys. Chem. C* **2007**, *111*, 12730–12740; d) Z. Tang, N. A. Kotov, B. Magonov, B. Ozturk, *Nat. Mater.* **2003**, *2*, 413–418.

[10] a) T. Still, *High frequency acoustics in colloid-based meso- and nanostructures by spontaneous Brillouin light scattering*, 1st ed., Springer, Berlin, Heidelberg, **2010**; b) E. Alonso-Redondo, M. Schmitt, Z. Urbach, C. M. Hui, R. Sainidou, P. Rembert, K. Matyjaszewski, M. R. Bockstaller, G. Fytas, *Nat. Commun.* **2015**, *6*, 8309.

[11] a) V. Singh, T. L. Bougher, A. Weathers, Y. Cai, K. Bi, M. T. Pettes, S. A. McMenamin, W. Lv, D. P. Resler, T. R. Gattuso, D. H. Altman, K. H. Sandhage, L. Shi, A. Henry, B. A. Cola, *Nat. Nanotechnol.* **2014**, *9*, 384–390; b) A. Mendioroz, R. Fuente-Dacal, E. Apinaniz, A. Salazar, *Rev. Sci. Instrum.* **2009**, *80*, 074904.

[12] L. Wang, T. Sasaki, *Chem. Rev.* **2014**, *114*, 9455–9486.

[13] P. Davidson, C. Penisson, D. Constantin, J.-C. P. Gabriel, *Proc. Natl. Acad. Sci. USA* **2018**, *115*, 6662–6667.

[14] A. Lerf, *Dalton Trans.* **2014**, *43*, 10276–10291.

[15] V. Nicolosi, M. Chhowalla, M. G. Kanatzidis, M. S. Strano, J. N. Coleman, *Science* **2013**, *340*, 1226419.

[16] M. Daab, N. J. Eichstaedt, A. Edenharter, S. Rosenfeldt, J. Breu, *RSC Adv.* **2018**, *8*, 28797–28803.

[17] J. E. F. C. Gardolinski, G. Lagaly, *Clay Miner.* **2005**, *40*, 547–556.

[18] M. Stöter, D. A. Kunz, M. Schmidt, D. Hirsemann, H. Kalo, B. Putz, J. Senker, J. Breu, *Langmuir* **2013**, *29*, 1280–1285.

[19] S. Rosenfeldt, M. Stöter, M. Schlenk, T. Martin, R. Q. Albuquerque, S. Förster, J. Breu, *Langmuir* **2016**, *32*, 10582–10588.

[20] K. Sano, Y. S. Kim, Y. Ishida, Y. Ebina, T. Sasaki, T. Hikima, T. Aida, *Nat. Commun.* **2016**, *7*, 12559.

[21] H. Kalo, W. Milius, J. Breu, *RSC Adv.* **2012**, *2*, 8452–8459.

[22] D. A. Kunz, J. Erath, D. Kluge, H. Thurn, B. Putz, A. Fery, J. Breu, *ACS Appl. Mater. Interfaces* **2013**, *5*, 5851–5855.

[23] M. Wong, R. Ishige, K. L. White, P. Li, D. Kim, R. Krishnamoorti, R. Gunther, T. Higuchi, H. Jinnai, A. Takahara, R. Nishimura, H. J. Sue, *Nat. Commun.* **2014**, *5*, 3589.

[24] a) W. Seidl, J. Breu, *Z. Kristallogr. - Cryst. Mater.* **2005**, *220*, 169–176; b) A. Baumgartner, K. Sattler, J. Thun, J. Breu, *Angew. Chem. Int. Ed.* **2008**, *47*, 1640–1644; *Angew. Chem.* **2008**, *120*, 1664–1668.

[25] N. L. McFarlane, N. J. Wagner, E. W. Kaler, M. L. Lynch, *Langmuir* **2010**, *26*, 13823–13830.

[26] E. S. Tsurko, P. Feicht, F. Nehm, K. Ament, S. Rosenfeldt, I. Pietsch, K. Roschmann, H. Kalo, J. Breu, *Macromolecules* **2017**, *50*, 4344 – 4350.
[27] D. M. Moore, R. C. Reynolds, Jr., *X-ray Diffraction and the Identification and Analysis of Clay Minerals*, Oxford University Press, Oxford, **1997**.
[28] A. Philipp, N. W. Pech-May, B. A. F. Kopera, A. M. Lechner, S. Rosenfeldt, M. Retsch, *Anal. Chem.* **2019**, *91*, 8476 – 8483.
[29] C. Clauser, E. Huenges, in *Rock Physics & Phase Relations: A Handbook of Physical Constants* (Ed.: T. J. Ahrens), American Geophysical Union, Washington DC, **2013**, pp. 105 – 126.
[30] J. K. Carson, S. J. Lovatt, D. J. Tanner, A. C. Cleland, *Int. J. Heat Mass Transfer* **2005**, *48*, 2150 – 2158.
[31] Y.-F. Huang, Z.-G. Wang, H.-M. Yin, J.-Z. Xu, Y. Chen, J. Lei, L. Zhu, F. Gong, Z.-M. Li, *ACS Appl. Nano Mater.* **2018**, *1*, 3312 – 3320.
[32] L. P. Tremblay, M. B. Johnson, U. Werner-Zwanziger, M. A. White, *J. Mater. Res.* **2011**, *26*, 1216 – 1224.
[33] R. W. Gammon, Brillouin scattering experiments in the ferroelectric crystal triglycine sulfate, PhD thesis, John Hopkins University, **1967**.
[34] L. E. McNeil, M. Grimsditch, *J. Phys. Condens. Matter* **1993**, *5*, 1681.
[35] J. Krüger, L. Peetz, M. Pietralla, *Polymer* **1978**, *19*, 1397 – 1404.
[36] a) S. P. Cheadle, R. J. Brown, D. C. Lawton, *Geophysics* **1991**, *56*, 1603 – 1613; b) M. Mah, D. R. Schmitt, *Geophysics* **2001**, *66*, 1217 – 1225.
[37] a) S. Cusack, A. Miller, *J. Mol. Biol.* **1979**, *135*, 39 – 51; b) Y. C. Chu, S. I. Rokhlin, *J. Acoust. Soc. Am.* **1994**, *96*, 342 – 352.
[38] M. Zgonik, P. Bernasconi, M. Duelli, R. Schlesser, P. Günter, M. H. Garrett, D. Rytz, Y. Zhu, X. Wu, *Phys. Rev. B* **1994**, *50*, 5941 – 5949.
[39] J. Midya, Y. Cang, S. A. Egorov, K. Matyjaszewski, M. R. Bockstaller, A. Nikoubashman, G. Fytas, *Nano Lett.* **2019**, *19*, 2715 – 2722.
[40] G. A. Elbaz, W. L. Ong, E. A. Doud, P. Kim, D. W. Paley, X. Roy, J. A. Malen, *Nano Lett.* **2017**, *17*, 5734 – 5739.
[41] A. S. Henry, G. Chen, *J. Comput. Theor. Nanosci.* **2008**, *5*, 141 – 152.
[42] W. L. Ong, S. M. Rupich, D. V. Talapin, A. J. McGaughey, J. A. Malen, *Nat. Mater.* **2013**, *12*, 410 – 415.

Manuscript received: September 9, 2019
Accepted manuscript online: November 12, 2019
Version of record online: December 4, 2019

Angewandte Chemie
Eine Zeitschrift der Gesellschaft Deutscher Chemiker

Supporting Information

Tunable Thermoelastic Anisotropy in Hybrid Bragg Stacks with Extreme Polymer Confinement

Zuyuan Wang, Konrad Rolle[+], Theresa Schilling[+], Patrick Hummel[+], Alexandra Philipp[+], Bernd A. F. Kopera, Anna M. Lechner, Markus Retsch, Josef Breu,* and George Fytas**

anie_201911546_sm_miscellaneous_information.pdf

Abstract: Controlling thermomechanical anisotropy is important for emerging heat management applications such as thermal interface and electronic packaging materials. Whereas many studies report on thermal transport in anisotropic nanocomposite materials, a fundamental understanding of the interplay between mechanical and thermal properties is missing, due to the lack of measurements of direction-dependent mechanical properties. In this work, exceptionally coherent and transparent hybrid Bragg stacks made of strictly alternating mica-type nanosheets (synthetic hectorite) and polymer layers (polyvinylpyrrolidone) were fabricated at large scale. Distinct from ordinary nanocomposites, these stacks display long-range periodicity, which is tunable down to angstrom precision. A large thermal transport anisotropy (up to 38) is consequently observed, with the high in-plane thermal conductivity (up to 5.7 W m^{-1} K^{-1}) exhibiting an effective medium behavior. The unique hybrid material combined with advanced characterization techniques allows correlating the full elastic tensors to the direction-dependent thermal conductivities. We, therefore, provide a first analysis on how the direction-dependent Young's and shear moduli influence the flow of heat.

DOI: 10.1002/anie.201911546

Table of Contents

Section S0. Summary of Experimental Section

Sample preparation. The synthetic clay sodium fluorohectorite (Hec, $[Na_{0.5}]^{inter}[Mg_{2.5}Li_{0.5}]^{oct}[Si_4]^{tet}O_{10}F_2$) was delaminated by immersing it into Millipore water (0.5 wt%). The aqueous PVP solution (1 wt%) was added in the desired weight ratio. The suspension was mixed for at least one day in an overhead shaker. The homogeneity of the suspension was crosschecked by SAXS measurements. Self-supporting films were prepared using a fully automatic spray coating system. Every spraying cycle is followed by a drying cycle of 90 s at a temperature of 55 °C. We prepared pure PVP, pure Hec, and four hybrid Hec/PVP films. The self-supporting films were characterized by thermogravimetric analysis, XRD, and TEM. Additional information about the sample preparation can be found in Section S1.

In-plane thermal conductivity measurements. Lock-in thermography measures the temperature spreading across the free-standing samples upon thermal excitation by a focused laser beam with a modulated intensity. To prevent convective heat losses, the experiments are conducted in a vacuum chamber. The amplitude and phase data are extracted from the radial temperature distribution. The thermal diffusivity is then fitted by the slope method for thermally thin films. With the density, determined by helium pycnometry, and the specific heat, determined by differential scanning calorimetry (DSC), the thermal conductivity can be calculated. More details are provided in Section S2.

Cross-plane thermal conductivity measurements. The photoacoustic method uses a modulated laser beam to periodically heat a transducer layer in intimate contact with the sample. The heat is converted into an acoustic wave propagating into a gas tight cell above the sample, which is filled with helium at 20 psi. A sensitive microphone detects the phase shift between the acoustic signal and the modulated laser by a lock-in amplifier. The frequency-dependent phase shift is then compared to a multilayer model, assuming one-dimensional heat transfer. Therefrom, the total layer resistance is obtained. With the film thickness determined by AFM, the effective thermal conductivity is calculated. More details are provided in Section S2.

Brillouin light spectroscopy (BLS). BLS measures the phonon dispersion, $\omega(\mathbf{q})$, by detecting the Doppler frequency shift, ω, of the inelastically scattered light by sound waves ("phonons") with a wave vector, $\mathbf{q}$. We recorded BLS spectra utilizing three scattering geometries (transmission, reflection, and backscattering) and two polarization configurations of the incident (λ = 532 nm) and scattered light (polarized VV, depolarized VH), which allowed us to establish the nature of the observed phonons. We varied the incident angle to obtain the direction-dependent sound velocities necessary for the determination of the anisotropic elasticity. The elastic stiffness tensors were obtained from the representation of the direction-dependent sound velocities by the Christoffel equation assuming transverse isotropy. The characteristic Young's moduli, shear moduli, and Poisson's ratios of the Bragg stacks were subsequently calculated. More details can be found in Section S3.

Section S1. Sample preparation

Materials

The synthetic clay sodium fluorohectorite (Hec, $[Na_{0.5}]^{inter}[Mg_{2.5}Li_{0.5}]^{oct}[Si_4]^{tet}O_{10}F_2$) was synthesized via melt synthesis followed by long-term annealing, according to an established procedure. The material featured a cation exchange capacity of 1.27 mmol g^{-1} (References[1]). Polyvinylpyrrolidone (PVP; M_w = 40.000 g mol^{-1}) was provided by Sigma Aldrich.

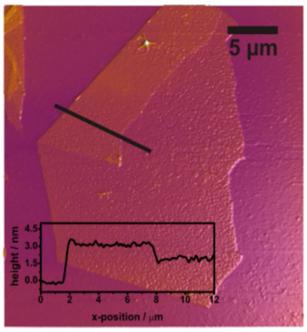

Figure S1. Atomic force microscopy image of a single delaminated Hec nanosheet. Reprinted with permission from Langmuir .[1b] Copyright 2019 American Chemical Society.

Film preparation

For the delamination, the synthetic Hec was immersed into Millipore water (0.5 wt%). The complete delamination was studied by small angle X-ray scattering (SAXS).[2] The aqueous PVP solution (1 wt%) was added in the desired weight ratio. The suspension was mixed for at least 1 day in the overhead shaker. Homogeneity of the suspensions was cross-checked by SAXS measurements. All SAXS data were measured using the small-angle X-ray system "Double Ganesha AIR" (SAXSLAB, Denmark). The X-ray source of this laboratory-based system is a rotating anode (copper, MicroMax 007HF, Rigaku Corporation, Japan) providing a micro-focused beam. The data were recorded by a position sensitive detector (PILATUS 300 K, Dectris). To cover the range of scattering vectors between 0.004-1.0 Å^{-1}, different detector positions were used. The measurements of the suspensions were done in 1 mm glass capillaries (Hilgenberg, code 4007610, Germany) at room temperature. To improve the detection limit of the in-house machine, the suspensions were first concentrated to ≈ 10 wt% by centrifugation at 10000 rpm for 1 hour. A rational basal series was found for all suspensions, indicating that all clay nanosheets were separated to exactly the same distance by water and PVP (Figure S2). Within experimental errors reaggregation to stacks of Hec can be excluded by the absence of a reflection typical for crystalline hydrated Hec phases at q = 0.65-0.41 Å^{-1}.

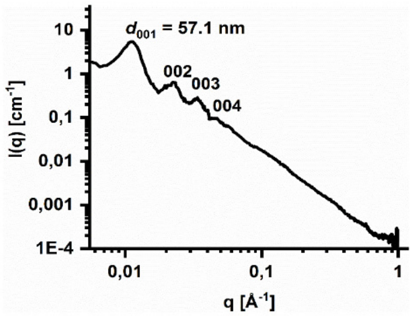

Figure S2. 1D SAXS pattern of the concentrated gel sample Hec40/PVP60.

The self-supporting films were prepared by spray coating. The fully automatic spray coating system was equipped with a SATA 4000 LAB HVLP 1.0 mm spray gun (SATA GmbH & Co. KG, Germany). Suspensions were sprayed on a corona-treated polyethylene terephthalate (PET) foil (optimont 501, bleher Folientechnik, Germany). The spraying and nozzle pressure were set constant at values of 2 and 4 bar, respectively. The round per flat fan control was set to 6 with a flow speed of 3 mL s^{-1}. The distance between the spraying gun and the substrate was 17 cm. The thickness of the suspension layer applied in one spraying step is ≈ 2 µm which corresponds to ≈ 20 nm dry nanocomposite film thickness. For drying the suspension layer, the sample is stopped under infrared lamps until evaporation of the solvent is complete. After every spraying cycle, a drying cycle of 90 s with a temperature of 55 °C took place. The spraying/drying cycle is repeated until the desired barrier film thickness of 50 µm is obtained. Afterwards, the film was dried at 100 °C for 3 days and peeled off from the PET foil to achieve self-supporting films. For characterization by photoacoustic analysis thinner films on the order of a few µm were spray coated onto clean 1 mm thick microscopy glass slides.

In total, we prepared six samples, which are denoted as Hec0/PVP100, Hec23/PVP77, Hec31/PVP69, Hec40/PVP60, Hec51/PVP49, and Hec100/PVP0, respectively (Table S1). Throughout the manuscript, all samples are referred to by the nominal volume fractions (vol%) of Hec and PVP, respectively. To rule out compositional changes during spray coating, these ratios were cross-checked (Table S1) by thermogravimetric analysis (TGA), using a Linseis STA PT 1600 (Linseis Messgeräte GmbH, Germany). Changes in mass observed upon heating in synthetic air up to 800 °C were attributed to the combustion of PVP.

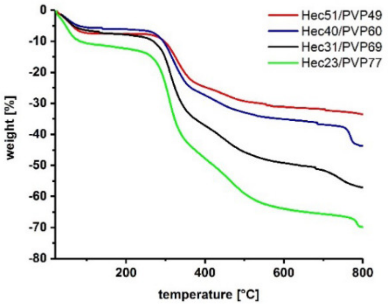

Figure S3. TGA curves of four hybrid Bragg stacks. The weight loss below 200 °C corresponds to the water.

X-ray diffraction (XRD) patterns for the films were recorded in Bragg-Brentano-geometry on an Empyrean diffractometer (PANalytical B.V.; the Netherlands) using Cu K_{α} radiation (λ = 1.54187 Å). The self-supporting films were placed on glass slides (Menzel-Gläser; Thermo Scientific). Prior to the XRD measurements, the samples were dried at 100 °C in a vacuum chamber for one week.

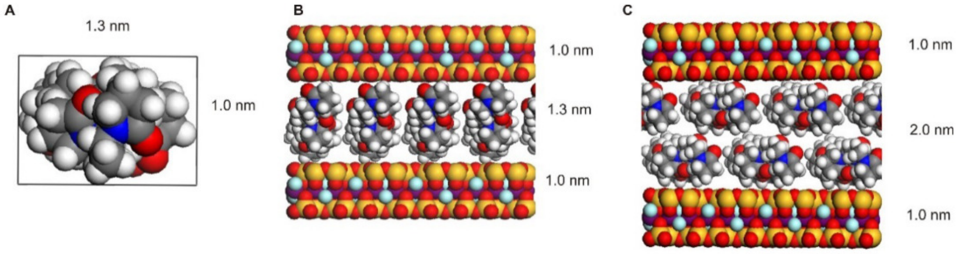

Figure S4. Space filling models. (A) PVP viewed along the polymer backbone chain. (B) Monolayer of PVP oriented with the longer principal axis perpendicular to the Hec nanosheet. (C) Bilayer of PVP lying in the plane of the Hec nanosheets.

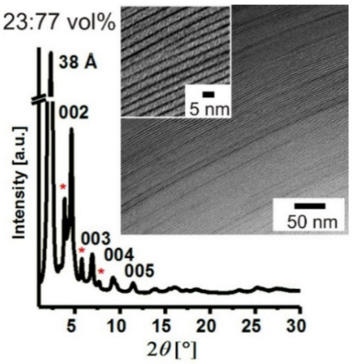

Figure S5. XRD pattern and TEM image of the nanocomposite film Hec23/PVP77. The red asterisks denote a second series of basal reflections of a minority phase (*d* = 2.3 nm).

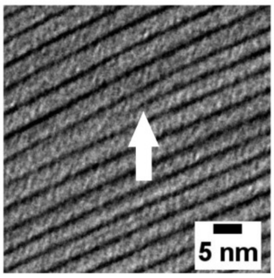

Figure S6. Lattice plane termination of a single Hec nanosheet.

As a measure of the quality of the one-dimensional crystallinity of the films, the coefficient of variation (CV) and the full width at half maximum (FWHM) were determined (Table S1). Large CV-values (≈ 3% [3]) and large FWHM indicate non-rationality of the diffraction pattern as caused by a random interstratification of different interlayer heights.

Assuming PVP and Hec densities of 1.2 g cm^{-3} and 2.7 g cm^{-3}, respectively, nominal *d*-spacings can be calculated for the various volume ratios ($d_{nominal}$ in Table S1).[4] They agree reasonably with those obtained from XRD measurements (d_{XRD} in Table S1). In analyzing the cross-plane thermal conductivity using the series resistance model, we used the d_{XRD} values.

Table S1. Overview of the structural and chemical characterization.

	nominal Hec:PVP ratio [wt%]	nominal Hec:PVP ratio [vol%]	PVP content [a] [wt%]	PVP content [b] [vol%]	d_{nominal} [Å]	d_{XRD} [Å]	gallery height (PVP) [c] [nm]	CV [%]	FWHM [°2θ]
Hec100/PVP0	100:0	100:0	-	-	10	10	-	-	-
Hec51/PVP49	70:30	51:49	27	45	18	19	0.9	5.9	0.4
Hec40/PVP60	60:40	40:60	38	58	23	23	1.3	1.3	0.3
Hec31/PVP69	50:50	31:69	49	68	30	30	2.0	1.0	0.3
Hec23/PVP77	40:60	23:77	59	76	41	38	2.8	2.8	0.3
Hec0/PVP100	0:100	0:100	100	100	-	-	-	-	-

[a] determined by TGA; [b] calculated with the PVP content determined by TGA; [c] gallery height corresponds to the *d*-spacing minus the Hec platelet height of 1 nm.

Scanning electron microscopy (SEM) images were taken with a Zeiss LEO 1530 (Carl Zeiss AG, Germany) at an operating voltage of 3 kV. Cross sections were prepared by cutting with a razor blade. The samples with Hec were sputtered with 10 nm carbon.

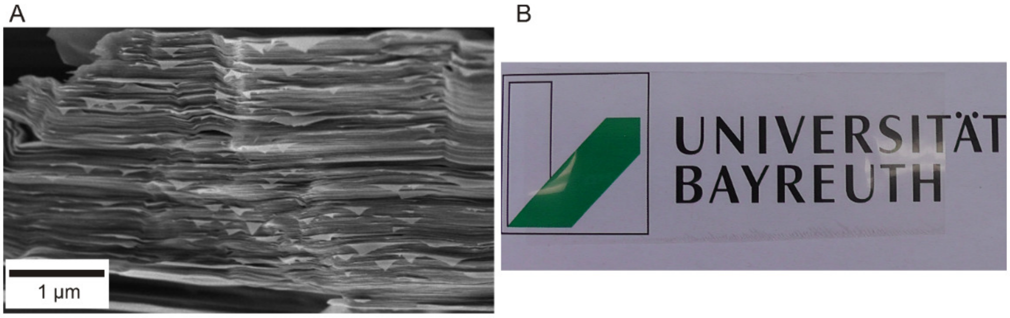

Figure S7. SEM image and photograph of the hybrid film. A) The SEM image displays the ordered arrangement of hectorite sheets at the macro-scale. B) As the hectorite platelets arrange highly ordered, light scattering is prevented and the films is transparent.

Transmission electron microscopy (TEM) images were taken on a JEOL JEM-2200FS (JEOL GmbH, Germany) at an acceleration voltage of 200 kV. Cross-section pictures of the self-supporting films were prepared with a Cryo Ion Slicer IB-09060CIS (JEOL, Germany).

Section S2. Thermal measurements

For the determination of the in-plane and cross-plane thermal conductivity, the density and the specific heat are needed. Therefore, Helium pycnometry and differential scanning calorimetry (DSC) were used. We determined the in-plane thermal diffusivity by lock-in thermography, and the cross-plane thermal conductivity by the photoacoustic method. Prior to the measurements, the samples were dried at 100 °C in a vacuum chamber for one week.

Helium pycnometry

The density of the samples was measured by helium pycnometry. Therefore, an Ultrapyc 1200e (Quantachrome Instruments) was used. Prior to each measurement the volume of the empty measurement cell was measured. Afterwards, small pieces of the free-standing films were weighed into the sample cell with a nominal volume of 1.8 cm^3. One hundred runs were performed to determine the volume of the films at room temperature. By knowing the mass (measured on a fine balance) and the volume, the density of the samples was calculated.

Differential scanning calorimetry

The specific heat was determined by DSC measurements according to the ASTM E1269 standard. The samples were freeze ground for better processability and contact to the DSC pans. The measurements were performed on a TA instruments Discovery DSC 2500. An isothermal step (1h, 100 °C) was conducted prior to the measurement to ensure dry conditions. Then two heating cycles were used and only the second cycle evaluated. The temperature profile ranged from -40 to 250 °C using a heating rate of 20 K min^{-1} with a nitrogen flow of 50 mL min^{-1}.

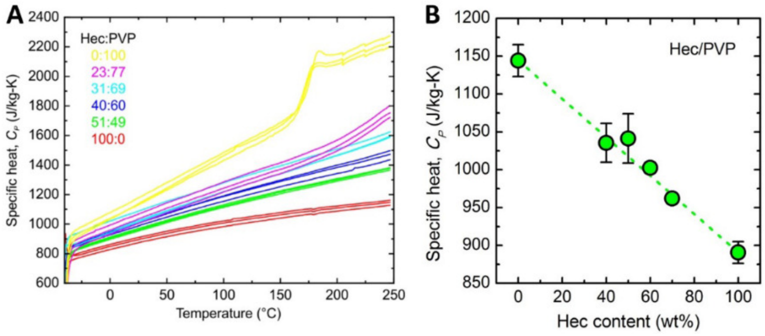

Figure S8. Temperature and composition dependencies of the specific heat. (A) Three samples per Hec/PVP composition were measured. The average specific heat at 25 °C was used to calculate the thermal conductivity. (B) The green dashed line shows the prediction by a simple mixing model, $C_P(x) = (1\text{-}x)C_P(0\%) + xC_P(100\%)$, with x being the hectorite weight fraction.

Lock-in thermography

The in-plane thermal diffusivity of free-standing Hec/PVP stack films was obtained by lock-in thermography (LIT). The self-built LIT set-up is shown in Figure S9.

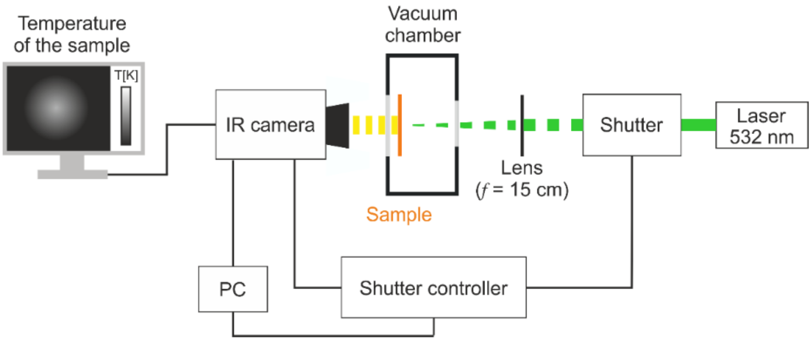

Figure S9. Scheme of the lock-in thermography set-up. The samples were measured in a vacuum chamber to avoid convective heat losses to the environment.

The sample is heated by a laser beam (Genesis MX 532-1000 SLM OPS, Coherent, λ = 532 nm) focused onto the sample surface by a lens of 150 mm focal length. The intensity of the laser is modulated using a shutter (SH05/M, Thorlabs) controlled by a shutter controller (SC10, Thorlabs). The emitted infrared (IR) radiation of the sample surface is detected by an Infratec VarioCAM HD research IR camera (spectral window: 7.5-14 µm). The camera is equipped with a close-up lense. In this configuration, the minimum spatial resolution is 29 µm (working distance: 33 mm). Since heat losses to the environment lead to an overestimation of the thermal diffusivity[5] all samples were measured under vacuum conditions (~3x10^{-3} mbar). Furthermore, all samples were coated with a 20 nm carbon layer for enhanced laser absorption. The coating of the sample was facing to the IR camera. LIT measurements were performed using Infratec's IRBISactiveonline software. Measurements were conducted at several lock-in frequencies between 0.219 and 1.765 Hz (depending on the Hec/PVP composition). Furthermore, each measurement was averaged over several (600-2000) lock-in periods to enhance the signal to noise ratio, with the first 60-100 periods being discarded. The software calculates automatically the amplitude and phase of the temperature oscillations (Figure S10). The red point marks the midpoint of the laser excitation and thus the midpoint of the radial distribution.

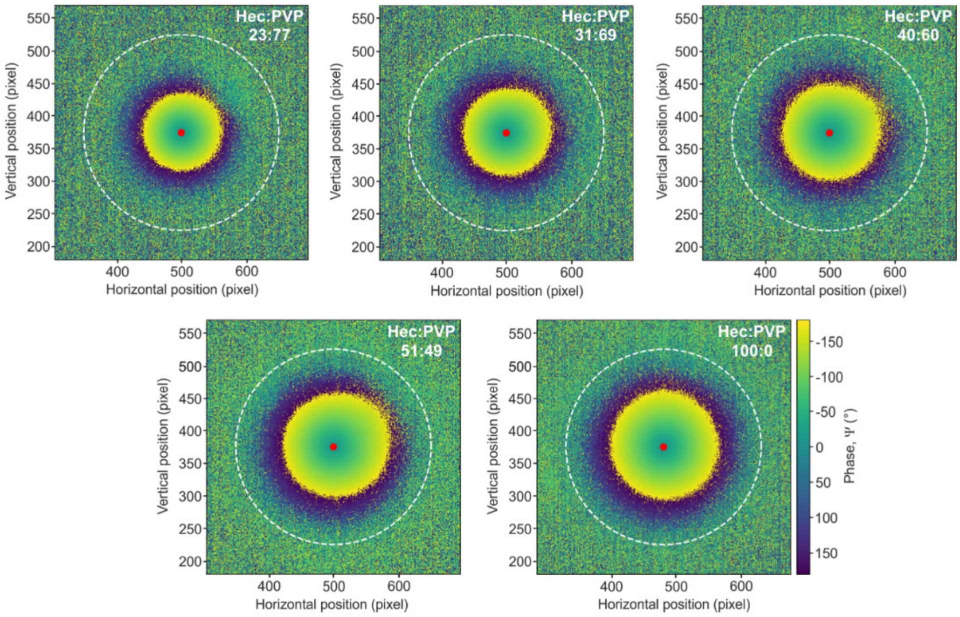

Figure S10. Exemplary two-dimensional phase images measured at a frequency of 1.111 Hz. The penetration depth of the temperature oscillations increases with increasing thermal diffusivity of the Hec/PVP films. The focal point of the laser is marked by a red point in the center of the IR image.

A self-written Python script is used to extract radial profiles for the phase and amplitdue images (Figure S11). The thermal diffusivity is calculated from the phase and amplitude slopes according to the slope method of a thermally thin film[5b]:

$$m_{\Psi} \cdot m_{\ln(T\cdot r^{0.5})} = \frac{\pi f_{\text{lock-in}}}{\alpha_{\parallel}} \quad . \qquad \text{(S1)}$$

Here, m_{Ψ} is the slope of the linear relation of the phase and the radial distance r, $m_{\ln(T\cdot r^{0.5})}$ is the slope of the linear relation of the natural logarithm of the amplitude T multiplied by the square root of the radial distance r, $f_{\text{lock-in}}$ is the lock-in frequency, and $\alpha_{\parallel}$ is the in-plane thermal diffusivity.

Three films have been measured for each Hec/PVP composition. An average in-plane thermal diffusivity and a standard deviation were calculated for each composition, as summarized in Table S2.

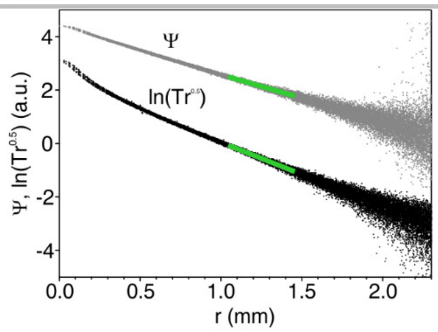

Figure S11. Exemplary phase Ψ and amplitude profiles. The green line indicates the region, where the linear fit was evaluated. This is sufficiently far away from the central excitation spot.

Table S2. In-plane thermal diffusivity values of Hec/PVP stack films. Three films per Hec/PVP composition were measured, based on which an average in-plane thermal diffusivity and a standard deviation were calculated.

Sample	**In-plane thermal diffusivity (mm^2 s^{-1})**
Hec23/PVP77	1.02 ± 0.04
Hec31/PVP69	1.28 ± 0.02
Hec40/PVP60	1.52 ± 0.04
Hec51/PVP49	1.69 ± 0.03
Hec100/PVP0	2.35 ± 0.03

The in-plane thermal conductivity was calculated from the in-plane thermal diffusivity ($\alpha_{||}$), density (ρ), and specific heat (C_P) as

$$k_{||} = \alpha_{||} \cdot \rho \cdot C_P \qquad \text{(S2)}$$

Photoacoustic method

The cross-plane thermal conductivity was determined by the photoacoustic method. It uses the photoacoustic effect to determine the thermal properties of a sample. Therefore, a modulated laser beam (λ = 488 nm) periodically heats the sample. For good absorption of the laser energy a thin Au transducer layer (~ 150 nm) was coated on the sample surface. For photoacoustic characterization, the samples were spray-coated on a glass substrate. The layout of the measurement cell above the sample is shown in Figure S12A. The gas tight cell is filled with a helium pressure of 20 psi. The microphone (Bruel&Kjaer, 4398-A-011) connected to the cell measures an acoustic wave, which is induced by the periodic heat conduction from the transducer layer surface to the gas phase. As shown in Figure S12B, the microphone is linked to a lock-in amplifier with integrated signal generator (Zurich instruments, HF2LI). The signal generator controls the electro-optic modulator (EOM, Conoptics, M25A) and therefore the frequency of the modulated laser beam. The acoustic signal detected by the microphone is then transferred into a phase and amplitude shift in relation to the modulation of the incident laser beam.

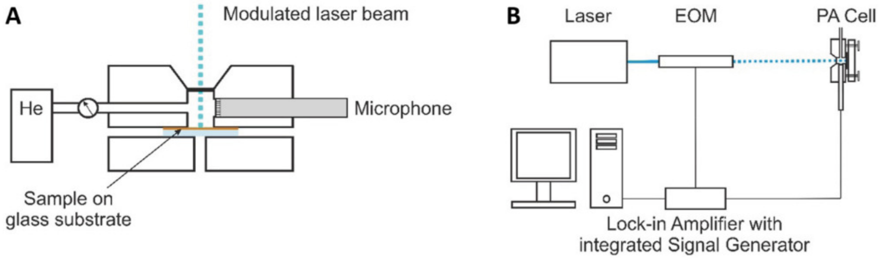

Figure S12. Scheme of photoacoustic measurements. (A) The photoacoustic cell. (B) The whole setup.

The phase shift is detected as a function of the frequency in a range from 110 Hz to 4000 Hz. The signal is then normalized with the phase shift signal of a thermally thick glass sample (1 mm) with known thermal properties. A representative frequency sweep is shown in Figure S13. The red line indicates the best fit according to the fitting procedure presented by Singh et al..[6] They used the generalized multilayer model of Hu et al.[7] assuming one-dimensional heat transfer. The unknown fitting parameters are the contact resistance between the gold layer and the sample, the thermal diffusivity of the sample, and the contact resistance between sample and substrate. For thin films the fit is not very sensitive to the individual parameters, but to the total layer resistance. Therefore, only the total layer resistance is reported. From the total layer resistance it is possible to calculate the effective thermal conductivity by dividing with the thickness. The thickness of the samples was determined by AFM measurements. The values of the total layer resistance and sample thickness are summarized in Table S3. For each Hec/PVP ratio samples with three different thicknesses were measured to exclude influences from the sample thickness.

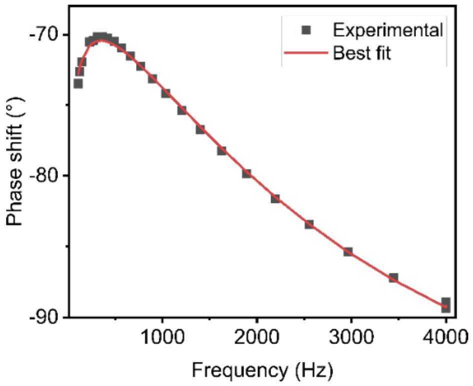

Figure S13. Normalized photoacoustic phase signal. Representative photoacoustic measurement of the Hec31/PVP69 sample with a thickness of 1.979 µm. The red line shows the best fit.

Table S3. Summary of the photoacoustic measurements. The total layer resistance, the thickness, and the resulting effective cross-plane thermal conductivity are given for each sample.

Sample	Total layer resistance [mm² K W^{-1}]	Thickness [µm]	Effective cross-plane thermal conductivity [W m^{-1} K^{-1}]
Hec100/PVP0	1.58	0.28	0.177
Hec100/PVP0	2.55	0.595	0.234
Hec100/PVP0	4.34	0.94	0.217
Hec51/PVP49	3.69	0.255	0.069
Hec51/PVP49	7.74	0.722	0.093
Hec51/PVP49	11.53	0.957	0.083
Hec40/PVP60	6.54	0.463	0.071
Hec40/PVP60	14.03	1.139	0.081
Hec40/PVP60	18.96	1.987	0.105
Hec31/PVP69	8.20	0.744	0.091
Hec31/PVP69	17.58	1.382	0.079
Hec31/PVP69	24.06	1.979	0.082
Hec23/PVP77	8.81	0.568	0.064
Hec23/PVP77	17.45	1.677	0.096
Hec23/PVP77	26.37	2.568	0.097
Hec0/PVP100	2.26	0.351	0.155
Hec0/PVP100	4.50	0.792	0.176

Section S3. Brillouin light spectroscopy

Brillouin Light Spectroscopy (BLS) measures the phonon dispersion, i.e., the wave vector, **q,** dependent sound velocity, $v_i(\mathbf{q})$, by detecting the Doppler frequency shift, *f,* in laser light inelastically scattered by sound waves ("phonons"). Since the phonon modes in question are thermally populated, the Bragg condition for light scattering is satisfied independent of the scattering angle, in contrast to the kindred time-domain ("picosecond ultrasonic") techniques that require external phonon injection via special sample preparation. Since the latter typically involves deposition of non-transparent metallic transducer films, they also do not readily allow for transmission and backscattering measurements, further limiting the potential of these techniques for probing anisotropic materials.

Assuming a planar sample, BLS can be conducted in three scattering geometries: transmission, reflection, and backscattering. For angle-dependent measurements in the transmission and reflection geometries, the laser source (λ = 532 nm) was mounted on a goniometer and rotated around the sample, similar to a wide-angle X-ray (WAXS) setup. For the transmission geometry (top-right inset to Figure 3B), the propagation vector, **q,** of the sound wave lies in the plane of the sample and its modulus, $|\mathbf{q}|$, is independent of the refractive index according to $|\mathbf{q}|_{\parallel} = (4\pi/\lambda)\sin\beta$, with *β* being the light incident angle. For the reflection geometry, the Bragg condition is fulfilled for sound waves with **q** along the normal to the sample plane, so that $|\mathbf{q}| = (4\pi/\lambda)\sqrt{n^2 - \sin^2\beta}$, with *n* being the refractive index of the sample.[8] In order to find *n*, several points at different *β* were acquired, and then fit linearly; *n* was determined under the constraint that the fit has to pass through the origin (Figure S14A), and the obtained values are reported in Table S4. In contrast to the transmission geometry, the range of the dispersion relationship that can be scanned by varying $|\mathbf{q}|_{\perp}$ is more restricted due to refraction of the laser beam at the air-sample boundary. Finally, backscattering measurements can be conducted, where the incident and scattered light traverse the same path, and the sample is mounted on a rotating stage with angular gradation marks. Only a single dispersion point, corresponding to **q** directed opposite to $\mathbf{k}_i$ in the film and of a magnitude, $|\mathbf{q}| = 4\pi n/\lambda$, is accessible in the backscattering geometry, but all possible $\mathbf{q}/|\mathbf{q}|$ directions can be probed. Because backscattering measurements use the same lens for focusing the incident and collimating scattered light, the alignment of the setup is generally much easier, so that all the backscattering spectra were acquired with microscope objectives (typically 10x) to reduce the spectrum accumulation time.

From the given formulas, it is easy to see that the Brillouin frequency shift does not exceed $2nv/\lambda$, where *v* is sound velocity. These frequencies render viscoelasticity effects negligible and are detected using a high-resolution six-pass Tandem Fabry Perot (TFP) interferometer (JRS Instruments, Switzerland) optimized for the 1-50 GHz range. Values still further out on the dispersion relationship can be accessed using, for example, picosecond ultrasonic interferometry (PUI), but at the expense of great effort and without any gain in information for the problem at hand.[9] Finally, BLS also offers direct access to the shear moduli, simply by analyzing scattered light in different polarizations: VV (i.e., vertical incident and vertical scattered light) corresponds to quasi-longitudinal and quasi-transverse phonon modes, and VH (i.e., vertical incident and horizontal scattered light) to the pure-transverse phonon mode (for transversely isotropic samples, HV does not show a transverse peak). Before the BLS measurements, the samples were dried at 100 °C in a vacuum chamber for one week to remove any residual water content.

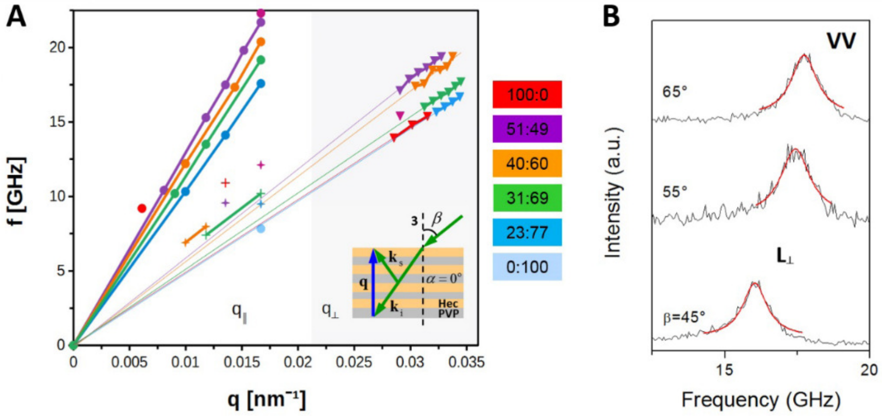

Figure S14. BLS experiments in the reflection geometry. (A) Dispersion (frequency vs. wave vector) of the longitudinal (L) and transverse (T) phonons in the hybrid stacks and the two constituent components (see the color code) obtained from the polarized (VV) and depolarized (VH) BLS spectra recorded in the reflection geometry (inset). (B) Typical VV spectra of the Hec31/PVP69 hybrid film at three laser incident angles.

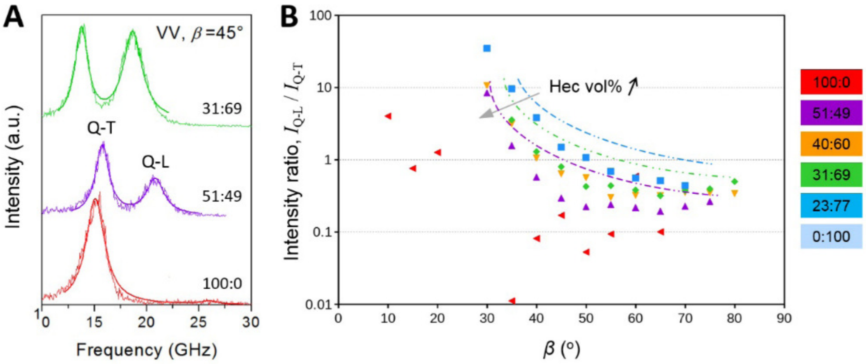

Figure S15. BLS spectra and peak intensity. (A) Polarized (VV) BLS spectra recorded in the backscattering geometry (inset to Figure 3A) for two hybrid stacks and the pure Hec film at an incident angle of 45°. (B) The intensity ratio of the Q-L and Q-T peaks in backscattering VV spectra vs. the laser incident angle.

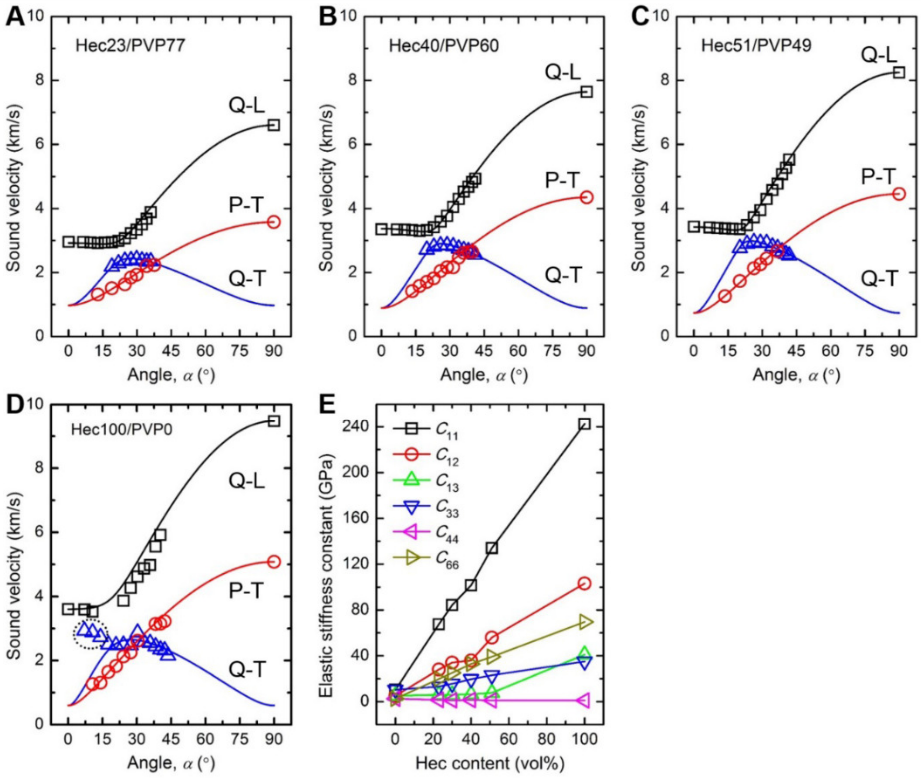

Figure S16. Direction-dependent sound velocities of hybrid stack films. (A) Hec23/PVP77, (B) Hec40/PVP60, (C) Hec51/PVP49, and (D) Hec100/PVP0 (the data points in the dotted circle were not used in the fitting). Q-L, P-T, and Q-T represent the quasi-longitudinal, pure-transverse, and quasi-transverse phonon modes, respectively. (E) Variation of the elastic stiffness constants with the Hec volume fraction.

Based on the BLS-measured direction-dependent sound velocities, we obtained the elastic tensor within the framework of the Christoffel equation.[10]

$$\begin{bmatrix} \Gamma_{11}-\rho v^2 & \Gamma_{12} & \Gamma_{13} \\ \Gamma_{21} & \Gamma_{22}-\rho v^2 & \Gamma_{23} \\ \Gamma_{31} & \Gamma_{32} & \Gamma_{33}-\rho v^2 \end{bmatrix} \begin{bmatrix} u_1 \\ u_2 \\ u_3 \end{bmatrix} = \begin{bmatrix} 0 \\ 0 \\ 0 \end{bmatrix}, \qquad \text{(S3)}$$

where ρ is the density of the sample, v is the sound velocity, $\mathbf{u} = [u_1,\ u_2,\ u_3]^{\mathrm{T}}$ is the displacement vector, and Γ_{ik} (i, k = 1, 2, 3) is the Christoffel stress, which is defined as

$$\Gamma_{ik} = \sum_{j=1}^{3}\sum_{l=1}^{3} C_{ijkl}\, n_j n_l \,. \qquad \text{(S4)}$$

Here, C_{ijkl} denotes an element of the 4th rank elastic tensor, and $\mathbf{n} = [n_1,\ n_2,\ n_3]^{\mathrm{T}}$ represents the phonon propagation direction.

For a transversely isotropic material, the elastic tensor, in the Voigt notation, has the following form.[11]

$$\mathbf{C} = \begin{bmatrix} C_{11} & C_{12} & C_{13} & & & \\ C_{12} & C_{11} & C_{13} & & & \\ C_{13} & C_{13} & C_{33} & & & \\ & & & C_{44} & & \\ & & & & C_{44} & \\ & & & & & C_{66} = \dfrac{C_{11}-C_{12}}{2} \end{bmatrix}, \tag{S5}$$

and contains five independent stiffness constants. After some algebra, the sound velocities of the Q-L, Q-T, and P-T modes along a direction defined by *α* can be represented as follows,

$$v_{\text{Q-L}}(\alpha) = \sqrt{\frac{-A_1 + \sqrt{A_1^2 - 4A_2}}{2\rho}} \tag{S6}$$

$$v_{\text{Q-T}}(\alpha) = \sqrt{\frac{-A_1 - \sqrt{A_1^2 - 4A_2}}{2\rho}} \tag{S7}$$

$$v_{\text{P-T}}(\alpha) = \sqrt{\frac{A_3}{\rho}}, \tag{S8}$$

where,

$$A_1 = -(\sin^2\alpha C_{11} + \cos^2\alpha C_{33} + C_{44}) \tag{S9}$$

$$A_2 = \sin^4\alpha C_{11}C_{44} + \sin^2\alpha\cos^2\alpha(C_{11}C_{33} - C_{13}^2 - 2C_{13}C_{44}) + \cos^4\alpha C_{33}C_{44}. \tag{S10}$$

$$A_3 = \sin^2\alpha C_{66} + \cos^2\alpha C_{44}. \tag{S11}$$

Through nonlinear χ^2 fitting of the BLS-measured sound velocities (i.e., *v* vs. *α*) with Equations (S6)-(S8), we obtained the elastic stiffness constants as well as their uncertainties.[12] The χ^2 is defined as

$$\chi^2 = \sum_i \frac{\left[v_{i,\,\text{fit}}(C_{11},\, C_{12},\, C_{13},\, C_{33},\, C_{44},\, \alpha) - v_{i,\,\text{exp}}(\alpha)\right]^2}{(\Delta v_{i,\,\text{exp}})^2}, \tag{S12}$$

where $v_{\text{i, fit}}$ and $v_{\text{i, exp}}$ are the fitted and experimental sound velocities, respectively, $\Delta v_{\text{i, exp}}$ is the uncertainty of the measured sound velocity, and the summation is over all experimental sound velocities. By considering the uncertainties of the measured angles, refractive indices, and phonon frequencies, we estimated $\Delta v_{\text{i, exp}}$ to be $0.02v_{\text{i, exp}}$. We imposed the following constraints for the elastic stiffness constants[13]: (1) $C_{11} > |C_{12}|$, (2) $C_{44} > 0$, and (3) $C_{33}(C_{11}+C_{12}) > 2C_{13}^2$, which ensure positive Young's and shear moduli. The availability of experimental data for all the Q-L, Q-T, and P-T modes allows unique determination of C_{11}, C_{12}, C_{13}, C_{33}, and C_{44}.

After that, we calculated the engineering mechanical properties,[11] which include the in-plane Young's modulus ($E_{||}$), cross-plane Young's modulus ($E_{\perp}$), sliding shear modulus (G_{13}), torsional shear modulus (G_{12}), and two characteristic Poisson's ratios (ν_{31} and ν_{12}). Note that only five of the engineering mechanical properties are independent (typically, $\{E_{||}, E_{\perp}, G_{13}, G_{12}, \nu_{31}\}$ or $\{E_{||}, E_{\perp}, G_{13}, \nu_{12}, \nu_{31}\}$ are chosen). Also note that to be consistent with the direction-dependent thermal conductivity results, we used subscripts, "$\parallel$" and "$\perp$", to represent directions parallel and perpendicular to the sample film, respectively, rather than directions parallel and perpendicular to the "3"-axis (i.e., the symmetry axis), as seen in typical analysis of transversely isotropic materials. The relevant mechanical properties are summarized in Tables S4 and S5.

Table S4. Summary of elastic stiffness constants. Composition (Hec vol%, Hec wt%), density (ρ), refractive index (n), and elastic stiffness constants (C_{11}, C_{12}, C_{13}, C_{33}, C_{44}, and C_{66}) of the Hec/PVP hybrid Bragg stack films.

Sample ID	**Hec vol%**	**Hec wt%**	**ρ (g/cm^3)**	**n**	**C_{11} (GPa)**	**C_{12} (GPa)**	**C_{13} (GPa)**	**C_{33} (GPa)**	**C_{44} (GPa)**	**C_{66} (GPa)**
Hec0/PVP100	0	0	1.20	1.53*	10.4	5.2	5.2	10.4	2.6	2.6
Hec23/PVP77	23	40	1.55	1.54	67.6 ±1.7	28.0 ±1.9	6.0 ±1.2	13.2 ±0.3	1.5 ±0.1	19.8 ±0.5
Hec31/PVP69	31	50	1.62	1.50	84.3 ±1.5	34.0 ±1.8	6.1 ±1.5	15.7 ±0.3	1.2 ±0.2	25.1 ±0.5
Hec40/PVP60	40	60	1.74	1.47	101.6 ±1.8	35.9 ±2.2	6.5 ±1.8	19.7 ±0.4	1.4 ±0.1	32.9 ±0.6
Hec51/PVP49	51	70	1.97	1.45	134.1 ±2.2	55.9 ±2.9	7.7 ±2.3	23.0 ±0.5	1.1 ±0.1	39.1 ±0.9
Hec100/PVP0	100	100	2.70	1.40	242.5 ±6.2	103.2 ±6.7	40.9 ±5.2	35.0 ±0.9	1.0 ±0.1	69.6 ±1.2

*Source: https://refractiveindex.info/?shelf=organic&book=polyvinylpyrrolidone&page=Konig.

Table S5. Summary of engineering mechanical properties. Composition (Hec vol%, Hec wt%) and engineering mechanical properties of the Hec/PVP hybrid Bragg stack films. $E_{\parallel}$: in-plane Young's modulus; $E_{\perp}$: cross-plane Young's modulus; G_{13}, G_{23}: sliding shear moduli; G_{12}: torsional shear modulus; ν_{31}, ν_{32}, ν_{12}: Poisson's ratios (ν_{ij} represents the strain response in the j-direction due to a strain in the i-direction). Note that in Reference [11] ν_{31} was mistakenly denoted as ν_{13}.

Sample ID	**Hec vol%**	**Hec wt%**	$E_{\parallel}$ **(GPa)**	$E_{\perp}$ **(GPa)**	$\frac{E_{\parallel}}{E_{\perp}}$	**G_{13} = G_{23} (GPa)**	**G_{12} (GPa)**	$\nu_{31}=\nu_{32}$	ν_{12}
Hec0/PVP100	0	0	7.0	7.0	1	2.6	2.6	0.33 (assumed)	0.33 (assumed)
Hec23/PVP77	23	40	55.0 ±2.5	12.5 ±0.4	4.4	1.5 ±0.1	19.8 ±0.5	0.06 ±0.01	0.39 ±0.03
Hec31/PVP69	31	50	69.7 ±2.3	15.1 ±0.4	4.6	1.2 ±0.2	25.1 ±0.5	0.05 ±0.01	0.39 ±0.02
Hec40/PVP60	40	60	88.1 ±2.6	19.1 ±0.5	4.6	1.4 ±0.1	32.9 ±0.6	0.05 ±0.01	0.34 ±0.02
Hec51/PVP49	51	70	109.9 ±3.5	22.4 ±0.6	4.9	1.1 ±0.1	39.1 ±0.9	0.04 ±0.01	0.41 ±0.02
Hec100/PVP0	100	100	178.9 ±9.9	25.4 ±2.6	7.0	1.0 ±0.1	69.6 ±1.2	0.12 ±0.02	0.29 ±0.06

Section S4. Evaluation of interfacial thermal conductance

The series resistance model (SRM) shown in Figure 4F illustrates a hybrid stack unit cell consisting of one Hec layer and one PVP layer. We describe the corrugation of the Hec nanosheet (Figure 1B) by a thermal interface conductance, $G_{\mathrm{Hec/PVP}}$. For the unit cell in Figure 4F, the total thermal resistance can be calculated as $\frac{d_{\mathrm{XRD}}}{k_{\perp}} = \frac{d_{\mathrm{Hec}}}{k_{\mathrm{Hec}}} + \frac{d_{\mathrm{PVP}}}{k_{\mathrm{PVP}}} + \frac{2}{G_{\mathrm{Hec/PVP}}}$, where d_{XRD} is the basal spacing as determined by XRD (Table S1), $k_{\perp}$ is the effective cross-plane thermal conductivity, $d_{\mathrm{Hec}} = 10$ Å, and $d_{\mathrm{PVP}} = d_{\mathrm{XRD}} - d_{\mathrm{Hec}}$. For the thermal conductivity of the two components, we used the following values: $k_{\mathrm{Hec}} = 5.71$ W m^{-1} K^{-1}, and $k_{\mathrm{PVP}} = 0.17$ W m^{-1} K^{-1}. The Hec/PVP interfacial conductance, $G_{\mathrm{Hec/PVP}}$, is determined by least squares fitting of the experimental $k_{\perp}$ data (red solid line in Figure 4C) to be 89 ± 8 MW m^{-2} K^{-1}, which falls well into the range of interfacial conductance reported for inorganic/organic interfaces.[14] We also obtained the Hec/Hec interfacial conductance, $G_{\mathrm{Hec/Hec}} = 219 \pm 28$ MW m^{-2} K^{-1}, by considering a unit cell consisting of one Hec layer and one Hec/Hec interface (i.e., $\frac{d_{\mathrm{XRD}}}{k_{\perp}} = \frac{d_{\mathrm{Hec}}}{k_{\mathrm{Hec}}} + \frac{1}{G_{\mathrm{Hec/Hec}}}$).

Section S5. Uncertainty analysis

The uncertainties (standard deviations) of the data reported in this work were analyzed by taking into account the instrument accuracy, repetitive measurements, and propagation of uncertainties. The sound velocities were estimated to have an error bar of 2%. The uncertainties of the elastic stiffness constants were determined according to Zgonik et al..[12] The uncertainties of the engineering mechanical properties were calculated according to principles of uncertainty propagation. For instance,

$$E_{\perp} = C_{33} - \frac{2C_{13}^2}{C_{11} + C_{12}} \tag{S13}$$

$$\Delta E_{\perp} = \sqrt{\sum_{ij=11,\,12,\,13,\,33} \left(\frac{\partial E_{\perp}}{\partial C_{ij}}\right)^2 \left(\Delta C_{ij}\right)^2 + \sum_{\substack{ij,\,kl=11,\,12,\,13,\,33 \\ ij<kl}} 2\frac{\partial E_{\perp}}{\partial C_{ij}}\frac{\partial E_{\perp}}{\partial C_{kl}}\left(\Delta C_{ij}\right)\left(\Delta C_{kl}\right)} \tag{S14}$$

where $\frac{\partial E_{\perp}}{\partial C_{11}} = \frac{2C_{13}^2}{(C_{11}+C_{12})^2}$, $\frac{\partial E_{\perp}}{\partial C_{12}} = \frac{2C_{13}^2}{(C_{11}+C_{12})^2}$, $\frac{\partial E}{\partial C_{13}} = -\frac{4C_{13}}{C_{11}+C_{12}}$, and $\frac{\partial E_{\perp}}{\partial C_{33}} = 1$. Similar expressions can be derived for the other engineering moduli and the Poisson's ratios.

The uncertainties of the thermal measurement results are analyzed in a similar way, i.e., by considering uncertainty propagation. For example,

$$k_{\parallel} = \alpha_{\parallel}\rho C_P \tag{S15}$$

$$\Delta k_{\parallel} = \sqrt{\left(\frac{\partial k_{\parallel}}{\partial \alpha_{\parallel}}\right)^2 \left(\Delta \alpha_{\parallel}\right)^2 + \left(\frac{\partial k_{\parallel}}{\partial \rho}\right)^2 \left(\Delta \rho\right)^2 + \left(\frac{\partial k_{\parallel}}{\partial C_P}\right)^2 \left(\Delta C_P\right)^2} \tag{S16}$$

where $\frac{\partial k_{\parallel}}{\partial \alpha_{\parallel}} = \rho C_P$, $\frac{\partial k_{\parallel}}{\partial \rho} = \alpha_{\parallel} C_P$, and $\frac{\partial k_{\parallel}}{\partial C_P} = \alpha_{\parallel}\rho$. Here we assumed negligible covariance terms. Similar expressions can be derived for $k_{\perp}$, $k_{\parallel}/k_{\perp}$, $\bar{\Lambda}$, etc.

The uncertainties of the data are reported as error bars in the figures shown in the main text and Supporting Information. For clarity, error bars smaller than the symbol size are not shown.

References

[1] a) J. Breu, W. Seidl, A. J. Stoll, K. G. Lange, T. U. Probst, *Chem. Mater.* **2001**, *13*, 4213-4220; b) M. Stöter, D. A. Kunz, M. Schmidt, D. Hirsemann, H. Kalo, B. Putz, J. Senker, J. Breu, *Langmuir* **2013**, *29*, 1280-1285.

[2] S. Rosenfeldt, M. Stöter, M. Schlenk, T. Martin, R. Q. Albuquerque, S. Förster, J. Breu, *Langmuir* **2016**, *32*, 10582-10588.

[3] D. M. Moore, R. C. Reynolds, D. M., *X-ray Diffraction and the Identification and Analysis of Clay Minerals*, Oxford University Press, Oxford, U.K., **1997**.

[4] E. S. Tsurko, P. Feicht, F. Nehm, K. Ament, S. Rosenfeldt, I. Pietsch, K. Roschmann, H. Kalo, J. Breu, *Macromolecules* **2017**, *50*, 4344-4350.

[5] a) A. Salazar, A. Mendioroz, R. Fuente, *Appl. Phys. Lett.* **2009**, *95*, 121905; b) A. Mendioroz, R. Fuente-Dacal, E. Apinaniz, A. Salazar, *Rev. Sci. Instrum.* **2009**, *80*, 074904.

[6] V. Singh, T. L. Bougher, A. Weathers, Y. Cai, K. Bi, M. T. Pettes, S. A. McMenamin, W. Lv, D. P. Resler, T. R. Gattuso, D. H. Altman, K. H. Sandhage, L. Shi, A. Henry, B. A. Cola, *Nat. Nanotechnol.* **2014**, *9*, 384-390.

[7] H. Hu, X. Wang, X. Xu, *J. Appl. Phys.* **1999**, *86*, 3953-3958.

[8] T. Still, *High frequency acoustics in colloid-based meso- and nanostructures by spontaneous Brillouin light scattering*, 1 ed., Springer-Verlag Berlin Heidelberg, **2010**.

[9] C. Klieber, *Ultrafast photo-acoustic spectroscopy of super-cooled liquids*, Massachusetts Institute of Technology, **2010**.

[10] a) S. P. Cheadle, R. J. Brown, D. C. Lawton, *Geophysics* **1991**, *56*, 1603-1613; b) M. Mah, D. R. Schmitt, *Geophysics* **2001**, *66*, 1217-1225.

[11] S. Cusack, A. Miller, *J. Mol. Biol.* **1979**, *135*, 39-51.

[12] M. Zgonik, P. Bernasconi, M. Duelli, R. Schlesser, P. Günter, M. H. Garrett, D. Rytz, Y. Zhu, X. Wu, *Phys. Rev. B* **1994**, *50*, 5941-5949.

[13] F. Mouhat, F.-X. Coudert, *Phys. Rev. B* **2014**, *90*, 4104.

[14] a) M. D. Losego, M. E. Grady, N. R. Sottos, D. G. Cahill, P. V. Braun, *Nat. Mater.* **2012**, *11*, 502-506; b) W. L. Ong, S. M. Rupich, D. V. Talapin, A. J. McGaughey, J. A. Malen, *Nat. Mater.* **2013**, *12*, 410-415.

Author Contributions

M.R., J.B., and G.F. initialized the idea. T.S. explored and optimized the Hec/PVP system, fabricated the hybrid Bragg stacks, and characterized their structures. K.R. conducted the BLS experiments. A.P. conducted and analyzed the lock-in thermography measurements to obtain the in-plane thermal conductivity. P.H. performed and analyzed the photoacoustic characterization to obtain the cross-plane thermal conductivity and measured the sample densities. A.F.K. conducted additional lock-in thermography measurements and contributed to the lock-in thermography analysis. A.L. conducted and analyzed the DSC measurements to obtain the specific heat. Z.W. analyzed the BLS data and established the correlation between the mechanical moduli and thermal conductivity. Z.W., M.R., J.B., and G.F. wrote the manuscript. All authors have given approval to the final version of the manuscript. †These authors contributed equally.

7 Impact of Ultraconfinement on Composite Barriers

Theresa Schilling,[§] Christoph Habel,[§] Sabine Rosenfeldt, Maximilian Röhrl, Josef Breu*

[§] These authors contributed equally to this work

This work was published in *ACS Appl. Polym. Mater.* **2020**, *2*, 3010-3015.

Individual contribution:

The manuscript was written through contributions of all authors. All authors have given approval to the final version of the manuscript. I explored and optimized the Hec/PVP system, fabricated and characterized the Hec/PVP films. Christoph Habel conducted and analyzed the OTR measurements to obtain the oxygen permeability. Sabine Rosenfeldt recorded the SAXS measurements. Maximilian Röhrl assisted Christoph Habel with the OTR measurements.

ACS APPLIED POLYMER MATERIALS

pubs.acs.org/acsapm Article

Impact of Ultraconfinement on Composite Barriers

Theresa Schilling,[†] Christoph Habel,[†] Sabine Rosenfeldt, Maximilian Röhrl, and Josef Breu*

Cite This: *ACS Appl. Polym. Mater.* 2020, 2, 3010–3015 Read Online

ACCESS | Metrics & More | Article Recommendations | Supporting Information

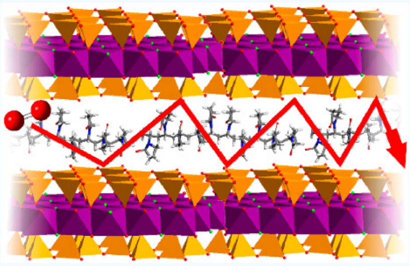

ABSTRACT: Flexible optoelectronic packaging is required to provide an ultrahigh barrier to oxygen under ambient conditions, meaning at a relative humidity above 50%. Many polymeric packaging materials, however, adsorb water vapor and the consequential softening is detrimental for the barrier properties. Despite its importance, systematic studies on the impact of the relative humidity (RH) on the oxygen permeability (OP) of clay nanocomposite barriers and convincing evidence for a potential hydrophobization due to compounding with nanosheets are scarce. Especially at filler contents greater than 30 vol %, as required for ultrahigh barriers, a severe confinement is imposed on interlayered polymer and thus its permeability properties are expected to be significantly modified as compared to the bulk. A systematic study of the relation between permeability and RH requires nanocomposite films that differ in filler content but at the same time are comparable with respect to aspect ratio, filler type, quality of texture, and one-dimensional crystallinity. By applying water-soluble polyvinylpyrrolidone (PVP) and ultrahigh-aspect-ratio synthetic clay (sodium fluorohectorite), we were able to prepare hybrid samples that meet these requirements for the first time. By spray coating, the components self-assemble into hybrid films of one-dimensional crystalline Bragg stacks. Two such hybrid films with filler contents of 31 and 40 vol % were fabricated. Indeed, the filler content was found to greatly affect the dependence of the oxygen permeability on RH. Comparing the performance of these two films, the OP in the 40 vol % sample was four times lower than would be expected because of the increase in filler content. To the best of our knowledge, this is the first convincing evidence for a pronounced confinement effect on the permeability.

KEYWORDS: *clay, hybrid films, swelling, Cussler, oxygen permeability, ultraconfinement*

INTRODUCTION

Although having prominent uses in the electronics, automotive, and building sectors, nearly 40% of polymers are consumed in the packaging sector.[1] Besides mechanical protection against shocks and vibrations, the main application-relevant feature of packaging material is the oxygen barrier that protects food from aerobic microbial spoilage and biochemical reactions like fat oxidation.[2] Best-before dates of packed food strongly correlate with the barrier performance of the packaging. Optoelectronic devices are even more sensitive to oxygen, leading to barrier requirements being orders of magnitude higher than for food packaging.

In general, the permeability (P) of the barrier coating is given by $P = SD$, where S and D are solubility and diffusivity constants of the permeates, respectively.[3] S depends on the affinity of permeates to the matrix wherein polar molecules are generally more soluble in polar than in nonpolar matrices and vice versa. At low relative humidity (RH), hydrophilic polymers possess excellent barrier properties for hydrophobic permeates like oxygen (see poly(vinyl alcohol) (PVA)[4] in Figure 1). However, at ambient conditions, the packaging will swell with water vapor, which inevitably leads to an increase in oxygen permeability (OP)[5,6] because dissolved water mole-

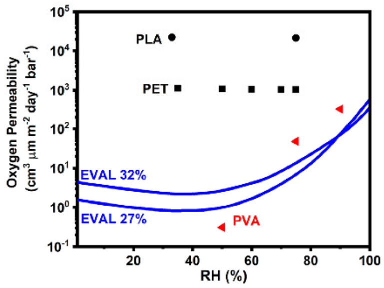

Figure 1. Nonlinear dependence of oxygen permeability of two EVAL types (% corresponds to the ethylene content).[15] Polyethylene terephthalate (PET, own measurement), PVA,[4] and polylactic acid (PLA)[16] values are giving for comparison.

Received: April 29, 2020
Accepted: May 28, 2020
Published: June 12, 2020

https://dx.doi.org/10.1021/acsapm.0c00456
ACS Appl. Polym. Mater. 2020, 2, 3010–3015

cules act as softener and increase segment mobility.[7] Alternatively, D can be reduced by the incorporation of crystalline, and thus impermeable, fillers like layered silicates (clay), which increase the diffusion path (tortuous pathway). For semidiluted systems with high-aspect-ratio fillers, Cussler's theory[8] predicts that D depends nonlinearly on the aspect ratio (α) and volume fraction (ϕ) of the filler (eq 1).

$$P_{\mathrm{rel}} = \frac{P}{P_0} = \left(1 + \mu\left(\frac{\alpha^2\phi^2}{1-\phi}\right)\right)^{-1} \tag{1}$$

with P = permeability of the filled polymer matrix, P_0 = permeability of the neat polymer matrix, ϕ = filler content (volume fraction), α = aspect ratio ($\alpha = d/h$, diameter d, height h) of the filler, and μ = geometrical factor of the filler depending on its shape.

Cussler's theory assumes that confinement of the polymer matrix, interlayered between clay nanosheets, does not alter its properties. In particular, it is assumed that the permeability of interlayered and bulk polymer is the same. At filler contents greater than 30 vol %, as required for ultrahigh barriers, the confinement of the polymer is, however, quite severe: Given a thickness of a single clay nanosheet of 1 nm and an equidistant arrangement as required for a homogeneous nanocomposite, the slit between adjacent nanosheets at 31 vol % is as narrow as 2 nm. This easily falls beneath the interlayered polymer's radius of gyration. Clearly, such a severe confinement is expected to significantly alter the polymer properties as compared to the bulk properties. In the literature, the impact of the confinement on the segment mobility,[9] glass transition temperature,[10−12] and viscosity[13] was proven. In this paper, we will now investigate the role of polymer confinement on permeability.

In commercial packaging materials, the moisture sensitivity of the barrier performance is compensated by laminating the hydrophilic polymer with a more hydrophobic polymer.[14] Alternatively, the hydrophobicity can be tuned via copolymerization. For instance, copolymers like poly(ethylene-*co*-vinyl alcohol) (EVOH) or laminates of it with polyethylene are widely used high-performance polymers for flexible barrier packaging with low OP.[15]

The moisture sensitivity of EVOH barrier films can be tuned by adjusting the ratio of the two monomers (Figure 1).[15,17,18] More hydrophilic EVOH (f.e. EVAL with an ethylene content of 27%) show lower OP at low and medium RH but at the same time are more sensitive to increasing RH. Consequently, at some RH values, the barrier performance of a more hydrophobic EVOH (f.e. EVAL with an ethylene content of 32%) becomes superior. To meet the requirements of a particular application with given RH specification, the ethylene content has to be adjusted. Quite counterintuitively, both EVAL types show a minor but significant decrease in OP between 0 and 40% RH (Figure 1). This phenomenon has been attributed to adsorption of water molecules filling up of free volume, thus leading to a reduced OP due to a lower diffusivity.[19,20]

Clays not only reduce permeability in a nonselective manner via the tortuous path mechanism but also have been claimed to hydrophobize polar, water-soluble polymer matrices. It has been shown that the critical RH, where swelling followed by a significant loss of oxygen barrier sets in, can be shifted to higher RH by compounding with sodium montmorillonite.[6,21,22] Choudalakis and Gotsis have suggested that this might be related to a modification of the structure and/or the crystallinity of the polymer matrix and a change of the free volume.[23] The incorporation of clay into a spider silk matrix was shown to increase the amount of crystalline ß-sheet domains in addition to a reduction in free volume and sensitivity to water.[24] This hydrophobization effect was furthermore observed for a PVA-modified clay nanocomposite[4] where swelling was shown to be retarded, resulting in low oxygen transmission rates at elevated RH. The swelling of nanocomposite films with a one-dimensional (1D) regular stacking (Bragg stacks) of polymer (polyethylenimine and poly(acrylic acid)) and a synthetic sodium fluorohectorite was found to be influenced by the quality of 1D crystallinity. The better ordered, the better the barrier observed at 38 °C and 90% RH.[25] Because of partial phase segregation, the volume of polymer matrix in the smectic domains was, however, invariant to the filler content. Consequently, this segregation did not allow for a systematic study on the impact of the volume ratio of clay to polymer matrix on the dependence of OP on RH.

With polyvinylpyrrolidone (PVP) as polymer matrix, phase segregation is not observed and 1D periodically homogeneous nanocomposite films (Bragg stacks) are obtained. These Bragg stack films represent a model system, which allow us to realize two different polymer confinements (with polymer contents of 31 vol % and 40 vol %) without affecting the 1D crystallinity, quality of texture, aspect ratio, or filler type. These materials allow, for the first time, a study on the swelling behavior of PVP in the confined space of two 1D crystalline Bragg stack films with varying clay content. Moreover, the impact of the confinement effect and the moisture sensitivity on the OP is studied and compared for two otherwise comparable nanocomposites.

■ EXPERIMENTAL SECTION

Materials. The synthetic clay sodium fluorohectorite (Hec, $[\mathrm{Na}_{0.5}]^{\mathrm{inter}}[\mathrm{Mg}_{2.5}\mathrm{Li}_{0.5}]^{\mathrm{oct}}[\mathrm{Si4}]^{\mathrm{tet}}\mathrm{O}_{10}\mathrm{F}_2$) was obtained via melt synthesis followed by long-term annealing, according to an established procedure.[26,27] PVP (M_w = 40 000 g mol^{-1}) was provided by Sigma-Aldrich.

Film Preparation and Characterization. The as-synthesized Hec was delaminated by immersing it into Millipore water (0.2 vol %). PVP was dissolved in Millipore water (0.8 vol %) and added in the desired volume ratio. The suspension was mixed for at least 1 day in an overhead shaker. The quality of the suspension, in terms of homogeneity, was crosschecked by small-angle X-ray scattering (SAXS).

The nanocomposite films sprayed on a PET foil (36 μm, Bleher Folientechnik, Germany) were prepared by employing a fully automatic spray coating system. Every spraying cycle is followed by a drying cycle of 90 s at a temperature of 55 °C. The films were characterized by X-ray diffraction (XRD), transmission electron microscopy (TEM), and thermogravimetric analysis (TGA). Oxygen transmission rates (OTR) were measured on a Mocon OX-TRAN 2/21 (XL) instrument (Minneapolis, USA). Additional information about the sample preparation and characterization methods can be found in Sections S1 and S2.

■ RESULTS AND DISCUSSION

Synthetic sodium fluorohectorite (Hec, $[\mathrm{Na}_{0.5}]^{\mathrm{inter}}[\mathrm{Mg}_{2.5}\mathrm{Li}_{0.5}]^{\mathrm{oct}}[\mathrm{Si}_4]^{\mathrm{tet}}\mathrm{O}_{10}\mathrm{F}_2$) is an excellent material for barrier applications. Hec shows the rare phenomenon of osmotic swelling. By immersing the Hec crystals into deionized water, osmotic swelling allows for complete and gentle delamination of the Hec crystals into 1 nm thick nanosheets while preserving the large diameter of 20 μm.[27] This way,

https://dx.doi.org/10.1021/acsapm.0c00456
ACS Appl. Polym. Mater. 2020, 2, 3010−3015

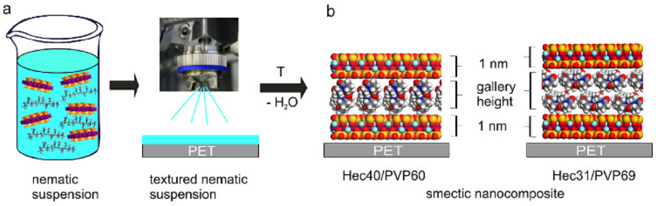

Figure 2. Schematic of the processing method of the perfectly ordered Hec/PVP Bragg stack film. (a) Homogeneous ternary nematic dispersion comprising Hec, PVP, and water. The ternary dispersion spray coated on a corona-treated PET foil. (b) Upon drying, the components self-assemble into a hybrid film where PVP chains are confined in the interlayer space between two 1 nm thick nanosheets. The gallery heights are 1.3 and 2.0 nm for Hec40/PVP60 and Hec31/PVP69, respectively. The observed gallery heights correspond to a monolayer and a bilayer of PVP for Hec40/PVP60 and Hec31/PVP69, respectively.

highly flexible platy fillers with high aspect ratio (>20 000) are obtained without needing brute force sonication or purification. Because of the large aspect ratio, rotation of the nanosheets in suspension is hindered. Therefore, even very dilute suspensions of Hec (<1 vol %) form nematic phases.[28]

As reported for titanate nanosheets,[29] dilute aqueous dispersions of negatively charged Hec nanosheets adopt a cofacial arrangement because of strong electrostatic repulsion. In this nematic state, adjacent clay nanosheets are not only held in a coherent cofacial geometry but are also separated to long distances determined by the clay content, typically exceeding 50 nm.[28] Mixing this Hec dispersion with different amounts of an aqueous PVP solution allows the polymer to diffuse between adjacent Hec sheets (Figure 2a), yielding a perfectly homogeneous nematic hybrid phase consisting of water, Hec, and PVP, as verified by a basal series being observed in the SAXS traces (Figure 3).

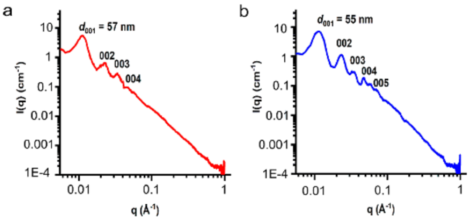

Figure 3. One-dimensional SAXS pattern of the concentrated gel sample (a) Hec40/PVP60 and (b) Hec31/PVP69. The varying layer separations observed are related to the clay content of the suspension rather than the Hec/PVP ratio.

Because of the transverse flexibility[30] of the 1 nm thin clay sheets and the huge aspect ratio of ~20 000, upon spray coating and subsequent drying the components self-assembled into 1D crystalline (Bragg-stack or smectic film[31]) nanocomposite films aligned parallel to the substrate (Figure 2b). At high filler content, the confinement of the polymer chains reaches a point where the height of the gallery between the nanosheets is the same order of magnitude as the molecular size of a polymer chain. Because the polymer matrix will always try to arrange itself in a dense packing between the nanosheets, only distinct polymer volumes, which depend on the diameter of a given polymer chain, allow for a regular stacking. The packing/size requirements and volume ratios match only for particular filler contents (31 and 40 vol %). Only then may homogeneous, 1D crystalline nanocomposite films (Figure 4)[25,31] be obtained, resulting in gallery heights (PVP layer thickness) of 1.3 and 2.0 nm, respectively. Here, the two samples were denoted as Hec31/PVP69 and Hec40/PVP60, with the numbers indicating the volume fractions, as crosschecked by TGA (Figure S1 and Table S1).

The XRD patterns of the hybrid films show rational 00*l* series with sharp and intense basal reflections up to the ninth order (Figure 4a, b). According to Meuring's rules,[32] the quality of the 1D crystalline order is further confirmed by a low coefficient of variation[32] and a small full width at half-maximum (Table S1). For Hec/PVP nanocomposites, phase segregation can safely be ruled out as the observed gallery heights were in accordance with the volume ratios (for details, see the Supporting Information) applied for fabricating the films. This perfect periodic homogeneity over large areas is further confirmed by TEM micrographs (Figure 4c, d). The nanocomposite films therefore may alternatively be considered as single-phase hybrid materials, of which we recently characterized the thermomechanical coupling.[33]

The two nanocomposite films with a filler content of 31 and 40 vol % are comparable in terms of crystalline order, homogeneity, type of polymer matrix and filler, aspect ratio of the filler, and the quality of texture but differ solely in the filler content. By comparing these two well-defined hybrid materials, the influence of the confinement on the moisture sensitivity can be systematically evaluated. Given the 1D crystallinity, the monitoring of swelling is particularly easy. With stepwise increase in the RH, both hybrid films swelled significantly as indicated by increasing gallery height (Figure 5a). Normalizing the increase to the gallery height at 0% RH showed that the water uptake is almost identical for both films (Figure 5b). For the less-filled hybrid film (Hec31/PVP69), the relative change in PVP volume is slightly higher than for the more-filled hybrid film (Hec40/PVP60), but only differs by less than 15%.

This observation is somewhat in contrast to a literature report,[34] where a more pronounced swelling was suggested when PVP was deposited alternating with montmorillonite clay via layer by layer (LbL) deposition. The LbL films, however, represent laminates of pure clay layers alternating with pure polymer layers, a segregated structure quite different from the hybrids investigated here. Comparing the swelling behavior of Hec40/PVP60 and Hec31/PVP69 suggested that increasing the Hec content reduces water vapor adsorption of the hybrid films slightly.

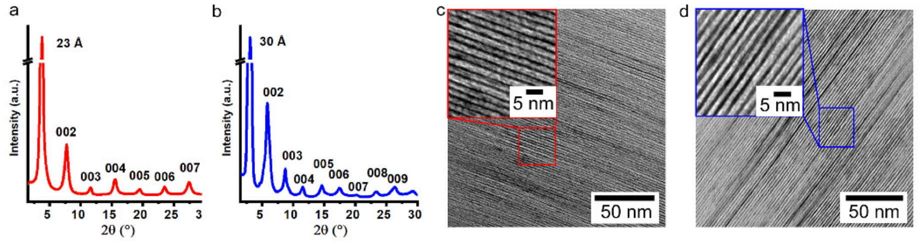

Figure 4. XRD patterns and microscopic images of the 1D periodically homogeneous nanocomposite films. XRD pattern of (a) Hec40/PVP60 and (b) Hec31/PVP69 with a rational series of 001-reflections up to the ninth order. Cross-sectional TEM images of (c) Hec40/PVP60 and (d) Hec31/PVP69 confirm the perfect translationally periodic homogeneity over large areas.

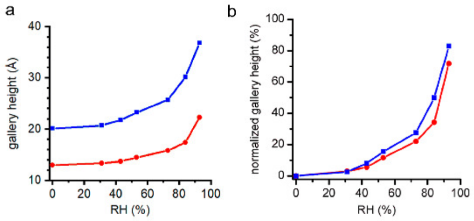

Figure 5. Study of the swelling behavior. (a) Absolute gallery height as a function of RH (red = Hec40/PVP60, blue = Hec31/PVP69). (b) Increase of the gallery height, normalized to the value at 0% RH, as a function of RH (red = Hec40/PVP60, blue = Hec31/PVP69).

Oxygen transmission rates (OTR) measured at various RH are, however, the much more sensitive probe for moisture sensitivity (Table S2). For applications, absolute OTR are the relevant features. However, transmissions rates are largely influenced by the thickness of the barrier coatings and even the transmission rate of the substrate. Therefore, the performance of the barrier coatings can only be compared by converting transmission rates into OP. For conversion, it is generally assumed that the rate is inversely proportional to the thickness (2.1 and 3.0 μm for Hec40/PVP60 and Hec31/PVP69, respectively).[35] Upon conversion of OTR values into OP values, the contribution of the PET substrate is subtracted according to Roberts et al.[36]

For water-soluble polymers, the sensitivity to RH, and consequently the deterioration of the barrier, is a well-known adverse phenomenon, as discussed in the Introduction.[5,6,37] However, as also discussed in the Introduction, up to a certain threshold value (<35% RH) the OP slightly decreases (Figure 6), as previously observed for EVAL[15] (Figure 1) and cellulose films.[19] Although both hybrid films adsorb water commencing at low RH, as indicated by the increasing gallery height (Figure 5a), initially the adsorbed water has no negative impact on the OP. The offset of swelling and breakdown of the barrier has been reported before. Wang et al.[19] and Muramatsu et al.[20] suggested that at the early stages of swelling, the adsorbed water is filling the free volume in the system, and thus leads to a lower diffusivity.[20] Above this threshold value (>35% RH), the permeability of Hec31/PVP69 increased from 0.024 (0% RH) to 0.796 $cm^3\ \mu m\ m^{-2}\ day^{-1}\ bar^{-1}$ (75% RH) and of Hec40/PVP60 from 0.002 (0% RH) to 0.143 $cm^3 \mu m\ m^{-2}\ day^{-1}\ bar^{-1}$ (75% RH).

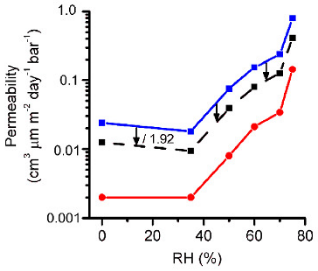

Figure 6. Oxygen permeability in logmarithic scaling of Hec40/PVP60 (red) and Hec31/PVP69 (blue) as a function of RH. According to Cussler's theory, the OP of Hec31/PVP69 should be reduced by a factor of 1.92 because of the increase in the filler content from 31 to 40 vol % (displayed as dashed black line).

Throughout the complete RH range, the OP of the more-filled hybrid film (Hec40/PVP60) was reduced by a factor of around 8. Because aspect ratio (α), geometrical factor (μ), and permeability of the neat polymer matrix (P_0) are the same for both nanocomposite films, according to Cussler's theory, the permeability is expected to be reduced by only a factor of 1.92 (see Section S3 for details) when increasing the filler content from 31 vol % (Hec31/PVP69) to 40 vol % (Hec40/PVP60) (Figure 6). The relative reduction observed in OP between Hec31/PVP69 and Hec40/PVP60 clearly cannot be attributed to the effect of increasing filler content as predicted by Cussler's theory. The effect is actually a factor of ≈4 larger than what is expected from Cussler's theory. As both hybrid films are identical except for the filler content, we propose this factor to be due to the differing confinement of the interlayered polymer sandwiched between the Hec nanosheets. Wang et al.[33] recently proposed, that the gallery height of the Hec/PVP hybrid film of 1.3 and 2 nm is related to the principle axes of 1.0 and 1.3 nm of the PVP chain itself. The gallery heights of Hec40/PVP60 and Hec31/PVP69 are consistent to a monolayer and a bilayer (Figure 2b), respectively. As recently suggested by Eckert et al.,[9] the segment mobility of a polymer chain within the confined space is significantly reduced. This is expected to diminish the diffusivity of low-molecular-weight components like oxygen and thus reduce the OP. This observation suggests that besides the nonlinear dependence of diffusivity on the aspect ratio and the volume fraction of filler considered by Cussler, additionally,

https://dx.doi.org/10.1021/acsapm.0c00456
ACS Appl. Polym. Mater. 2020, 2, 3010−3015

a linear effect of confinement exists at high filler content and thus severe confinement.

■ CONCLUSION

Periodically ordered Hec/PVP hybrid films represent model systems perfectly suited to study the impact of confinement on oxygen permeability. The model system allows for fabrication of nanocomposite films that are identical regarding homogeneity, crystallinity, and type and aspect ratio of filler, but that differ in filler content. Ranging from 0% to 75% of RH, the offset in permeability of these two films is much greater than what could be attributed to the increase of tortuous path predicted by Cussler's theory. This observation is attributed to the reduction of segment mobility by severe polymer confinement as encountered in highly filled homogeneous nanocomposites.

■ ASSOCIATED CONTENT

Supporting Information

The Supporting Information is available free of charge at https://pubs.acs.org/doi/10.1021/acsapm.0c00456.

> Detailed information about the film preparation and characterization with instrumental details; a table with an overview of the OTR and OP values and the approximation of Cussler's equation (PDF)

■ AUTHOR INFORMATION

Corresponding Author

Josef Breu − *Bavarian Polymer Institute and Department of Chemistry, University of Bayreuth, Bayreuth 95447, Germany;* orcid.org/0000-0002-2547-3950; Email: josef.breu@uni-bayreuth.de

Authors

Theresa Schilling − *Bavarian Polymer Institute and Department of Chemistry, University of Bayreuth, Bayreuth 95447, Germany*

Christoph Habel − *Bavarian Polymer Institute and Department of Chemistry, University of Bayreuth, Bayreuth 95447, Germany*

Sabine Rosenfeldt − *Bavarian Polymer Institute and Department of Chemistry, University of Bayreuth, Bayreuth 95447, Germany*

Maximilian Röhrl − *Bavarian Polymer Institute and Department of Chemistry, University of Bayreuth, Bayreuth 95447, Germany*

Complete contact information is available at: https://pubs.acs.org/10.1021/acsapm.0c00456

Author Contributions

[†]T.S. and C.H. contributed equally to this work. The manuscript was written through contributions of all authors. All authors have given approval to the final version of the manuscript. T.S. explored and optimized the Hec/PVP system and fabricated and characterized the Hec/PVP films. C.H. conducted and analyzed the OTR measurements to obtain the oxygen permeabilities.

Funding

This work was supported by the German Science Foundation (DFG) within the collaborative research projects SFB 840 and SFB 1357.

Notes

The authors declare no competing financial interest.

■ ACKNOWLEDGMENTS

The authors thank Florian Puchtler for producing the synthetic clay and Marco Schwarzmann for the transmission electron microscopy images. Moreover, we thank Renee Timmins for proofreading the manuscript. T.S. and C.H. thank the Elite Network of Bavaria for financial and other support. We appreciate the support of the Keylab for Optical and Electron Microscopy of the Bavarian Polymer Institute (BPI).

■ REFERENCES

(1) *Plastics−The Facts 2018: An Analysis of European Plastics Production, Demand and Waste Data*; PlasticsEurope: Brussels, Belgium, 2018.

(2) Akelah, A. Polymers in Food Packaging and Protection. In *Functionalized Polymeric Materials in Agriculture and the Food Industry*; Springer: Boston, 2013; pp 293−347.

(3) Sabu, T.; Kuruvilla, J.; Malhotra, S. K.; Goda, K.; Sreekala, M. S. *Polymer Composites*; Wiley−VCH: Weinheim, Germany, 2013; Vol. 2.

(4) Tsurko, E. S.; Feicht, P.; Habel, C.; Schilling, T.; Daab, M.; Rosenfeldt, S.; Breu, J. Can high oxygen and water vapor barrier nanocomposite coatings be obtained with a waterborne formulation? *J. Membr. Sci.* **2017**, *540*, 212−218.

(5) Mo, C.; Yuan, W.; Lei, W.; Shijiu, Y. Effects of Temperature and Humidity on the Barrier Properties of Biaxially-oriented Polypropylene and Polyvinyl Alcohol Films. *J. Appl. Packag. Res.* **2014**, *6*, 40−46.

(6) Grunlan, J. C.; Grigorian, A.; Hamilton, C. B.; Mehrabi, A. R. Effect of clay concentration on the oxygen permeability and optical properties of a modified poly(vinyl alcohol). *J. Appl. Polym. Sci.* **2004**, *93*, 1102−1109.

(7) Robertson, G. L. *Food Packaging: Principles and Practice*; Taylor & Francis Group: Boca Raton, FL, 2006.

(8) Cussler, E. L.; Hughes, S. E.; Ward, W. J.; Aris, R. Barrier membranes. *J. Membr. Sci.* **1988**, *38*, 161−174.

(9) Eckert, A.; Abbasi, M.; Mang, T.; Saalwächter, K.; Walther, A. Structure, Mechanical Properties, and Dynamics of Polyethylenoxide/Nanoclay Nacre-Mimetic Nanocomposites. *Macromolecules* **2020**, *53*, 1716−1725.

(10) Zhang, C.; Guo, Y.; Priestley, R. D. Glass Transition Temperature of Polymer Nanoparticles under Soft and Hard Confinement. *Macromolecules* **2011**, *44*, 4001−4006.

(11) Qin, X.; Xia, W.; Sinko, R.; Keten, S. Tuning Glass Transition in Polymer Nanocomposites with Functionalized Cellulose Nanocrystals through Nanoconfinement. *Nano Lett.* **2015**, *15*, 6738−44.

(12) Kang, E.; Graczykowski, B.; Jonas, U.; Christie, D.; Gray, L. A. G.; Cangialosi, D.; Priestley, R. D.; Fytas, G. Shell Architecture Strongly Influences the Glass Transition, Surface Mobility, and Elasticity of Polymer Core-Shell Nanoparticles. *Macromolecules* **2019**, *52*, 5399−5406.

(13) Johnson, K. J.; Glynos, E.; Maroulas, S.-D.; Narayanan, S.; Sakellariou, G.; Green, P. F. Confinement Effects on Host Chain Dynamics in Polymer Nanocomposite Thin Films. *Macromolecules* **2017**, *50*, 7241−7248.

(14) López-Rubio, A.; Hernández-Muñoz, P.; Gimenez, E.; Yamamoto, T.; Gavara, R.; Lagarón, J. M. Gas barrier changes and morphological alterations induced by retorting in ethylene vinyl alcohol-based food packaging structures. *J. Appl. Polym. Sci.* **2005**, *96*, 2192−2202.

(15) Kuraray Relative Humidity. http://www.evalevoh.com/en/eval-properties/barrier-to-oxygen/relative-humidity.aspx (accessed 2020-01-29).

(16) Habel, C.; Schöttle, M.; Daab, M.; Eichstaedt, N. J.; Wagner, D.; Bakhshi, H.; Agarwal, S.; Horn, M. s. A.; Breu, J. High-Barrier, Biodegradable Food Packaging. *Macromol. Mater. Eng.* **2018**, *303*, 1800333.

(17) Lange, J.; Wyser, Y. Recent Innovations in Barrier Technologies for Plastic Packaging - a Review. *Packag. Technol. Sci.* **2003**, *16*, 149−158.

(18) Zhang, Z.; Britt, I. J.; Tung, M. A. Permeation of oxygen and water vapor through EVOH films as influenced by relative humidity. *J. Appl. Polym. Sci.* **2001**, *82*, 1866−1872.

(19) Wang, J.; Gardner, D. J.; Stark, N. M.; Bousfield, D. W.; Tajvidi, M.; Cai, Z. Moisture and Oxygen Barrier Properties of Cellulose Nanomaterial-Based Films. *ACS Sustainable Chem. Eng.* **2018**, *6*, 49−70.

(20) Muramatsu, M.; Okura, M.; Kuboyama, K.; Ougizawa, T.; Yamamoto, T.; Nishihara, Y.; Saito, Y.; Ito, K.; Hirata, K.; Kobayashi, Y. Oxygen permeability and free volume hole size in ethylene−vinyl alcohol copolymer film: temperature and humidity dependence. *Radiat. Phys. Chem.* **2003**, *68*, 561−564.

(21) Song, Y.; Gerringer, J.; Qin, S.; Grunlan, J. C. High Oxygen Barrier Thin Film from Aqueous Polymer/Clay Slurry. *Ind. Eng. Chem. Res.* **2018**, *57*, 6904−6909.

(22) Ding, F.; Liu, J.; Zeng, S.; Xia, Y.; Wells, K. M.; Nieh, M. P.; Sun, L. Biomimetic nanocoatings with exceptional mechanical, barrier, and flame-retardant properties from large-scale one-step coassembly. *Sci. Adv.* **2017**, *3*, e1701212.

(23) Choudalakis, G.; Gotsis, A. D. Free volume and mass transport in polymer nanocomposites. *Curr. Opin. Colloid Interface Sci.* **2012**, *17*, 132−140.

(24) Doblhofer, E.; Schmid, J.; Riess, M.; Daab, M.; Suntinger, M.; Habel, C.; Bargel, H.; Hugenschmidt, C.; Rosenfeldt, S.; Breu, J.; Scheibel, T. Structural Insights into Water-Based Spider Silk Protein-Nanoclay Composites with Excellent Gas and Water Vapor Barrier Properties. *ACS Appl. Mater. Interfaces* **2016**, *8*, 25535−43.

(25) Tsurko, E. S.; Feicht, P.; Nehm, F.; Ament, K.; Rosenfeldt, S.; Pietsch, I.; Roschmann, K.; Kalo, H.; Breu, J. Large Scale Self-Assembly of Smectic Nanocomposite Films by Doctor Blading versus Spray Coating: Impact of Crystal Quality on Barrier Properties. *Macromolecules* **2017**, *50*, 4344−4350.

(26) Breu, J.; Seidl, W.; Stoll, A. J.; Lange, K. G.; Probst, T. U. Charge Homogeneity in Synthetic Fluorohectorite. *Chem. Mater.* **2001**, *13*, 4213−4220.

(27) Stöter, M.; Kunz, D. A.; Schmidt, M.; Hirsemann, D.; Kalo, H.; Putz, B.; Senker, J.; Breu, J. Nanoplatelets of sodium hectorite showing aspect ratios of approximately 20,000 and superior purity. *Langmuir* **2013**, *29*, 1280−1285.

(28) Rosenfeldt, S.; Stöter, M.; Schlenk, M.; Martin, T.; Albuquerque, R. Q.; Förster, S.; Breu, J. In-Depth Insights into the Key Steps of Delamination of Charged 2D Nanomaterials. *Langmuir* **2016**, *32*, 10582−10588.

(29) Sano, K.; Kim, Y. S.; Ishida, Y.; Ebina, Y.; Sasaki, T.; Hikima, T.; Aida, T. Photonic water dynamically responsive to external stimuli. *Nat. Commun.* **2016**, *7*, 12559.

(30) Kunz, D. A.; Erath, J.; Kluge, D.; Thurn, H.; Putz, B.; Fery, A.; Breu, J. In-plane modulus of singular 2:1 clay lamellae applying a simple wrinkling technique. *ACS Appl. Mater. Interfaces* **2013**, *5*, 5851−5855.

(31) Wong, M.; Ishige, R.; White, K. L.; Li, P.; Kim, D.; Krishnamoorti, R.; Gunther, R.; Higuchi, T.; Jinnai, H.; Takahara, A.; Nishimura, R.; Sue, H. J. Large-scale self-assembled zirconium phosphate smectic layers via a simple spray-coating process. *Nat. Commun.* **2014**, *5*, 3589.

(32) Moore, D. M.; Reynolds, R. C.; M, D. *X-ray Diffraction and the Identification and Analysis of Clay Minerals*; Oxford University Press: Oxford, U.K., 1997.

(33) Wang, Z.; Rolle, K.; Schilling, T.; Hummel, P.; Philipp, A.; Kopera, B. A. F.; Lechner, A. M.; Retsch, M.; Breu, J.; Fytas, G. Tunable Thermoelastic Anisotropy in Hybrid Bragg Stacks with Extreme Polymer Confinement. *Angew. Chem., Int. Ed.* **2020**, *59*, 1286−1294.

(34) Holder, K. M.; Priolo, M. A.; Secrist, K. E.; Greenlee, S. M.; Nolte, A. J.; Grunlan, J. C. Humidity-Responsive Gas Barrier of Hydrogen-Bonded Polymer−Clay Multilayer Thin Films. *J. Phys. Chem. C* **2012**, *116*, 19851−19856.

(35) Siracusa, V. Food Packaging Permeability Behaviour: A Report. *Int. J. Polym. Sci.* **2012**, *2012*, 1687−1697.

(36) Roberts, A. P.; Henry, B. M.; Sutton, A. P.; Grovenor, C. R. M.; Briggs, G. A. D.; Miyamoto, T.; Kano, M.; Tsukahara, Y.; Yanaka, M. Gas permeation in silicon-oxide/polymer (SiOx/PET) barrier films: role of the oxide lattice, nano-defects and macro-defects. *J. Membr. Sci.* **2002**, *208*, 75−88.

(37) Tang, M. C.; Agarwal, S.; Alsewailem, F. D.; Choi, H. J.; Gupta, R. K. A model for water vapor permeability reduction in poly(lactic acid) and nanoclay nanocomposites. *J. Appl. Polym. Sci.* **2018**, *135*, 46506.

Supporting Information

Impact of Ultraconfinement on Composite Barriers

Theresa Schilling,‡1 *Christoph Habel,*‡1 *Sabine Rosenfeldt,*1 *Maximilian Röhrl,*1 *Josef Breu*1*

1Bavarian Polymer Institute and Department of Chemistry, University of Bayreuth, Universitätsstraße 30, 95447 Bayreuth, Germany

‡ equal contribution

KEYWORDS: clay, hybrid films, swelling, Cussler, oxygen permeability, ultraconfinement

* Corresponding author

E-Mail: Josef.Breu@uni-bayreuth.de

Section S1. Materials and Film preparation

Materials

The synthetic clay sodium fluorohectorite (Hec, $[Na_{0.5}]^{inter}[Mg_{2.5}Li_{0.5}]^{oct}[Si4]^{tet}O_{10}F_2$) was synthesized via melt synthesis followed by long-term annealing, according to an established procedure.[1-2] The material featured a cation exchange capacity of 1.27 mmol g^{-1}. PVP (Mw = 40000 g mol^{-1}) was provided by Sigma Aldrich.

Film preparation

For repulsive delamination by osmotic swelling,[2-3] the synthetic Hec was immersed into Millipore water (0.2 vol%). The aqueous PVP solution (0.8 vol%) was added in the desired weight ratio. This dispersion of Hec and PVP was homogenized by mixing for at least 1 day in the overhead shaker (Figure 2a).

The barrier coatings were prepared by spray coating. The fully automatic spray coating system was equipped with a SATA 4000 LAB HVLP 1.0 mm spray gun (SATA GmbH & Co. KG, Germany). Dispersions were sprayed on a corona-treated polyethylene terephthalate (PET) foil (36 µm, Bleher Folientechnik, Germany). The spraying and nozzle pressure were set constant at values of 2 and 4 bar, respectively. The thickness of the dispersion layer applied in one spraying step is ≈ 2 µm, which corresponds to ≈ 20 nm dry nanocomposite film thickness (Figure 3c). For drying the dispersion layer, the sample was stopped under infrared lamps until evaporation of the solvent was complete. After every spraying cycle, a drying cycle of 90 s with a temperature of 55 °C took place. The spraying/drying cycle was repeated 80 times. Afterwards, the film was dried at 100 °C for 3 days under vacuum (10^{-3} bar).

Section S2. Dispersion and Film Characterization

Small angle X-ray scattering. Homogeneity of the dispersions was crosschecked by small angle X-ray scattering (SAXS) measurements using the small-angle X-ray system "Ganesha AIR" (SAXSLAB, Denmark). The X-ray source of this laboratory-based system is a rotating anode (copper, MicroMax 007HF, Rigaku Corporation, Japan). The data were recorded by a position sensitive detector (PILATUS 300 K, Dectris). To cover the range of scattering vectors between 0.02-0.85 $Å^{-1}$, different detector positions were used. The measurements of the dispersions were done in 1 mm glass capillaries (Hilgenberg, code 4007610, Germany) at room temperature. To improve the detection limit of the in-house machine, the dispersions were first concentrated to ≈ 10 wt% by centrifugation.

Thermogravimetric analysis. To rule out compositional changes during spray coating, these ratios were cross-checked (Table S1) by thermogravimetric analysis (TGA), using a Linseis STA PT 1600 (Linseis Messgeräte GmbH, Germany). Changes in mass observed upon heating in synthetic air up to 800 °C were attributed to the combustion of PVP. (Figure S1).

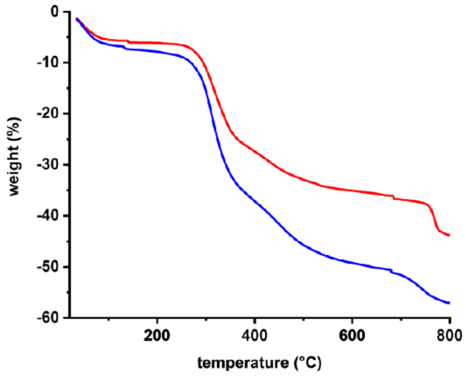

Figure S1. TGA curves of Hec40/PVP60 (red) and Hec31/PVP69 (blue). The weight loss below 200 °C corresponds to the water.

X-ray diffraction. XRD patterns of the films were recorded in Bragg-Brentano-geometry on an Empyrean diffractometer (PANalytical B.V.; the Netherlands) using Cu K_α radiation ($\lambda = 1.54187$ Å). The films were placed on glass slides (Menzel-Gläser; Thermo Scientific). Prior to measurements at 0% RH, samples were dried at 100 °C for one week in a vacuum chamber (10^{-3} bar). For the measurements of XRD patterns at varying RH, the samples were equilibrated for 1 week above saturated $MgCl_2$ $6H_2O$ (32% RH), K_2CO_3 (43% RH), $Mg(NO_3)_2$ (53% RH), NaCl (75% RH) KCl (84% RH) and KNO_3 (94% RH), respectively.

Calculation of the nominal gallery height:

Ruling out phase segregation

While XRD would be blind for segregated amorphous polymer volumes, it is, however, representative for the bulk of the nanocomposite films, since the X-ray beam is sampling large areas. Moreover, a more detailed evaluation of the XRD trace, including the crystallographic analysis for potential defects, renders it conclusive for ruling out phase segregation: The XRD pattern showed a rational *00l*-series characterized by a low coefficient of variation (Figure 4), emphasizing that the hybrid film is periodically homogenous over long ranges (more precisely: > the coherence length of the X-ray beam, which is typically 50 nm). In addition, the periodicity of the Hec/PVP film can be calculated via the volume fraction of PVP and Hec. In a 1D ordered Bragg film, the latter corresponds to the thickness of the Hec platelet. As calculated and observed gallery heights are identical (Table S1), within experimental certainty, phase segregation can be ruled out. The segregated polymer volume would be "missing" in the galleries and would not allow for such a perfect agreement.

Assuming PVP and Hec densities of 1.2 g cm^{-3} and 2.7 g cm^{-3}, respectively, nominal gallery height can be calculated for the various volume ratios (nominal gallery height in Table S1).[4] They agree reasonably with those obtained from XRD measurements (observed gallery height in Table S1). The gallery height corresponds to the *d*-spacing minus the Hec platelet height of 0.96 nm.

Table S1. Overview of the structural and chemical characterization at 0 % RH.

sample	nominal Hec:PVP ratio [wt%]	nominal Hec:PVP ratio [vol%]	PVP content * [wt%]	PVP content ** [vol%]	Nominal gallery height [nm]	Observed gallery height [nm]	CV [%]	FWHM [°2θ]
Hec40/PVP60	60:40	40:60	38	58	1.3	1.3	1.3	0.3
Hec31/PVP69	50:50	31:69	49	68	2.0	2.0	1.0	0.3

CV: coefficient of variation; FWHM: full width at half maximum

* determined by TGA (Fig. S2); ** calculated with the PVP content determined by TGA;

Transmission electron microscopy. Transmission electron microscopy (TEM) images were taken on a JEOL JEM-2200FS (JEOL GmbH, Germany) at an acceleration voltage of 200 kV. Cross-section pictures of the self-supporting films were prepared with a Cryo Ion Slicer IB-09060CIS (JEOL, Germany).

Oxygen transmission rates. Oxygen transmission rates (OTR) were measured on a Mocon OX-TRAN 2/21 and a Mocon OX-TRAN 2/21 XL instrument (Minneapolis, USA) with a lower detection limit of 0.05 $cm^3 m^{-2} day^{-1} bar^{-1}$ and 0.0005 $cm^3 m^{-2} day^{-1} bar^{-1}$, respectively. The measurements were conducted at 23 °C and RH of 0%, 35%, 50%, 60%, 70% and 75%. All films were carefully conditioned at the relevant RH until the samples reached equilibrium.

Table S2. Overview of the oxygen transmission rates and oxygen permeabilities.

RH (%)	Hec40/PVP60 (2.1 μm)	Hec31/PVP69 (3.0 μm)	Hec40/PVP60 (2.1 μm)	Hec31/PVP69 (3.0 μm)
	OTR (cm^3 m^{-2} day^{-1} bar^{-1})		OP (cm^3 μm m^{-2} day^{-1} bar^{-1})	
0	0.001	0.008	0.002	0.024
35	0.001	0.006	0.002	0.018
50	0.004	0.025	0.008	0.075
60	0.010	0.051	0.021	0.153
70	0.016	0.080	0.034	0.240
75	0.068	0.263	0.143	0.796

Profilometer. The thickness of the films was measured with a Veeco Dektak 150 Surface Profiler (Veeco Instruments, USA). Six measurements were taken at different spots of the films and averaged.

Section S3. Approximation of Cussler's equation

$$\frac{P_1}{P_2}=\frac{1+\mu\frac{\alpha^2\phi_2{}^2}{1-\phi_2}}{1+\mu\frac{\alpha^2\phi_1{}^2}{1-\phi_1}}$$

With α = const.=20000, μ = const.= 4/9, 0.3≤ ϕ ≤ 0.4 ➔ $\alpha^2\cdot\mu > 177000000$:

➔ **Equation simplified to**

$$\frac{P_1}{P_2}=\frac{\mu\frac{\alpha^2\phi_2{}^2}{1-\phi_2}}{\mu\frac{\alpha^2\phi_1{}^2}{1-\phi_1}}=\frac{\frac{\phi_2{}^2}{1-\phi_2}}{\frac{\phi_1{}^2}{1-\phi_1}}$$

For ϕ_1= 0.31 and ϕ_2= 0.4: $\frac{P_1}{P_2}$ = **1.92**

References

(1) Breu, J.; Seidl, W.; Stoll, A. J.; Lange, K. G.; Probst, T. U. Charge Homogeneity in Synthetic Fluorohectorite. *Chem. Mater.* **2001,** *13*, 4213-4220.

(2) Stöter, M.; Kunz, D. A.; Schmidt, M.; Hirsemann, D.; Kalo, H.; Putz, B.; Senker, J.; Breu, J. Nanoplatelets of sodium hectorite showing aspect ratios of approximately 20,000 and superior purity. *Langmuir* **2013,** *29*, 1280-1285.

(3) Rosenfeldt, S.; Stöter, M.; Schlenk, M.; Martin, T.; Albuquerque, R. Q.; Förster, S.; Breu, J. In-Depth Insights into the Key Steps of Delamination of Charged 2D Nanomaterials. *Langmuir* **2016,** *32*, 10582-10588.

(4) Tsurko, E. S.; Feicht, P.; Nehm, F.; Ament, K.; Rosenfeldt, S.; Pietsch, I.; Roschmann, K.; Kalo, H.; Breu, J. Large Scale Self-Assembly of Smectic Nanocomposite Films by Doctor Blading versus Spray Coating: Impact of Crystal Quality on Barrier Properties. *Macromolecules* **2017,** *50*, 4344-4350.

8 One-dimensional crystalline clay nacre-mimetics with record filler contents (73 -91 vol%): From brittle to ductile to brittle

Theresa Schilling, Daniel Wagner, Olli Ikkala, Josef Breu

Individual contribution:

I designed and planned the experiments and wrote the manuscript with Josef Breu. Moreover, I. explored and optimized the Hec/PEG system, fabricated and characterized the Hec/PEG films, and performed and analyzed the tensile testing measurements. Daniel Wagner fabricated the DS. Olli Ikkala contributed to the discussing process.

One-dimensional crystalline clay nacre mimetics with record filler contents (73 wt% - 91 wt%): From brittle to ductile to brittle

Theresa Schilling[1], *Daniel Wagner*[1],*Olli Ikkala*[2], *Josef Breu*[1]*

[1]Bavarian Polymer Institute and Department of Chemistry, University of Bayreuth, Universitätsstr. 30, 95440 Bayreuth, Germany

[2]Center of Excellence in Molecular Engineering of Biosynthetic Hybrid Materials Research, Aalto University, FI-00076, Finland

KEYWORDS: clay, organic-inorganic hybrid composites, nacre-mimetic, mechanical properties, ultraconfinement, toughness

ASTRACT

Natural materials like nacre are a source of inspiration because of their exceptionally ordered structure and the combination of both strength and toughness. However, for synthetic nacre-mimetic composites, the production of strong but stretchable materials at high clay contents remains challenging. Systematic investigations of factors crucial for mechanical properties, require model compounds that differs in the clay content but at the same time are comparable in terms of quality of texture, type of filler, and homogeneity, best assured by one dimensional crystallinity. Here, we introduce such a model system, consisting of mono or double layer of fluorohectorite and polyethylene glycol (PEG). With this components, the filler content can be carefully adjusted in the range 73 wt% - 91 wt%. To the best of our knowledge, the latter hybrid Bragg stack represents the record filler content in a clay nacre-mimetic. Of the five hybrid

Bragg stack films only the sample consisting of a hectorite monolayer and two layers of PEG was found to be ductile with an elongation of 8% and a yielding strength of 48 MPa. While this sample can be folded like paper into origami like structures without facture, all other samples should brittle behavior resulting in catastrophic failure.

INTRODUCTION

Biological composites like wood or bones always inspired scientists for the fabrication of advanced, concomitantly strong and tough (damage-tolerant) materials of low density. A strong material can resist plastic deformation, whereas a tough material is resistant to fracture.[1-2] On a first glance, strength and toughness seem to be mutually exclusive as toughness is accompanied with the ability of a material to distribute local high stresses by limited deformation. Therefore, strong materials tend to be brittle, whereas deformable, weak materials tend to be tough. However, nature developed strategies to reconcile both mechanical properties.

One prominent example is nacre, mainly consisting of strong aragonite platelets (E = 70 GPa,[3] 95 vol%, 200-900 nm thickness, 5-8 µm diameter), hierarchically arranged in a so called brick and mortar structure, separated by a tough but weak (11 GPa,[3] 10-50 nm thickness) biopolymer.[2] While the ceramic component provides high strength, the biopolymer distributes high local stresses and dissipates energy lending toughness to nacre. The thin biopolymer layer acts as lubricant and allows limited sliding of the platelets.[4] To preserve strength and to dissipate more energy, sliding, however, needs to be limited by additional toughening mechanism like mineral bridges connecting platelets,[5] a rough aragonite surface,[6] platelet interlocking due to corrugated platelets,[6] a tortuous crack path and pull out of platelets.[1]

When mimicking nacre with an atomically flat 2D material like graphene oxide or clay, characteristics like mineral bridges, rough surfaces or platelet interlocking are hard to realize. What can be mimicked is the homogeneous periodic mechanical decoupling. This requires, however, a uniform thickness and a one-dimensionally crystalline arrangement (“hybrid Bragg stack) of the filler platelets and polymer. Since the clay filler is “fabricated” in a top down process via delamination, this process has to be thermodynamically allowed to result in uniform thickness. While the standard procedure of liquid phase exfoliation provides a broad distribution of thicknesses, the rare phenomenon of repulsive osmotic swelling yields a unique thickness controlled by thermodynamics.[7-8] Given a large diameter of the layered starting material, osmotic swelling will produce a nematic liquid crystalline phase that can be homogenously be mixed with a polymer. Upon drying a wet coat of this nematic phase, however, in all but a few cases (partial) phase segregation will be triggered (polyvinyl alcohol,[9-11] ethoxylated polyethylenimine/poly (acrylic acid),[12] sodium carboxymethyl cellulose[13]) unless a sufficient interaction with the clay surface or the interlayer cation counterpoises the segregation. Only two polymer/clay systems have been identified that form hybrid Bragg stacks with two different polymer contents: polyvinylpyrrolidone (PVP)[14-16] and polyethylenglycol (PEG).[17-19] In summary, all these requirements render a systematic variation of parameters challenging, while filler contents of more than 75 wt% could yet not be realized with a homogenous, non-segregated material.[18]

Synthetic Na-fluorohectorite not only swells osmotically allowing for utter delamination into 1 nm thick layers.[20] Due to its unique homogeneity of charge density it, moreover, can be converted into an ordered interstratification where osmotically swelling and non-swelling interlayers are stacked in an strictly alternating fashion, which then allows for delamination into double stacks of 2 nm thickness.[21-24] Together with appropriate amounts of PEG we here fabricated hybrid Bragg stacks with different, well-defined filler contents and study their mechanical performance in stress strain experiments. Moreover, two grossly different nanoplatelet diameters were applied.

EXPERIMENTAL SECTION

Materials. The synthetic clay sodium fluorohectorite (Hec, $[Na_{0.5}]^{inter}[Mg_{2.5}Li_{0.5}]^{oct}[Si4]^{tet}O_{10}F_2$) was obtained via melt synthesis followed by long-term annealing, according to an established procedure.[20, 25] PEG (Mw = 1500 g mol^{-1}) was provided by Sigma Aldrich.

Film preparation and characterization. The as-synthesized Hec was delaminated by immersing it into Millipore water (0.4 vol%). The synthesis of double stacks (DS), consisting of strictly alternating sodium and ammonium interlayers was performed according to an already published procedure.[23] For the reduction of the original diameter of Hec and DS, the suspension was sonicated with an ultrasonic horn. PEG was dissolved in Millipore water (0.8 vol%) and added in the desired weight ratio. The suspension was mixed for at least one day in an overhead shaker. The quality of the suspension, in terms of homogeneity, was crosschecked by small angle X-ray scattering (SAXS).

The nanocomposite films sprayed on a PET foil (36 µm, Bleher Folientechnik, Germany) were prepared by employing a fully automatic spray coating system. Every spraying cycle is followed by a drying cycle of 90 s at a temperature of 40 °C. The films were characterized by X-ray diffraction (XRD), transmission electron microscopy (TEM), and thermogravimetric analysis (TGA). The mechanical characteristics were determined by tensile testing with a ZwickRoell testing machine equipped with a 20N load cell. Additional information about the sample preparation and characterization methods can be found in Section S1 and S2 (**Supporting Information**).

RESULTS AND DISCUSSION

Fabrication of 1D crystalline hybrid Bragg stacks with varying filler content

Among the 2D materials, only a handful compounds are known that show repulsive osmotic swelling,[26] which allows for most gentle delamination into monolayers only while preserving the diameter pristine crystals. Synthetic sodium fluorohectorite (Hec, $[Na_{0.5}]^{inter}$ $[Mg_{2.5}Li_{0.5}]^{oct}$ $[Si_4]^{tet}$ $O_{10}F_2$), obtained by melt synthesis,[25] followed by long-term annealing,[20] shows this rare phenomenon and is moreover characterized by phase purity, homogeneous charge density and thus uniform intracrystalline reactivity. When Hec is immersed into deionized water, 1 nm thick nanoplatelets with a median diameter of 18 000 are obtained (Hec↑).[20] The suspension obtained is not isotropic but rather represents a nematic phase due to the large aspect ratio of dispersed colloids, which are held in a cofacial arrangement due to the electrostatic repulsion.

Due to its superb charge homogeneity, Hec can be transformed into an ordered interstratification by partial ion exchange with NH_4^+ resulting in strictly alternating osmotically swelling Na^+ interlayers and non-swelling NH_4^+ interlayers. When this ordered interstratification is immersed into water, it spontaneously delaminates into double stacks (DS↑),[23] where two hectorite layers are connected via a non-swelling interlayer of ammonium cations. As shown previously applying a wrinkling method,[23, 27] these DS are 15 % stiffer than monolayers with in-plane moduli of 146 GPa and 171 GPa, repectively. For customizing the diameter, ultra-sonication is applied to reduce the diameter of Hec and DS to 340 and 406 nm, respectively (Figure S1). The small diameter platelets are referred to as Hec↓ and DS↓ (Fig. 1 top).

For the synthesis of tough nanocomposites, polymers with a low glass transition temperature (Tg) are advantageous. PEG shows a Tg of -20°C, it is water soluble and non-ionic and therefore does not interfere with the repulsive nature of the nematic Hec phase. PEG, moreover, is known to form complexes with Na^+[28] and consequently it indeed forms intercalated phases with two different PEG volumes,[19] because phase separation is counterpoised by the interaction with the interlayer cation.

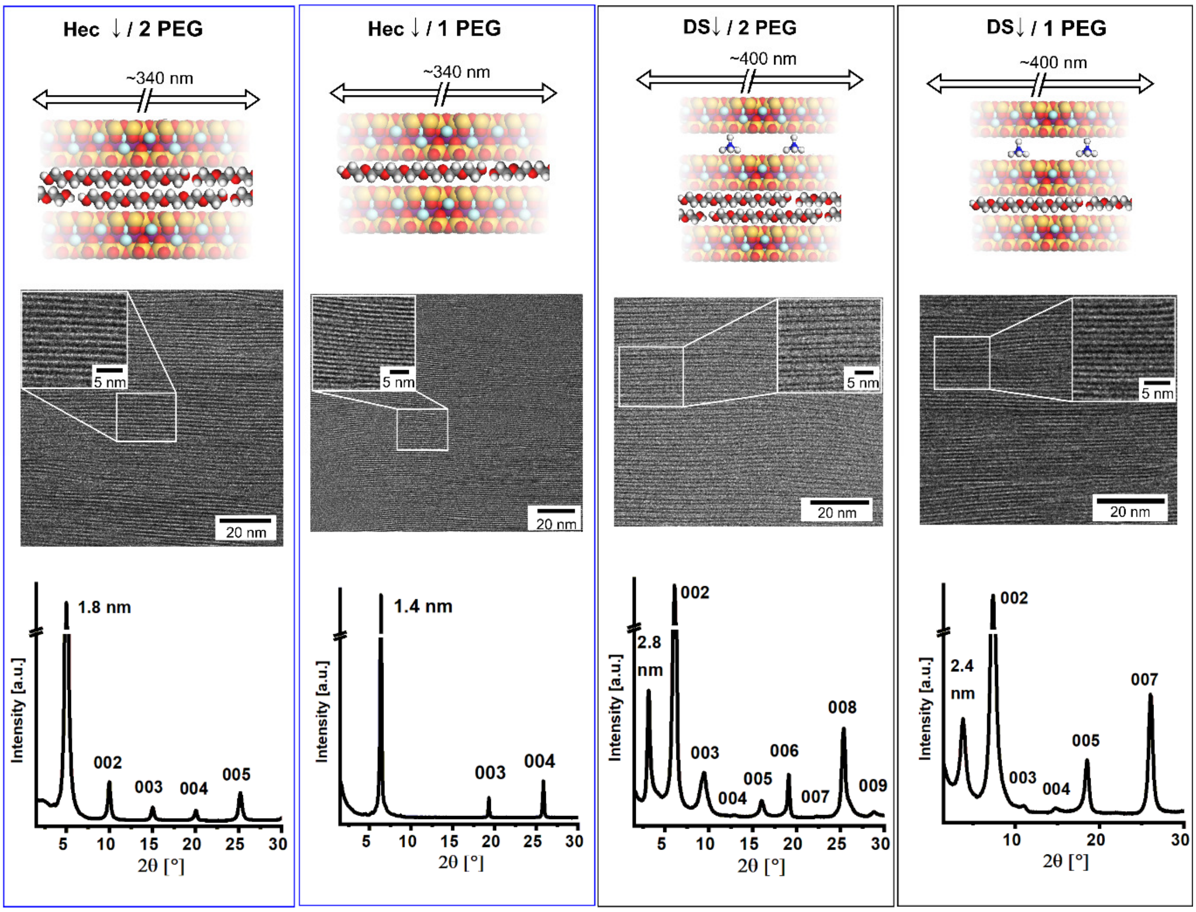

Figure 1: Schematic structures of the hybrid Bragg stacks (top), TEM microscopy images (middle) and XRD patterns. The XRD patterns and TEM images for all hybrid films confirm the perfectly 1D crystallinity as indicated by intense basal reflections, rational *00l*-series and long range periodicity as observed in the TEM images.

Independent of diameter and nanoplatelet thickness (Hec, DS) dilute (<1 vol%) suspensions represent nematic phases in water with nanoplatelets being separated to large distances > 50 nm.[8] Therefore solution compounding could easily be achieved simply by mixing the nematic Hec and DS phases with different amounts of an aqueous PEG solution as evidenced by small angle X-ray scattering (SAXS) (Figure S2), which proves that the nematic character of the suspension is preserved during compounding indicating periodic homogeneity.

Spray coating on PET followed by gentle drying produced self-supporting, transparent nanocomposite films that could easily be pulled of the substrate. Due to the huge aspect ratio the nanoplatelets, moreover, align parallel to the substrate and actually, a monocrystalline film was obtained with the stacking direction oriented perpendicular to the film (Figure 1 middle).

Intercalated phases with PEG volume contents of 46 vol% (Hec/2PEG)[17-19, 29-30] and 30 vol% (Hec/1PEG)[19] corresponding to periodicities of 1.8 nm and 1.4 nm, respectively, were described in literature. Independent of the nanoplatelet diameter, the XRD patterns recorded for the various films confirm the published periodicities of 1.77 nm and 1.38 nm for Hec↑/2PEG, Hec↓/2PEG and Hec↓/1PEG, respectively. The PEG volume contents were carefully optimized to yield perfect periodicity. According to Meuring's rule[31], a defect-free 1D crystallinity corresponds with small FWHM. With our PEG-content optimized samples intense basal reflections of a rational *00l* series up to the 5th and 4th order and a very low CVs of 0.3 to 0.7 % for Hec↓/2PEG and Hec↓/1PEG, respectively, (Figure 1, Table S1) could be achieved.

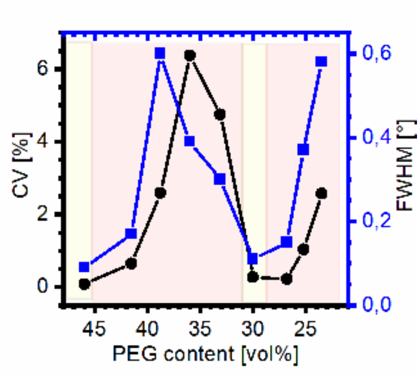

Figure 2: Optimization of the PEG content of Hec↓/2PEG and Hec↓/1PEG to improve 1D crystallinity of hybrid Bragg stacks. Defect-free periodicity corresponds to minima in CV and FWHM, which are observed at 46 and 30 vol%, respectively for Hec↓/2PEG and Hec↓/1PEG.

As expected, FWHM minima (Figure 2) at 46 vol% (Hec↓/2PEG) and 30 vol% (Hec↓/1PEG) coincide with CV minima. Such low CV of 0.1 %(Hec↑/2PEG) are only observed if the interlayer height is absolute uniform, which usually requires ionic or molecular interlayer cations of the same type. Observing such a low CV for a hybrid Bragg stack with intercalated macromolecules is quite surprising as even low molecular weight polymers are expected to adopt different configurations.

In the literature two conflicting structural models are discussed for Hec/2PEG: a double layer of PEG chains[19] or PEG-helices. Even the most precise determination of the periodicity in stacking direction does not allow to differentiate since both secondary structures will have similar heights and both would be in line with the observed interlayer height of 0.77 nm (1.77 nm – thickness of clay layer). For simplicity of drawing the schematics shown in Figure 1, top were drawn with double layers. Transmission electron microscopy (TEM) images (Figure 1, middle) corroborate the defect-free periodic homogeneity.

Applying DS, periodicities and filler content could be varied without compromising homogeneity or the quality of 1D crystallinity. As described for Hec↓/2PEG and Hec↓/1PEG the PEG content was carefully optimized and the optimum 1D crystallinity was observed for 30°vol% and 18 vol% with CV values of 1.6 and 1.0 for DS↓/2PEG and DS↓/1PEG, respectively (Figure 1). As expected the *d*-spacings increase by 1 nm to 2.79 and 2.38 nm for DS/2PEG and DS/1PEG, respectively as compared to the Hec composites, as the thickness of NH_4^+- hectorite is 1 nm. The quality of the 1D crystallinity of the hybrid Bragg stack is comparable to the Hec composites as indicated by intense reflections, a rational *00l*-series up to the 9th and 6th order (Figure 1), respectively, a low FWHM and a low CVs as mentioned above. Moreover, TEM images of both DS composites also showed an exceptional long rang order (Figure 1). Hec↓/1PEG and DS↓/2PEG compositions differ only by the additional NH_4^+ that only shows up by slight variations in the wt% content while the volume content is the same within experimental errors (Table S1). As becomes evident from the PXRD traces and the TEM images, the periodicity of the latter is, however, doubled and thus the interface area between PEG and the clay is halved.

The five different samples prepared allow for studying in a more systematic way the influence of nanoplatelet diameter, filler content and thickness of polymeric decoupling layer on bulk modulus, yield strength and elongation at break for nacre mimics representing single hybrid phases.

Bulk Mechanics by tensile testing of self-supporting films

Stress strain curves were measured at 53 % relative humidity (RH) to determine the mechanical properties of the hybrid Bragg stack films (Figure 3 A-B). Values reported in Table 1 represent average values of seven individual measurements.

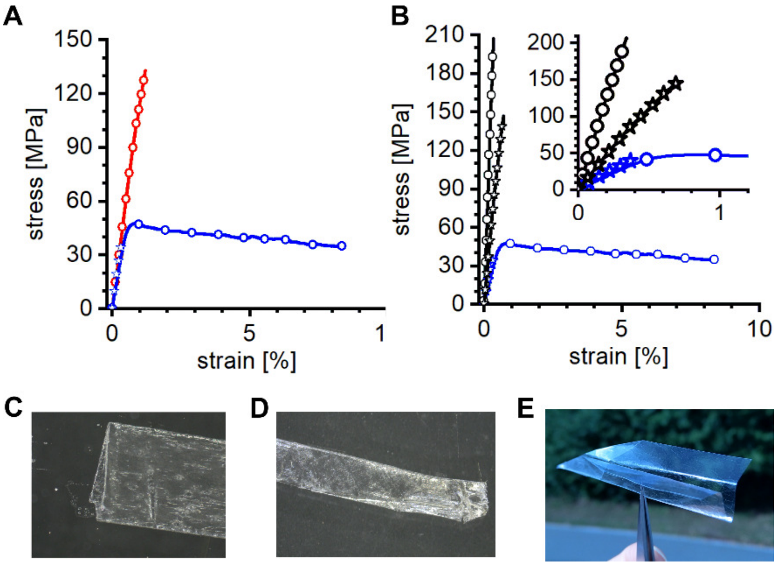

Figure 3: Study of the mechanical properties by tensile testing. A) Influence of the filler diameter: Hec↑/2PEG (red, circle) and Hec↓/2PEG (blue, circle). B) Influence of thickness of filler (Hec vs DS) and thickness of decoupling layer (1PEG vs 2PEG): DS↓/2PEG (black, circle), DS↓/1PEG (black, asterisk) and Hec↓/1PEG (blue, asterisk). C) One half of a test stripe showing brittle fracture of Hec↑/2PEG. D) One half of a tested sample illustrating the plastic deformation of Hec↓/2PEG. E) Transparent and flexible self-supporting films allowing folding without breaking.

First, the impact of the nanoplatelet diameter on the mechanical properties was investigated. The stress-strain curve of the hybrid Bragg stack with a large nanoplatelet diameter Hec↑/2PEG (Figure 3A, red, circle) showed a steep increase and failed catastrophically at a maximum strength of 147 MPa and a small elongation of 1.1 %, without any sign of plastic deformation. Moreover, the fracture point (Figure 3C) shows a defined, smooth edge, being characteristic for a brittle fracture.

At low stress, a similar slope is observed for the small diameter filler (Hec↓/2PEG, Figure 3A, blue, circle), as illustrated by comparable Young's moduli of 10 GPa and 12 GPa for Hec↓/2PEG and Hec↑/2PEG, respectively. However, contrary to the large diameter nanoplatelets, for the small diameter filler Hec↓/2PEG at a yield strength of 48 MPa a plastic deformation is observed. While the strain increased constantly, the stress was slightly reduced, until the sample breaks at an elongation of 8.4 %. The large Hec nanoplatelets appear to be rigidly interlocked and local stresses lead to a brittle fracture, while decreasing the diameter leads to a ductile material with elongation increased by a factor of 8. This suggests that the smaller Hec platelets with a diameter of 340 nm allow the sliding of the platelets against each other, going along with a stretching of the test strip (Figure 3D). Moreover, the transparent nacre-mimetic can be folded like a paper (Figure 3E) without breaking. While previous studies have varied the diameter by applying different clay sources,[11] which implies that many other parameters are inevitably also changes, in particular the amount of accessory minerals, the cation exchange capacity and the homogeneity of charge density, here the diameter was changed by sonication, which keeps everything else constant. With average diameters of 18000 nm and 340 nm and assuming circular shape, absolute areas of 508.938 μm^2 and 0.182 μm^2 indicate that the interface area for an individual Hec↑/2PEG nanoplatelet is by a factor of ≈ 2800 larger than for Hec↓/2PEG. In a first approximation, the absolute interaction for adjacent individual platelets in the stacking direction will thus also be much stronger for

Hec↑/2PEG. The brittle behavior would actually suggest that it is too strong to allow sliding and energy dissipation related to it.

The ability of a material to undergo deformation due to frictional motion between stacked moieties in the brick and mortar structure is crucial for the local dissipation of high stresses that would otherwise cause the material to fracture by stress concentration into a single filler nanoplatelet. The deformation by platelet sliding in nacre is limited by the surface roughness of the aragonite platelets and mineral bridges, which restore the interaction and assure a constant strength during plastic deformation. For clay nanocomposites, sliding has previously been observed with polymers, which are capable of forming sacrificial hydrogen bonds.[32-33] Since the clay surface is atomically flat and carries no functional groups capable of forming e.g. hydrogen bonds, the deformation process in the hybrid Bragg stacks deficient of such hydrogen bonding networks, is lacking necessary re-pinning mechanisms and therefore the strength slightly decreases with elongation.

As the smaller diameter proved advantageous for the toughness, we focused on hybrid Bragg stacks made with the small diameter Hec↓ and DS↓.

Table 1: Overview of material characteristic obtained by tensile testing at 53% RH

sample	Young's modulus - E (GPa)	Maximum tensile strength - σ (MPa)	Elongation at break - ε (%)	Work of fracture [MJ/m^3]
Hec↑/2PEG	12 ± 1	130 ± 20	1.2 ± 0.3	0.7 ± 0.4
Hec↓/2PEG	10 ± 1	48 ± 5	8.4 ± 2.0	3.4 ± 0.9
Hec↓/1PEG	13 ± 1	42 ± 8	0.4 ± 0.1	0.1 ± 0.0
DS↓/2PEG	32 ± 3	202 ± 16	0.7 ± 0.1	0.8 ± 0.1
DS↓/1PEG	26 ± 3	149 ± 19	0.7 ± 0.1	0.6 ± 0.1

Decreasing the PEG content is expected to improve Young's moduli and possibly also strength as the content of the strong component clay is increased to 70 vol% for Hec↓/1PEG (Figure 3B-blue, asterisk). While the Young´s modulus increases slightly to 13 GPa for Hec↓/1PEG as compared to 10 GPa for Hec↓/2PEG, however, the strength decreased from 48 MPa to 42 MPa when lowering the thickness of the PEG decoupling layer. This is due to the brittle nature of Hec↓/1PEG ($\varepsilon = 0.4\%$). Obviously, the single layer PEG chain in the interlayer is coordinated to Na^+ interlayer cations and the Coulomb interaction of the resulting "polycation" hinders sliding of the platelets against each other. This in turn would suggest that in case of Hec↓/2PEG the interface between the two PEG layers is the weakest part in the structure and allows sliding. As stated by Rolle et al.[16] for Hec/PVP, hybrid Bragg stacks with more than one chain in the interlayer exhibit a "bulk-like" and a clay/polymer interface, resulting in two distinct glass transition temperatures of the polymer, strongly confined in this interlayer. Apparently, the distinct interfaces also determine ductility in highly filled hybrid Bragg stacks.

Applying DS instead of Hec should allow for further increasing Young's moduli and possibly also strength as the content of the strong component clay may be increased to a record value of up to 82 vol% for DS↓/1PEG (Figure 3B-blue, asterisk) while additionally the stiffness of DS is 15 % higher than of single Hec nanoplatelets. As expected, the Young´s moduli indeed increases to 32 GPa and 26 GPa for DS↓/2PEG and DS↓/1PEG, respectively. As the filler content for the latter is 12 vol% higher, this is counterintuitive and implies that the mixing rule does not hold. The same is true for the yield strength, which is ≈ 200 MPa for DS↓/2PEG and only ≈ 150 MPa for the higher filler content material DS↓/1PEG. However, the values for Young's modulus and strength are interestingly high, as such high values in nanocomposites, are more likely to be achieved with high Tg polymers[11] in combination with cross-linking[34-35] or by combining low Tg polymers with hydrogen bonding networks.[32-33]

For DS↓/1PEG a brittle behavior (ε = 0.7%) was expected based on observations with Hec↓/1PEG. Unfortunately and somewhat surprisingly, contrary to Hec↓/2PEG (Figure 3B, blue, circle) with DS↓/2PEG (Figure 3C, black, circle), the elongation is reduced from 8.4 % to 0.7 %. Going from Hec to DS a much stiffer (factor 3) and stronger (factor 4) hybrid Bragg stack could be obtained but at the expense of completely loosing ductility. Since the specific interface area per volume is halved when going from Hec to DS, the opposite trend would be expected and the reasons for the catastrophic failure mechanism remain unclear.

CONCLUSION

To summarize, the mechanical properties depend on a number of parameters: filler content, filler stiffness and strength, the nature of potential interactions (reversible or sacrificial) and their strength at filler / organic interface, specific interface area, absolute platelet surface and diameter of nanoplatelets. Moreover, nacre mimics are highly anisotropic due to the highly anisotropic mechanical features of platy nanofillers and their preferred orientation in a film. The interdependence of the various parameters renders systematic optimization difficult. For highly filled nacre mimics the situation becomes even worse due to strong confinement effects that greatly modify the properties of decoupling layers not only as compared to the bulk properties but also when going from e.g. a 2 nm to a 1 nm confinement. Tougher materials require to improve decoupling while offering a variety of energy dissipation mechanisms. This in turn requires less confinement and therefore a higher slit for the polymer while not scarifying homogeneity by (partial) phase segregation.

ASSOCIATED CONTENT

Supporting Information

Detailed information about the hybrid film preparation and characterization with instrumental details; a table for an overview of the structural and chemical characterization.

AUTHOR INFORMATION

Corresponding Author

* E-mail: josef.breu@uni-bayreuth.de (J.B.)

Author Contributions

T.S and J.B. initialized the idea and wrote the manuscript. All authors have given approval to the final version of the manuscript. T.S. explored and optimized the Hec/PEG system, fabricated and characterized the Hec/PEG films, and performed and analyzed the tensile testing measurements. D.W. fabricated the DS.

Funding

This work was supported by the German Science Foundation (DFG) within the collaborative research projects SFB 840 and SFB 1357.

Notes

The authors declare no competing financial interest.

ACKNOWLEDGMENT

The authors thank Florian Puchtler for producing the synthetic clay and Marco Schwarzmann for preparing and taking the transmission electron microscopy images. Moreover, we thank Sabine Rosenfeldt for conducting SAXS measurements on the gel samples. We appreciate the support of the Keylab for Optical and Electron Microscopy of the Bavarian Polymer Institute (BPI).

REFERENCES

1. Ritchie, R. O., The conflicts between strength and toughness. *Nat. Mater.* **2011,** *10* (11), 817-822.
2. Wegst, U. G.; Bai, H.; Saiz, E.; Tomsia, A. P.; Ritchie, R. O., Bioinspired structural materials. *Nat. Mater.* **2015,** *14* (1), 23-36.
3. Xu, Z.-H.; Yang, Y.; Huang, Z.; Li, X., Elastic modulus of biopolymer matrix in nacre measured using coupled atomic force microscopy bending and inverse finite element techniques. *Mater. Sci. Eng. C* **2011,** *31* (8), 1852-1856.
4. Wang, R. Z.; Suo, Z.; Evans, A. G.; Yao, N.; Aksay, I. A., Deformation mechanisms in nacre. *J. Mater. Res.* **2011,** *16* (09), 2485-2493.
5. Meyers, M. A.; Lin, A. Y.; Chen, P. Y.; Muyco, J., Mechanical strength of abalone nacre: role of the soft organic layer. *J. Mech. Behav. Biomed. Mater.* **2008,** *1* (1), 76-85.
6. Barthelat, F.; Espinosa, H. D., An Experimental Investigation of Deformation and Fracture of Nacre–Mother of Pearl. *Exp. Mech.* **2007,** *47* (3), 311-324.
7. Stöter, M.; Rosenfeldt, S.; Breu, J., Tunable Exfoliation of Synthetic Clays. *Annu. Rev. Mater. Res.* **2015,** *45* (1), 129-151.
8. Rosenfeldt, S.; Stöter, M.; Schlenk, M.; Martin, T.; Albuquerque, R. Q.; Förster, S.; Breu, J., In-Depth Insights into the Key Steps of Delamination of Charged 2D Nanomaterials. *Langmuir* **2016,** *32* (41), 10582-10588.
9. Tsurko, E. S.; Feicht, P.; Habel, C.; Schilling, T.; Daab, M.; Rosenfeldt, S.; Breu, J., Can high oxygen and water vapor barrier nanocomposite coatings be obtained with a waterborne formulation? *J. Membr. Sci.* **2017,** *540*, 212-218.
10. Morits, M.; Verho, T.; Sorvari, J.; Liljeström, V.; Kostiainen, M. A.; Gröschel, A. H.; Ikkala, O., Toughness and Fracture Properties in Nacre-Mimetic Clay/Polymer Nanocomposites. *Adv. Funct. Mater.* **2017,** *27* (10).
11. Das, P.; Malho, J. M.; Rahimi, K.; Schacher, F. H.; Wang, B.; Demco, D. E.; Walther, A., Nacre-mimetics with synthetic nanoclays up to ultrahigh aspect ratios. *Nat. Commun.* **2015,** *6*, 5967.
12. Tsurko, E. S.; Feicht, P.; Nehm, F.; Ament, K.; Rosenfeldt, S.; Pietsch, I.; Roschmann, K.; Kalo, H.; Breu, J., Large Scale Self-Assembly of Smectic Nanocomposite Films by Doctor Blading versus Spray Coating: Impact of Crystal Quality on Barrier Properties. *Macromolecules* **2017,** *50* (11), 4344-4350.
13. Das, P.; Schipmann, S.; Malho, J. M.; Zhu, B.; Klemradt, U.; Walther, A., Facile access to large-scale, self-assembled, nacre-inspired, high-performance materials with tunable nanoscale periodicities. *ACS Appl. Mater. Inter.* **2013,** *5* (9), 3738-47.
14. Wang, Z.; Rolle, K.; Schilling, T.; Hummel, P.; Philipp, A.; Kopera, B. A. F.; Lechner, A. M.; Retsch, M.; Breu, J.; Fytas, G., Tunable Thermoelastic Anisotropy in Hybrid Bragg Stacks with Extreme Polymer Confinement. *Angew. Chem. Int. Ed.* **2020,** *59* (3), 1286-1294.
15. Schilling, T.; Habel, C.; Rosenfeldt, S.; Röhrl, M.; Breu, J., Impact of Ultraconfinement on Composite Barriers. *ACS Appl. Polym. Mater.* **2020,** *2* (7), 3010-3015.
16. Rolle, K.; Schilling, T.; Westermeier, F.; Das, S.; Breu, J.; Fytas, G., Large Tg Shift in Hybrid Bragg Stacks through Interfacial Slowdown. under revision at ACS Nano, 2020.
17. Habel, C.; Maiz, J.; Olmedo-Martínez, J. L.; López, J. V.; Breu, J.; Müller, A. J., Competition between nucleation and confinement in the crystallization of poly(ethylene glycol)/ large aspect ratio hectorite nanocomposites. *Polymer* **2020**, 122734.
18. Eckert, A.; Abbasi, M.; Mang, T.; Saalwächter, K.; Walther, A., Structure, Mechanical Properties, and Dynamics of Polyethylenoxide/Nanoclay Nacre-Mimetic Nanocomposites. *Macromolecules* **2020,** *53* (5), 1716-1725.

19. Wu, J.; Lerner, M. M., Structural, thermal, and electrical characterization of layered nanocomposites derived from sodium-montmorillonite and polyethers. *Chem. Mat.* **1993,** *5* (6), 835-838.

20. Stöter, M.; Kunz, D. A.; Schmidt, M.; Hirsemann, D.; Kalo, H.; Putz, B.; Senker, J.; Breu, J., Nanoplatelets of sodium hectorite showing aspect ratios of approximately 20,000 and superior purity. *Langmuir* **2013,** *29* (4), 1280-1285.

21. Stöter, M.; Biersack, B.; Reimer, N.; Herling, M.; Stock, N.; Schobert, R.; Breu, J., Ordered Heterostructures of Two Strictly Alternating Types of Nanoreactors. *Chem. Mater.* **2014,** *26* (18), 5412-5419.

22. Stöter, M.; Biersack, B.; Rosenfeldt, S.; Leitl, M. J.; Kalo, H.; Schobert, R.; Yersin, H.; Ozin, G. A.; Förster, S.; Breu, J., Encapsulation of functional organic compounds in nanoglass for optically anisotropic coatings. *Angew. Chem. Int. Ed.* **2015,** *54* (16), 4963-7.

23. Stöter, M.; Gödrich, S.; Feicht, P.; Rosenfeldt, S.; Thurn, H.; Neubauer, J. W.; Seuss, M.; Lindner, P.; Kalo, H.; Möller, M.; Fery, A.; Förster, S.; Papastavrou, G.; Breu, J., Controlled Exfoliation of Layered Silicate Heterostructures into Bilayers and Their Conversion into Giant Janus Platelets. *Angew. Chem. Int. Ed.* **2016,** *55* (26), 7398-7402.

24. Möller, M. W.; Hirsemann, D.; Haarmann, F.; Senker, J.; Breu, J., Facile Scalable Synthesis of Rectorites. *Chem. Mater.* **2010,** *22* (1), 186-196.

25. Breu, J.; Seidl, W.; Stoll, A. J.; Lange, K. G.; Probst, T. U., Charge Homogeneity in Synthetic Fluorohectorite. *Chem. Mater.* **2001,** *13* (11), 4213-4220.

26. Lerf, A., Storylines in intercalation chemistry. *Dalton Trans.* **2014,** *43* (27), 10276-10291.

27. Kunz, D. A.; Erath, J.; Kluge, D.; Thurn, H.; Putz, B.; Fery, A.; Breu, J., In-plane modulus of singular 2:1 clay lamellae applying a simple wrinkling technique. *ACS Appl. Mater. Interfaces* **2013,** *5* (12), 5851-5855.

28. Arkhipovich, G. N.; Dubrovskii, S. A.; Kazanskii, K. S.; Shupik, A. N., Complexing of Na† ion with polyethylene glycol. *Polym. Sci. (U.S.S.R.)* **1981,** *23* (7), 1827-1841.

29. Aranda, P.; Ruiz-Hitzky, E., Poly(ethylene oxide)-silicate intercalation materials. *Chem. Mater.* **1992,** *4* (6), 1395-1403.

30. Strawhecker, K. E.; Manias, E., Crystallization Behavior of Poly(ethylene oxide) in the Presence of Na+Montmorillonite Fillers. *Chem. Mat.* **2003,** *15* (4), 844-849.

31. Moore, D. M.; Reynolds, R. C.; M., D., *X-ray Diffraction and the Identification and Analysis of Clay Minerals*. Oxford University Press: Oxford, U.K., 1997.

32. Zhu, B.; Jasinski, N.; Benitez, A.; Noack, M.; Park, D.; Goldmann, A. S.; Barner-Kowollik, C.; Walther, A., Hierarchical Nacre Mimetics with Synergistic Mechanical Properties by Control of Molecular Interactions in Self-Healing Polymers. *Angew. Chem. Int. Ed.* **2015,** *54* (30), 8653-7.

33. Eckert, A.; Rudolph, T.; Guo, J.; Mang, T.; Walther, A., Exceptionally Ductile and Tough Biomimetic Artificial Nacre with Gas Barrier Function. *Adv Mater* **2018,** *30* (32), e1802477.

34. Walther, A.; Bjurhager, I.; Malho, J. M.; Pere, J.; Ruokolainen, J.; Berglund, L. A.; Ikkala, O., Large-area, lightweight and thick biomimetic composites with superior material properties via fast, economic, and green pathways. *Nano Lett.* **2010,** *10* (8), 2742-2748.

35. Walther, A.; Bjurhager, I.; Malho, J. M.; Ruokolainen, J.; Berglund, L.; Ikkala, O., Supramolecular control of stiffness and strength in lightweight high-performance nacre-mimetic paper with fire-shielding properties. *Angew. Chem. Int. Ed.* **2010,** *49* (36), 6448-6453.

Supporting Information

One-dimensional crystalline clay nacre mimetics with record filler contents (73 wt% - 91 wt%): From brittle to ductile to brittle

*Theresa Schilling[1], Daniel Wagner[1],Olli Ikkala[2], Josef Breu[1]**

[1]Bavarian Polymer Institute and Department of Chemistry, University of Bayreuth, Universitätsstr. 30, 95440 Bayreuth, Germany

[1]Center of Excellence in Molecular Engineering of Biosynthetic Hybrid Materials Research, Aalto University, FI-00076, Finland

KEYWORDS: clay, organic-inorganic hybrid composites, nacre-mimetic, mechanical properties, Ultraconfinement, toughness

* Corresponding author

E-Mail: Josef.Breu@uni-bayreuth.de

S1. Sample preparation

Materials

The synthetic clay sodium fluorohectorite (Hec, $[Na_{0.5}]^{inter}[Mg_{2.5}Li_{0.5}]^{oct}[Si_4]^{tet}O_{10}F_2$) was synthesized by melt synthesis followed by long-term annealing, according to an already published procedure.[1-2] The material featured a cation exchange capacity of 1.18 mmol g^{-1} and an aspect ratio of 18 000.[1-2] The material with this huge pristine aspect ratio is referred to by Hec↑. Upon immersion in deionized water, the pristine material swells osmotically producing a nematic suspension with nanoplatelets of mean diameters of ≈ 18 µm being separated by > 100 nm at 0.4 vol%.[3]

The synthesis of double stacks (DS), consisting of strictly alternating sodium and ammonium interlayers was performed according to an already published procedure.[4]

To reduce the original diameter, a 0.4 vol% suspension of delaminated Hec↑ or DS↑ was sonicated for 15 minutes in an ice bath applying a UIP 1000hd (Hielscher Ultrasonic GmbH, Germany) equipped with a ultrasonic horn BS2d22 and a booster B2-1.2, at 20 kHz with a maximal output power of 1000 W.

The sonicated suspensions were diluted (0.0004 vol%), drop casted on a plasma-treated silicon wafer and sputtered with 10 nm carbon for scanning electron microscopy (SEM) applying a Zeiss Ultra plus (Carl Zeiss AG, Germany) at an operating voltage of 3 kV. *ImageJ* was used to evaluate the average diameter of 150 nanoplatelets. (Figure S1). The small aspect ratio suspensions and/ or platelets are referred to as Hec↓ and DS↓. The average diameter of Hec↓ and DS↓ is 340 and 406 nm, respectively.

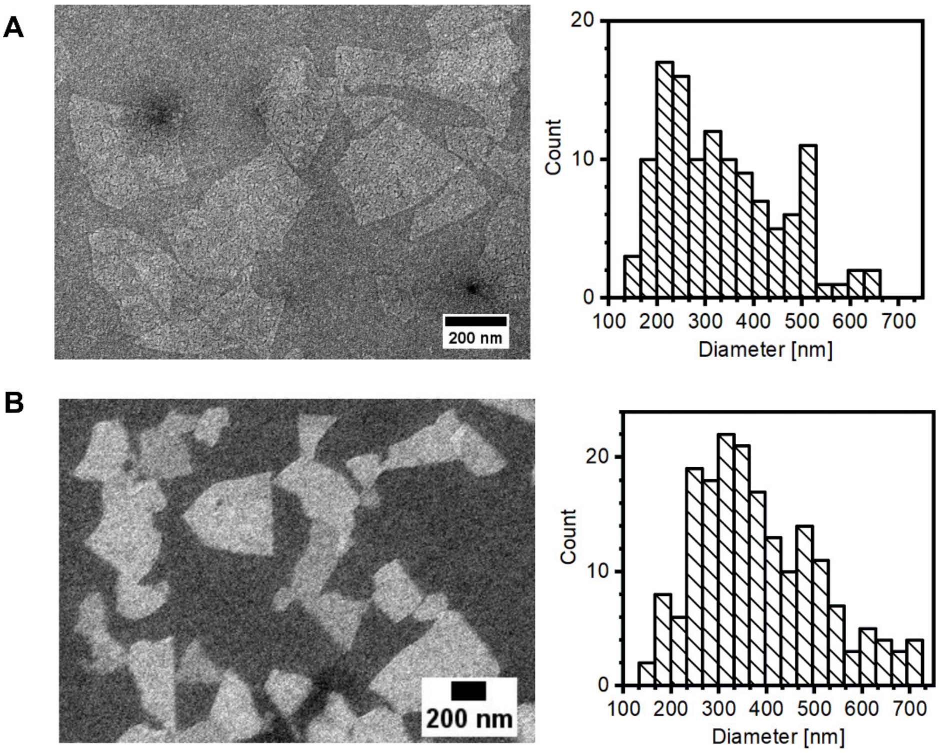

Figure S1. Typical SEM micrographs and histograms of the platelet diameter distribution of sonicated (A) Hec↓ and (B) DS↓ as evaluated by *ImageJ*.

Film preparation

An aqueous Polyethylene glycol (PEG-1500 Mw = 1500 g mol^{-1}, Sigma Aldrich) solution (0.8 vol%) was added in appropriate amounts to obtain the desired volume ratio of Hec or DS to PEG. To assure homogenization, the suspension was mixed for 1 day in the overhead shaker.

The self-supporting films were prepared by spray coating. The fully automatic spray coating system was equipped with a SATA 4000 LAB HVLP 1.0 mm spray gun (SATA GmbH & Co. KG, Germany). Suspensions were sprayed on a corona-treated polyethylene terephthalate (PET) foil (optimont 501, bleher Folientechnik, Germany). The spraying and nozzle pressure were set constant at values of 2 and 4 bar, respectively. The round per flat fan control was set to 6 with a flow speed of 3 mL s^{-1}. The distance between the spraying gun and the substrate was 17 cm. The thickness of the suspension layer applied in one spraying step is about 2 µm which corresponds to about 20 nm dry film thickness. For drying the suspension layer, the sample is stopped under infrared lamps until evaporation of the solvent is complete. After every spraying cycle, a drying cycle of 90 s with a temperature of 40 °C took place. The spraying/drying cycle is repeated until the desired barrier film thickness of 30 µm is obtained. Afterward, the film was dried at 60 °C for 7 days, and peeled off from the PET foil for achieving self-supporting films.

In total, we prepared five different samples: Hec↑/2PEG, Hec↓/2PEG, Hec↓/1PEG, DS↓/2PEG, DS↓/1PEG. The nomenclature is based on the two different volume contents of PEG. A detailed explanation is given in Table S1.

S2. Characterization of the suspensions and films

Small Angle X-Ray Scattering (SAXS)

All SAXS data were measured using the small-angle X-ray system “Double Ganesha AIR” (SAXSLAB, Denmark). The X-ray source of this laboratory-based system is a rotating anode (copper, MicroMax 007HF, Rigaku Corporation, Japan), providing a micro-focused beam. The data were recorded by a position-sensitive detector (PILATUS 300 K, Dectris). To cover the range of scattering vectors different detector positions were used. The measurements of the suspensions were done in 1 mm glass capillaries (Hilgenberg, code 4007610, Germany) at room temperature. To improve the detection limit of the in-house machine, the suspensions were first concentrated by centrifugation at 10,000 rpm for 1 hour. The data were radially averaged and background corrected. As background, a water-filled capillary was used.

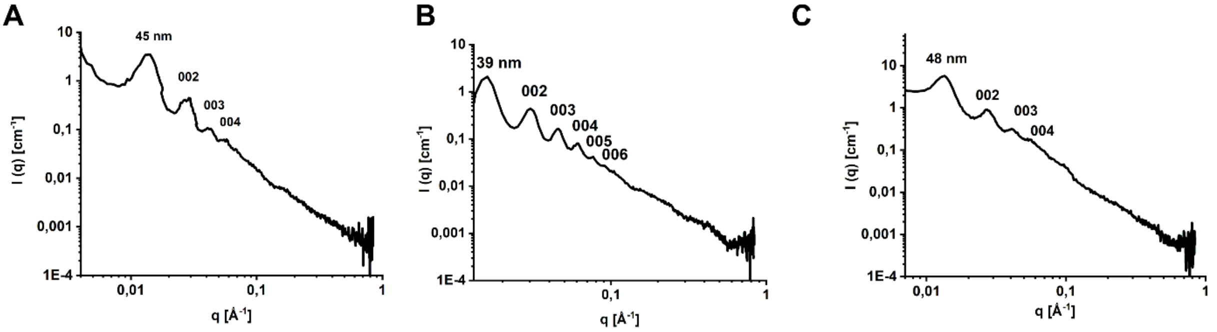

Figure S2. One-dimensional SAXS pattern of the concentrated gel samples A) Hec↑/2PEG, B) Hec↓/2PEG, and C) DS↓/2PEG. The varying layer separations observed are related to the clay content of the suspensions rather than the Hec/PEG ratio.

X-Ray diffraction (XRD) analysis

XRD patterns for the films were recorded in Bragg-Brentano-geometry on an Empyrean diffractometer (PANalytical B.V.; the Netherlands) using Cu K_α radiation (λ = 1.54187 Å). The self-supporting films were placed on glass slides (Menzel-Gläser; Thermo Scientific). Before the measurements, samples were dried at 100 °C for one week in a vacuum chamber.

As a measure of the quality of the one-dimensional crystallinity of the films, the coefficient of variation (CV) and the full width at half maximum (FWHM) were determined (Table S1). Large CV-values (> 3%[4]) and large FWHM indicate non-rationality of the diffraction pattern as caused by a random interstratification of different interlayer heights, which represent defects in the periodicity.

Table S1. Overview of the structural and chemical characterization at 0 % RH.

sample	nominal Hec:PEG ratio [wt%]	nominal Hec:PEG ratio [vol%]	PEG content* [wt%]	PEG content** [vol%]	Nominal d-spacing [nm]	Observed d-spacing [nm]	CV [%]	FWHM [°2θ]
Hec↑/2PEG	73:27	54:46	27	46	1.77	1.77	0.1	0.1-0.2
Hec↓/2PEG	73:27	54:46	27	46	1.76	1.77	0.3	0.3-0.5
Hec↓/1PEG	84:16	70:30	16	30	1.38	1.38	0.6	0.5-0.9
DS↓/2PEG	84:16	70:30	16	30	2.77	2.79	1.6	0.4-0.8
DS↓/1PEG	91:9	82:18	9	18	2.38	2.39	1.0	0.5-1.0

* determined by TGA (Fig. S2); ** recalculated from vol% PVP assuming bulk density

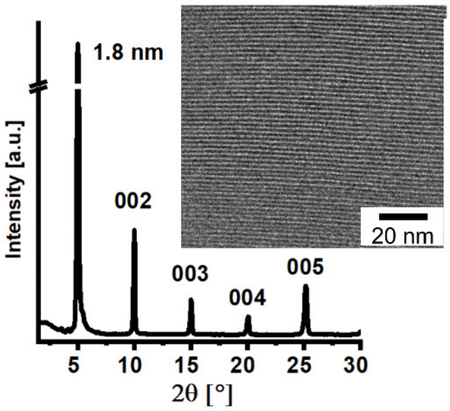

Figure S3. XRD pattern and TEM image of Hec↑/2PEG.

Thermogravimetric analysis (TGA)

These ratios were cross-checked (Figure S2, Table S1) for the dried films by thermogravimetric analysis (TGA), using a Mettler Toledo SDTA851 equipped with the gas control unit TS0800GC1 (Mettler Toledo, USA). Changes in mass observed upon heating in synthetic air up to 900 °C were attributed to the combustion of PEG. (Figure S2).

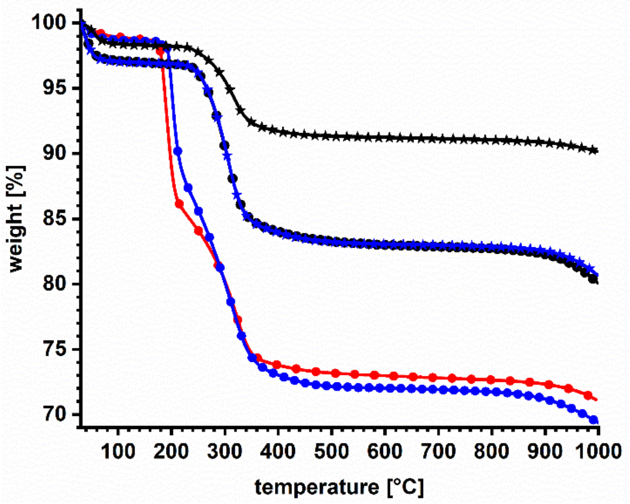

Figure S4. TGA curves of Hec↑/2PEG (red curve, circle), Hec↓/2PEG (blue curve, circle), Hec↓/1PEG (blue curve, asterisk), DS↓/2PEG (black curve, circle), DS↓/1PEG (black curve, asterisk). The weight loss below 150 °C corresponds to adsorbed water.

Transmission electron microscopy (TEM)

TEM images of the self-supporting films were taken on a JEOL JEM-2200FS (JEOL GmbH, Germany) at an acceleration voltage of 200 kV. Cross-section pictures of the self-supporting films were prepared with a Cryo Ion Slicer IB-09060CIS (JEOL, Germany).

Tensile testing

The stress-strain curves were recorded with a ZwickRoell material testing machine of the type BT1-FR0.5TN.D14 (ZwickRoell, Ulm, Germany) equipped with a 20 N load cell (Xforce HP, ZwickRoell, Ulm, Germany). The test strips had a dimension of 20 mm x 2 mm x 30 µm. Before testing, the test strips were conditioned in a desiccator with a relative humidity of 53 % RH for 7 days. A minimum of 7 test strips was measured for every sample.

Literature

(1) Breu, J.; Seidl, W.; Stoll, A. J.; Lange, K. G.; Probst, T. U. Charge Homogeneity in Synthetic Fluorohectorite. *Chem. Mater.* 2001, *13*, 4213-4220.

(2) Stöter, M.; Kunz, D. A.; Schmidt, M.; Hirsemann, D.; Kalo, H.; Putz, B.; Senker, J.; Breu, J. Nanoplatelets of sodium hectorite showing aspect ratios of approximately 20,000 and superior purity. *Langmuir* **2013,** *29*, 1280-1285.

(3) Rosenfeldt, S.; Stöter, M.; Schlenk, M.; Martin, T.; Albuquerque, R. Q.; Förster, S.; Breu, J. In-Depth Insights into the Key Steps of Delamination of Charged 2D Nanomaterials. *Langmuir* **2016,** *32*, 10582-10588.

(4) Stöter, M.; Gödrich, S.; Feicht, P.; Rosenfeldt, S.; Thurn, H.; Neubauer, J. W.; Seuss, M.; Lindner, P.; Kalo, H.; Möller, M.; Fery, A.; Förster, S.; Papastavrou, G.; Breu, J. Controlled Exfoliation of Layered Silicate Heterostructures into Bilayers and Their Conversion into Giant Janus Platelets. *Angew. Chem. Int. Ed.* **2016,** *55*, 7398-7402.

9 List of publications and conferences

Publications and Manuscripts

- Schilling, T.;Wagner, D., Ikkala. O., Breu, J., One-diemnsional crystalline clay nacre-mimetics with record filler contents (73 wt%-91 wt%): From bittle to ductile to brittle
- Rolle, K; Schilling, T.; Westermeier, F.; Das, S.; Breu, J.; Fytas, G., Large Tg Shifts in Hybrid Bragg Stacks through Interfacial Slowdown. *Macromolecules.* **2021**, *54* (5), 2551-2560.
- Schilling, T.; Habel, C.; Rosenfeldt, S.; Röhrl, M.; Breu, J., Impact of Ultraconfinement on Composite Barriers. *ACS Appl. Polym. Mater.* **2020**, *2* (7), 3010-3015.
- Philipp, A.; Hummel, P.; Schilling, T.; Feicht, P.; Rosenfeldt, S.; Ertl, M.; Schottle, M.; Lechner, A. M.; Xu, Z.; Gao, C.; Breu, J.; Retsch, M., Anisotropic Thermal Transport in Spray-Coated Single-Phase Two-Dimensional Materials: Synthetic Clay Versus Graphene Oxide. *ACS Appl. Mater. Inter.* **2020**, *12* (16), 18785-18791.
- Wang, Z. Y.; Rolle, K.; Schilling, T.; Hummel, P.; Philipp, A.; Kopera, B. A. F.; Lechner, A. M.; Retsch, M.; Breu, J.; Fytas, G., Tunable Thermoelastic Anisotropy in Hybrid Bragg Stacks with Extreme Polymer Confinement. *Angew Chem Int Edit* **2020**, *59* (3), 1286-1294.
- Zhu, J.; Habel, C.; Schilling, T.; Greiner, A.; Breu, J.; Agarwal, S., Filter-Through Method of Making Highly Efficient Polymer-Clay Nanocomposite Membranes. *Macromol. Mater. Eng.* **2019**, *304* (7).
- Tsurko, E. S.; Feicht, P.; Habel, C.; Schilling, T.; Daab, M.; Rosenfeldt, S.; Breu, J., Can high oxygen and water vapor barrier nanocomposite coatings be obtained with a waterborne formulation? *J. Membr. Sci.* **2017**, *540*, 212-218.

Conferences

2019 *"Tunable thermoelastic anisotropy in Hybrid Bragg stacks with extreme polymer confinement"* - **Poster**

Theresa Schilling, Zuyuan Wang, Konrad Rolle, Patrick Hummel, Alexandra Philipp, Bernd A. F. Kopera, Anna M. Lechner, Markus Retsch, Josef Breu, George Fytas

16th Biennial Bayreuth Polymer Symposium, 22th - 24th September, 2019, Bayreuth, Germany

2019 *"Tunable thermoelastic anisotropy in Bragg stacks with extreme polymer confinement"* - **Talk**

Theresa Schilling, Zuyuan Wang, Konrad Rolle, Patrick Hummel, Alexandra Philipp, Markus Retsch, Josef Breu, George Fytas

Euroclay 2019 - International conference on clay science and technology, 1st - 5th July, 2019, Paris, France

2018 "Spray Coating of Large Area Smectic Crystals and their Mechanical Properties" - **Poster**

Theresa Schilling, Christoph Habel, Josef Breu

19th International Symposium on the Reactivity of Solids (ISRS - 19), Bayreuth, Germany

Danksagung

Ich möchte mich bei allen Menschen bedanken, die mich im Laufe der Promotion und während des Studiums an der Universität Bayreuth unterstützt haben. Durch euch, war die Zeit sehr schön.

Mein ganz besonderer Dank gilt meinem Betreuer Herrn Prof. Dr. Josef Breu, der mir dieses interessante und spannende Promotionsthema ermöglichte, mich stets unterstütze, mir die benötigten Freiheiten in der Forschung lies und doch stets ein offenes Ohr für mich hatte.

Des Weiteren möchte ich mich bei allen Kooperationspartnern für die enge fachliche Zusammenarbeit bedanken. Durch Euch wurde die Realisierung dieser Arbeit und die weitreichende Charakterisierung der Hybrid Bragg Stacks erst möglich. Mein besonderer Dank gilt Prof. Dr. Markus Retsch und Prof. Dr. George Fytas für die regen fachlichen Diskussionen. Darüber hinaus danke ich Dr. Patrick Hummel, Alexandra Philipp, Marius Schöttle und Kai Herrmann für die Messungen der thermischen Leitfähigkeit und Konrad Rolle, Zuyuan Wang und Malgorzata Bartkiewicz für die Bestimmung der mechanischen Moduli an unzähligen Hybrid Bragg Stacks.

Mein Dank gilt weiterhin meinen Kollegen der ACI und AC III, die mich nicht nur fachlich, sondern auch durch Lachen und einer extra Portion Humor in zahlreichen Kaffeepausen unterstützt haben. In diesem Zusammenhang ist besonders Marion Breunig, Martin Rieß, Dr. Wolfgang Milius und mein langjähriger Laborkollege Dr. Thomas Martin zu erwähnen. Danke für Eure Unterstützung in den letzten Jahren! Danke Marco Schwarzmann für dein Engagement aus meinen Proben die besten TEM Bilder herauszuholen. Darüber hinaus möchte ich mich bei Elmar Sehl für seine Hilfe bei den Zugversuchen bedanken.

Mein Dank gilt auch meinen weit verstreuten Freunden, Yogamädels und CoMento Mädels. Ohne euch hätte ich nicht den hin und wieder nötigen Abstand zur Uni bekommen. Danke, dass es euch gibt. Ihr habt mich nicht nur fachlich, sondern auch geistig weiterentwickelt.

Zum Schluss danke ich meinem Mann und meiner Familie für die unablässige Unterstützung und den Rückhalt. Ohne eure Liebe, Vertrauen, aufmunternde Worte, Zuspruch und den Rückhalt wäre ich heute nicht an dieser Stelle.

(Eidesstattliche) Versicherungen und Erklärungen

§ 9 Satz 2 Nr. 3 PromO BayNAT

Hiermit versichere ich eidesstaatlich, dass ich die Arbeit selbstständig verfasst und keine anderen als die von mir angegebenen Quellen und Hilfsmittel benutzt habe.
(*vgl. Art. 64 Abs. 1 Satz 6 BayHSchG*)

§9 Satz 2 Nr. 3 PromO BayNAT

Hiermit erkläre ich, dass ich die Dissertation nicht bereits zur Erlangung eines akademischen Grades eingereicht habe und dass ich nicht bereits diese oder eine gleichartige Doktorprüfung endgültig nicht bestanden habe.

§9 Satz 2 Nr. 4 PromO BayNAT

Hiermit erkläre ich, dass ich Hilfe von gewerblichen Promotionsberatern bzw. -vermittlern oder ähnlichen Dienstleistern weder bisher in Anspruch genommen habe noch künftig in Anspruch nehmen werde.

§9 Satz 2 Nr. 7 PromO BayNAT

Hiermit erkläre ich mein Einverständnis, dass die elektronische Fassung meiner Dissertation unter Wahrung meiner Urheberrechte und des Datenschutzes einer gesonderten Überprüfung unterzogen werden kann.

§9 Satz 2 Nr. 8 PromO BayNAT

Hiermit erkläre ich mein Einverständnis, dass bei Verdacht wissenschaftlichen Fehlverhaltens Ermittlungen durch universitätsinterne Organe der wissenschaftlichen Selbstkontrolle stattfinden können.

Bayreuth, den Dienstag, 10. August 2021

Ort, Datum Theresa Sophie Dörres